Master's Thesis

Behaviour of cohesionless soil during cyclic loading

June 2012

Amir Shajarati
Kris Wessel Sørensen
Søren Kjær Nielsen

M.Sc. in Civil and Structural Engineering, Aalborg University

STUDENT REPORT
AALBORG UNIVERSITET

The Faculty of Engineering
Sohngårdsholmsvej 57
Phone 96 35 97 31
Fax 98 13 63 93
http://www.bsn.aau.dk

Title: Behaviour of Cohesionless Soil During Cyclic Loading
Project period: Autumn 2011 - Spring 2012
Project group: b124b

Group members:

Amir Shajarati

Kris Wessel Sørensen

Søren Kjær Nielsen

Supervisors:
Prof. Lars Bo Ibsen
Associate Prof. Johan Clausen

Circulation: 6
Pages: 138
Appendix pages: 32
Finished: 14 June 2012

Synopsis:

One of the challenges in offshore geotechnical engineering, is how to account for cyclic loading. This has lead to several research projects regarding cyclic loading. However, due to the complexity of the loading and the effects hereof, no standardized method for taking cyclic loading into consideration has yet been made. Therefore the topic of cyclic loading still needs more investigation.
Through this Master Thesis the effects that cyclic loading will have on cohesionless soils have been investigated. The soil in question is a marine sand taken from an offshore site in Frederikshavn, Denmark, where a prototype of a suction bucket foundation has been installed supporting a Vestas V90-3.0 MW wind turbine.
Cyclic triaxial tests have been conducted in order to construct design diagrams that can be used in the design of new offshore wind turbine foundations. During these tests it was found that the cyclic and average load ratios, along with the pore pressure, had a significant impact on the cyclic load bearing capacity.
An advanced constitutive model in form of the *Modified Critical State Two-Surface Plasticity Model for Sand* with an explicit integration scheme was also coded in Matlab. This was done in order to create a model, which could accurately simulate cyclic soil behaviour. However, the explicit integration scheme was found to be inefficient and could therefore not be recommended for a constitutive model of this advanced level.

Preface

This Master's Thesis "Behaviour of Cohesionless Soil During Cyclic Loading" accounts for 45 ECTS and was carried out in the period September 2011 to June 2012 at the Department of Civil Engineering, Aalborg University, Denmark under the Geotechnical Engineering Research Group.

The thesis consists of four parts. The first part is an introduction to the investigated subject including the aim of thesis. The second part consists of three articles; The first article is a literature study dealing with the relevant topics for cyclic loaded soils. The second article contains the test results for cyclic triaxial tests on Frederikshavn Sand. Prior to the execution of the triaxial tests, the cyclic triaxial apparatus was assembled, and a test manual describing the test procedure was made along with corrections to an earlier manual. The third article is concerning the implementation of a simple explicit integration scheme into an advanced constitutive model. The third part contains concluding remarks, which includes a conclusion, a discussion and suggestions for future investigations. The fourth part is an appendix, which should be seen as an addendum to the report.

The report is divided into chapters, sections and subsections. These different levels have been numbered in the order they appear. E.g. the first chapter in the report is numbered 1, the first section in this chapter 1.1 etc. In the appendix the chapters have been numbered the same way as described before, but with an A in front of the numbers. E.g. the first chapter in the appendix is numbered A1, the first section A1.1 etc. The articles are constructed in the same way, but they only consists of sections and subsections.

Figures and tables are numbered in accordance with the chapter they appear within. E.g. the first figure in the third chapter has been given the number 3.1, the second 3.2 etc. Captions will appear under each figure and above each table. If no source of reference has been submitted in the caption, the picture or table is created by the group.

Throughout the report and articles references to different sources will appear. A detailed description of these is presented in the end of the report or article. The references appear in accordance with the Harvard-method. In the text the references are shown on the form (surname, year) or surname (year). If a reference is placed before a full stop, it refers to the very sentence only. If the reference is after the full stop, it refers to the entire section.

Contents

PART I

INTRODUCTION

1 Introduction

From 2012 to 2035 the worlds power consumption is expected to increase with approximately 50 % to 225 TW according to the U.S. Energy Information Administration [2011], see Figure 1.1. This makes the need for energy resources ever higher as natural resources are dwindling. Furthermore, increasing governmental demands require lower emissions and more sustainable energy sources to power the world. The Danish Government has initiated a plan to make 50 % of Denmark's energy production come from renewable energy sources by 2020 and 100 % by 2050 [Energistyrelsen, 2012].

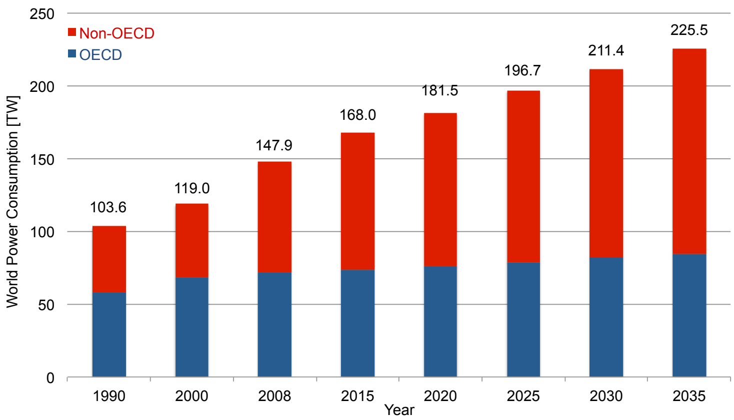

Figure 1.1: *World power consumption projected to the year 2035 [U.S. Energy Information Administration, 2011].*

This has lead to an evolution of the wind turbine technology, which have seen large progress over the past 25 years. Wind turbines have grown in both size and energy output, thereby becoming more efficient at harvesting energy from the wind. Figure 1.2 shows how the size, from the first 50 kW wind turbine erected in 1985, has evolved up to the multi-MW wind turbines that are available today.

With the increase in size of wind turbines it has become more and more difficult to find suitable places onshore to locate wind farms. This has lead to several offshore wind farms in the last 10 years and more are planned for future construction. A benefit of going offshore is the increase in mean wind speed due to less disturbance of the wind field. However, when going offshore the cost of energy becomes more expensive due to higher operational costs, larger loads and complex site conditions. Recent offshore wind farms have been located further away from the coast and in deeper waters. Something which increases the cost of energy even more.

As the wind farms are moving out into deeper waters the foundations become larger and the loads as well. Cyclic loading from waves, wind and current plays an important role in the fatigue limit state, which for wind turbines typically means a maximum permanent rotation of 0.5°. The inclusion of cyclic loading is important because during the 25 years of which a wind turbine is operational, it will be subjected to approximately 10^8 cycles [Achmus et al., 2009][Lesny, 2010]. This can lead to a significant reduction of the bearing capacity or unacceptable soil deformations.

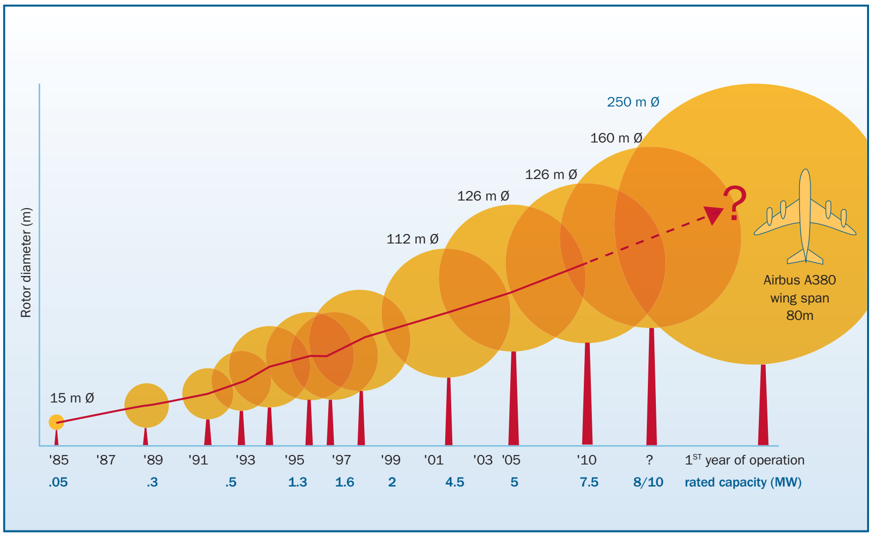

Figure 1.2: *Evolution of wind turbine sizes [UpWind, 2011].*

1.1 Foundations for Offshore Wind Turbines

There are different foundation concepts for offshore wind turbines, of which five are shown in Figure 1.3. One of these is the suction bucket/caisson foundation, which is latest type of the shown concepts. Studies have shown that the bucket foundation, with suitable soil condition, is feasible in up to 30 meters of water depth [Universal Foundation, 2012]. It has some advantages compared to many other foundation concepts, with respect to price and environmental impact.

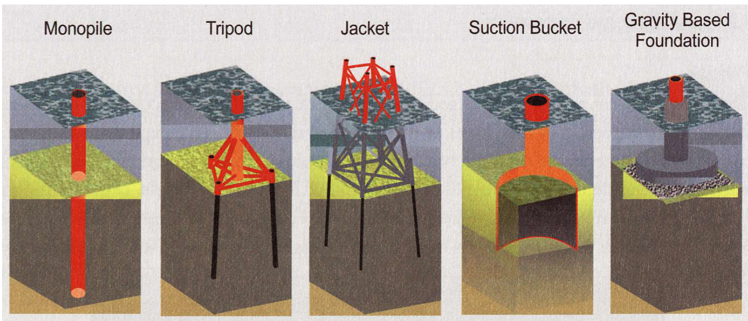

Figure 1.3: *Conventional foundations for offshore wind energy plants. [Lesny, 2010]*

As the environmental requirements increase, the requirements for offshore wind turbine foundations also increase. Some of the environmental requirements are concerning noise levels during installation, in order to protect fish and sea mammals. Comparing the installation of a monopile and a suction bucket, the monopile is installed by ramming the pile into the soil with heavy machinery. This creates large vibrations which in some cases can create acoustic noise levels of up to 200 dB, which can be lethal to fish and sea mammals [Lesny, 2010]. The installation process for the suction caisson is made by vacuum, which only requires light machinery.

Another regulatory requirement is that the seabed should be left undisturbed after the wind turbine have served its operation time. For a monopile the uninstallation is done by cutting-off the pile several meters below the sea bed. The upper part is removed and the steel may be reused, the rest is left into the seabed. When the suction bucket needs to be removed the vacuum inside is being replaced by pressure and the entire bucket comes out of the seabed. This make the entire steel structure reusable, which beside having an environmental effect, also has a positive economical effect.

1.2 Frederikshavn Sand

On a prototype of the suction bucket foundation, a fully operational Vestas V90-3.0 MW offshore wind turbine was installed in 2002 in Frederikshavn on a test site [Universal Foundation, 2012]. Due to the success of the first prototype, a new and larger bucket foundation is planned for installation in late 2012 with a new Vestas 7.0 MW wind turbine. The new foundation will be installed in deeper waters off the coast of Frederikshavn.

Figure 1.4: *Installation of the Suction Bucket at Frederikshavn. Photo: Lars Bo Ibsen.*

In order to calculate the bearing capacity of the new bucket, soil samples have been taken for laboratory testing, which has been classified as a marine sand with shell deposits. The sand in question will be used for all the investigations during this thesis.

1.3 Aim of Thesis

The aim of this thesis is to investigate the undrained effects on Frederikshavn Sand affected by cyclic loading. In order to do this, cyclic triaxial tests will be conducted on the sand in question. The tests will be conducted undrained in order to simulate the effects that a single storm will have on the soil in cases were the drainage path is too long for the excess pore pressure to dissipate. Furthermore, to simulate offshore conditions the tests will be conducted with a relative density I_D = 80 %. The overall aim of these triaxial tests is to develop a design diagram, which can be used in order to determine the cyclic bearing capacity of the soil for a given cyclic load history.

Besides the cyclic triaxial tests an explicit integration scheme will be implemented into an advanced constitutive model, namely the *Modified Critical State Two-Surface Plasticity Model for Sand* originally developed by Manzari and Dafalias [1997a] and modified by LeBlanc [2008]. The constitutive model should be able to correctly model cyclic loading on soils and capture effects such as pore pressure build-up, liquefaction and change in void ratio. The implementation of the explicit integration scheme is done in order to investigate if the constitutive model is still able to maintain accuracy and efficiency with a simple integration scheme.

Part
II
Articles

Article 1

Behaviour of Cohesionless Soils During Cyclic Loading

Behaviour of Cohesionless Soils During Cyclic Loading

Amir Shajarati
Kris Wessel Sørensen
Søren Kjær Nielsen
Lars Bo Ibsen

ISSN 1901-7278
DCE Technical Memorandum No. 14

AALBORG UNIVERSITY
Department of Civil Engineering

Aalborg University
Department of Civil Engineering
Geotechnical Engineering

DCE Technical Memorandum No. 14

Behaviour of Cohesionless Soils During Cyclic Loading

by

Amir Shajarati
Kris Wessel Sørensen
Søren Kjær Nielsen
Lars Bo Ibsen

June 2012

Scientific Publications at the Department of Civil Engineering

Technical Reports are published for timely dissemination of research results and scientific work carried out at the Department of Civil Engineering (DCE) at Aalborg University. This medium allows publication of more detailed explanations and results than typically allowed in scientific journals.

Technical Memoranda are produced to enable the preliminary dissemination of scientific work by the personnel of the DCE where such release is deemed to be appropriate. Documents of this kind may be incomplete or temporary versions of papers—or part of continuing work. This should be kept in mind when references are given to publications of this kind.

Contract Reports are produced to report scientific work carried out under contract. Publications of this kind contain confidential matter and are reserved for the sponsors and the DCE. Therefore, Contract Reports are generally not available for public circulation.

Lecture Notes contain material produced by the lecturers at the DCE for educational purposes. This may be scientific notes, lecture books, example problems or manuals for laboratory work, or computer programs developed at the DCE.

Theses are monograms or collections of papers published to report the scientific work carried out at the DCE to obtain a degree as either PhD or Doctor of Technology. The thesis is publicly available after the defence of the degree.

Latest News is published to enable rapid communication of information about scientific work carried out at the DCE. This includes the status of research projects, developments in the laboratories, information about collaborative work and recent research results.

Published 2012 by
Aalborg University
Department of Civil Engineering
Sohngaardsholmsvej 57,
DK-9000 Aalborg, Denmark

Printed in Aalborg at Aalborg University

ISSN 1901-7278
DCE Technical Memorandum No. 14

Behaviour of Cohesionless Soils During Cyclic Loading

Amir Shajarati[1] Kris Wessel Sørensen[1] Søren Kjær Nielsen[1] Lars Bo Ibsen[2]

Department of Civil Engineering, Aalborg University

Abstract

Offshore wind turbine foundations are typically subjected to cyclic loading from both wind and waves, which can lead to unacceptable deformations in the soil. However, no generally accepted standardised method is currently available, when accounting for cyclic loading during the design of offshore wind turbine foundations. Therefore a literature study is performed in order to investigate existing research treating the behaviour of cohesionless soils, when subjected to cyclic loading. The behaviour of a soil subjected to cyclic loading is found to be dependent on; the relative density, mean effective stresses prior to cyclic loading, cyclic and average shear stresses and the drainage conditions.

1 Introduction

Offshore wind turbine foundations are typically subjected to cyclic loading from both wind and waves. It is therefore important that not only the static load-bearing capacity is investigated, but also the cyclic load-bearing capacity. However, at present there is no generally accepted standardised method, which can be applied in order to determine the cyclic load-bearing capacity for offshore wind turbine foundations.

In order to understand the effects that cyclic loading has on cohesionless soils, literature on the topic from different authors has been gathered and a literature study is presented in this article. The purpose is to describe how the soil behaves when subjected to cyclic loading. As mentioned cyclic loading can be caused by environmental loads from wind and waves. This form of loading will have an effect on soil properties such as soil stiffness, shear strength, and void ratio.

The stresses in this article are mapped by the Cambridge method where the deviatoric stress, q, and the mean principle stress, p, are defined as

$$q = \sigma_1 - \sigma_3 \tag{1}$$

$$p = \frac{\sigma_1 + \sigma_2 + \sigma_3}{3} \tag{2}$$

2 Characteristic Line

The transition from compressive to dilative behaviour is denoted as the *characteristic state*, and is illustrated for different stress paths by dots in Figure 1. The characteristic state is defined as the state where $\delta\varepsilon_v/\delta\varepsilon_1$ is equal to zero, and plotted in a p' - q diagram they construct a straight line through origio. This line is defined as the *characteristic line*, and the angle of the characteristic line is referred to as the *characteristic friction angle*, φ_{cl}. Stress states below the characteristic line leads to contraction ($\Delta\varepsilon_v > 0$) whereas if a stress state is above the characteristic line it leads to dilation ($\Delta\varepsilon_v < 0$). This means that a dense soil following a given stress path starting from below the characteristic line to a stress point above it, will first contract, then dilate when it crosses the characteristic line.

A similar transition occurs in the undrained state, where the so-called *phase transformation line* describes the change in incremental pore pressure, Δu, going from positive to negative increments. The phase transformation stress is defined as where p' has a vertical tangent, i.e. where the mean effective

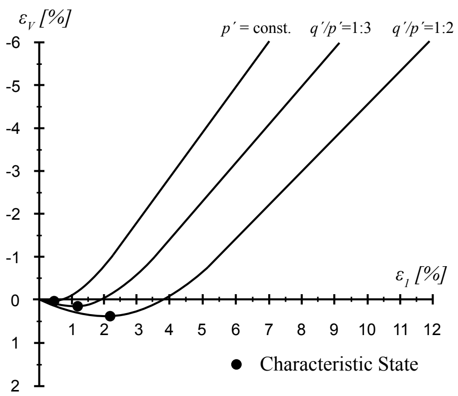

Figure 1: *Volumetric strain as a function of the axial strains during a triaxial compression test on a dense sand for a specimen with equal height and diameter.(Ibsen, 1998)*

[1] *M.Sc. Student, Department of Civil Engineering, Aalborg University, Denmark*

[2] *Prof., Department of Civil Engineering, Aalborg University, Denmark*

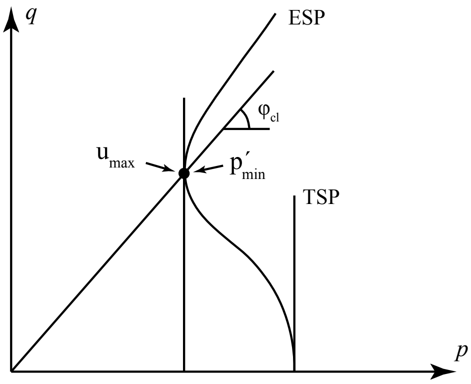

Figure 2: *Phase transformation state in undrained triaxial compression tests on sand with p = constant. ESP = Effective Stress Path. TSP = Total Stress Path. (Ibsen, 1998).*

stress reaches the lowest value, p'_{min}, as shown in Figure 2.

2.1 Influence of Relative Density

Figure 3 shows the failure envelopes for sands with different relative densities, I_D, along with the characteristic line. It is seen that sands with higher relative density dilates more and therefore gains a higher ultimate shear strength. However for very loose sands and for sands with a very high confining pressure the characteristic line coincides with the failure envelope. The latter case is due to crushing of the particles.

3 Monotonic Triaxial Tests

Triaxial tests, whether they are cyclic or monotonic, can be conducted in several ways. They can be drained or undrained, consolidated or unconsolidated and furthermore the consolidation can be made isotropic or anisotropic. When performing triaxial tests, the soil specimen should reflect the site conditions. This entails in most cases that only

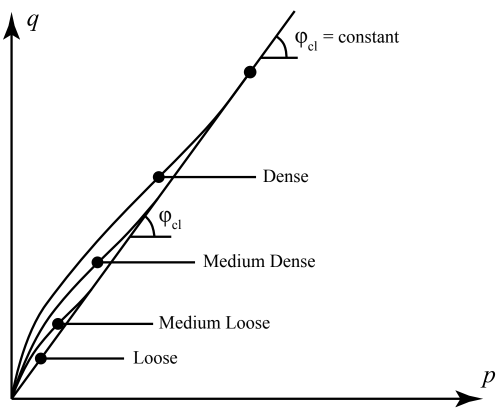

Figure 3: *Variation of drained shear strength envelope for sand with relative density (Ibsen and Lade, 1998a).*

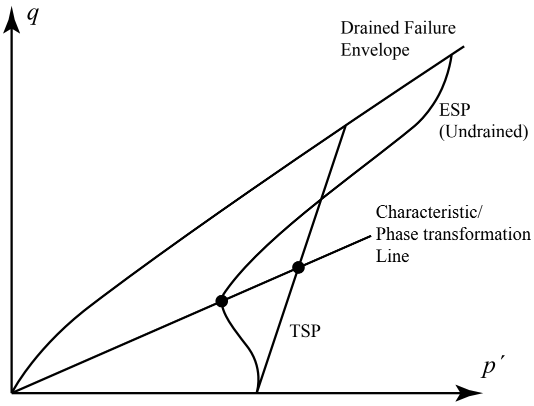

Figure 4: *Difference between a drained and an undrained test starting from the same mean effective stress.*

anisotropic consolidated tests should be used, and the drainage can be chosen so it corresponds to the site specific situation. The response of the soil will be different according to the relative density. In the following section it is only the behaviour of dense, i.e. dilative specimens, that will be treated since these are most common offshore (Lesny, 2010).

3.1 Drained vs. Undrained

In drained triaxial tests the pore pressure is allowed to dissipate and no excess pore pressure is generated. This makes the effective stresses equal to the total stresses and they will follow the total stress path (TSP) in a $p' - q$ diagram as shown in Figure 4.

In undrained triaxial tests no volume change is possible and therefore excess pore pressure is generated. The stresses will therefore follow the effective stress path (ESP) in Figure 4. Below the phase transformation line this will lead to an increase in pore pressure and thereby a drop in effective stresses. When the stress crosses the phase transformation line the soil specimen will attempt to dilate, and therefore negative pore pressure is generated. This leads to an increase in effective stresses, which is why a dilative soil sample can withstand a larger load in the undrained condition compared to the drained condition.

3.2 Undrained Shear Strength

The drained shear strength, τ_f, accounts for the friction angle, the effective mean stress and cohesion, and is given as

$$\tau_f = \frac{1}{2} \cdot \frac{6\ \sin\varphi}{3 - \sin\varphi}\ (p' + c' \cot\varphi') \tag{3}$$

where $c' = 0$ for cohesionless soils. In the undrained case for sand, the undrained shear strength, c_u, can be used instead of τ_f according to Ibsen and Lade (1998b). Therefore, the use of the above expression is extended to the undrained case by adding the initial pore pressure, u_0, and the pore pressure at which cavitation occurs u_{cav}, which results in equation (4). The used effective mean stress, p'_{df}, is the one which corresponds to failure in the drained case.

$$c_u = \frac{1}{2} \cdot \frac{6\,\sin\varphi}{3 - \sin\varphi}\,\left(p'_{df} + u_0 + u_{cav}\right) \qquad (4)$$

The argument for using the above expression is that the undrained bearing capacity for a dense sand is governed by cavitation, as negative pore pressure develops during loading (Ibsen and Lade, 1998b). It is therefore important to include the pore pressure when calculating c_u in the undrained case for sand. The effect of adding the initial pore pressure, u_0, and the pore pressure at cavitation, u_{cav}, is illustrated in Figure 5. The figure illustrates the effective stress paths for two examples with the same initial effective mean stress, p'_0. The two examples end up having a different undrained shear strength, because of differences in initial pore pressure. Following the total stress path will lead to drained failure in point (a), which is the point where p'_{df} is measured. From this point the amount of initial pore pressure and the pore pressure at cavitation is added to p'_{df}. This means that a higher amount of initial pore pressure will lead to a higher value of the undrained shear strength before failure is reached, which is illustrated by point (b) and (c).

4 Cyclic loading

A definition of cyclic loading is needed in order to determine how to conduct laboratory tests with cyclic loading on cohesionless soil. In Peralta (2010) a definition of cyclic loading is given as a load frequency between 0 and 1 Hz, as shown in Table 1. Furthermore, inertia forces can be neglected due to the low frequency, and the accumulated strain is predominantly plastic.

Cyclic loading is defined by two components; the *average shear stress*, τ_a, and a *cyclic shear stress*,

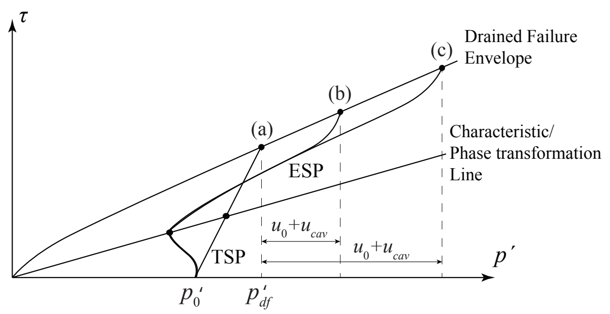

Figure 5: *Illustration of the effect of including initial pore pressure and the pore pressure at cavitation to the drained failure criterion.*

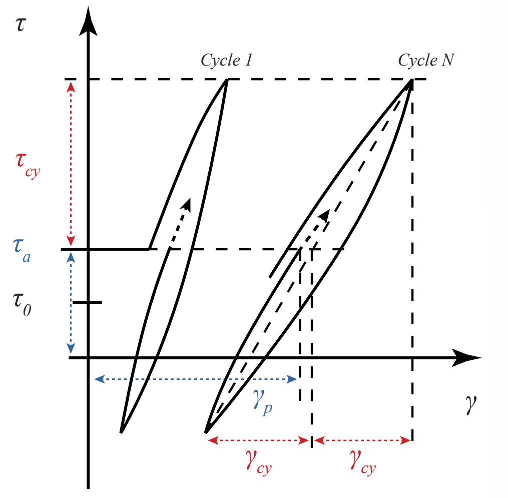

Figure 6: *Definition of stress and strain under cyclic loading (Andersen, 2009).*

τ_{cy}, which is the amplitude of a load cycle. These are depicted in Figure 6.

Failure caused by cyclic loading is defined as either 15 % of *permanent shear strain*, γ_p, or 15 % *cyclic shear strain*, γ_{cy}, according to Andersen (2009). The cyclic and permanent shear strains are also depicted in Figure 6.

4.1 Critical States During Cyclic Loading

In order to determine failure during cyclic loading the concept of *cyclic limit state*, CLS, is used. The cyclic limit state describes the upper bound for non-failure conditions of cyclic loaded soils. The cyclic limit state is a straight line in the $p' - q$ space, on which a single point is defined as the *critical level of repeated loading*, $CLRL$. $CLRL$ is by Ibsen (1998) and Peralta (2010) defined as the upper bound stress level for a given soil at which strains and/or pore pressures accumulate continuously and lead to failure, and is therefore the shear stress level at the CLS-line in the $p' - q$ space.

Laboratory tests of soils under cyclic loading has shown, that soils subjected to a finite number of load cycles not necessarily reach failure, i.e. the cyclic limit state. In some cases the soil will instead reach a state of equilibrium before failure thereby producing only an elastic response, i.e no plastic strain or pore pressure accumulation with additional load cycles. This phenomenon is also known as *shakedown*.

4.2 Cyclic Stable State

A stress state where the positive and negative pore pressures generated neutralize each other is known as the *cyclic stable state*. For the undrained state it is defined as $\Sigma\Delta u = 0$ during a cycle. Ibsen (1998) performed nine undrained cyclic tests on a sand with $I_D = 0.78$ and equal height and diameter. The tests showed that if the mean deviatoric stress is lower

Table 1: *Approximate classification of repeated loading of soils. (Peralta, 2010)*

Repeated Loading of Soils	Cyclic	Cyclic-Dynamic	Dynamic
Frequency	0 to 1 Hz	1 to 10 Hz	> 10Hz
Inertia	No (negligible)	Yes (relevant)	Yes (relevant)
Strain accumulation	Predominantly plastic	Plastic and elastic	Predominantly elastic

than the cyclic stable state, positive pore pressure is generated. Opposite, a negative pore pressure is generated each time the mean deviatoric stress level becomes higher than the cyclic stable state. This is seen in Figure 7, which shows the nine cyclic tests and the generation of either positive or negative pore pressure. The cyclic loading leads the effective mean stress towards the cyclic stable state in each test. When the cyclic stable state has been reached the effective mean stress does not change and the cyclic loading will not lead to any further hardening or softening of the soil (shakedown).

4.3 Shakedown Theorem

For an elastic-perfectly plastic material subjected to cyclic loading, the shakedown theorem states that the five cases in Figure 8 can occur (Goldscheider, 1977). It could be questioned if it also can be used for soil, which is an elasto-plastic material. However, Goldscheider (1977) found by experiments, that the theorem partially can be used on cohesionless soils. One exception though, was that a pure elastic response of the soil was never observed during the performed cyclic triaxial tests.

Based on some of the cases within the shakedown theorem, different failure modes of soils due to cyclic loading are illustrated in Figure 9. Figure 9(a) shows incremental collapse, where the strain incre-

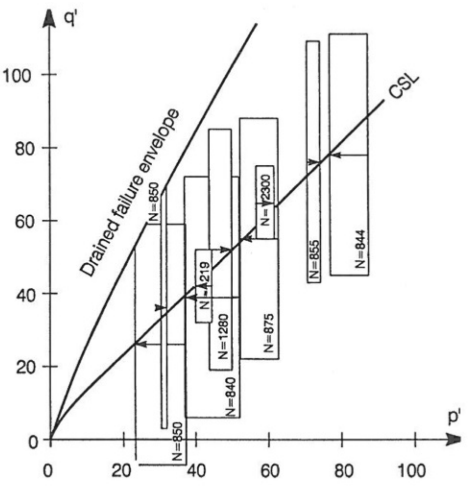

Figure 7: *The effective stress path of nine cyclic tests. The test is performed on Lund No. 0 with I_D = 0.78 and specimens with equal height and diameter. CSL is the Cyclic Stable Line, N is the number of cycles added to the test and the arrow describes the changes in effective mean stress. (Ibsen, 1998)*

Case 1: Elastic response
By sufficiently low cyclic load amplitudes, the response of the structure is elastic with no plastic deformations whatsoever;

Case 2: Ordinary collapse
By sufficiently high cyclic load amplitudes, the load carrying capacity of the structure becomes exhausted and failure occurs instantaneously as plastic, unconstrained deformations develop and the structure collapses – this is also known as ordinary collapse;

Case 3: Incremental collapse
By cyclic load amplitudes less than the collapse load given in (Case 2) and if the plastic strain increments are of the same sign (plastic strain increases incrementally), then the total accumulated plastic deformation of the structure increases indefinitely and becomes so large after a sufficient number of cycles so that it becomes unserviceable. This phenomenon is termed incremental collapse;

Case 4: Alternating plasticity
By cyclic load amplitudes less than the collapse load given in (Case 2) and if the plastic strain increments in each cycle changes sign, then the strain per cycle tends to cancel out the previous strain increment so that no further increase of the overall plastic deformations occurs or the total plastic deformation remains small. This case has been termed as alternating plasticity. In this case, residual forces or stresses remain in the material that do not become constant but tend to change cyclically with time. The plastic work increases indefinitely with number of cycles and at some local points of the structure, material may break due to low-cycle fatigue;

Case 5: Shakedown
In the last case, it may happen that for lower cyclic load amplitudes, an initial plastic deformation of the structure develops but, after a certain finite number of load cycles, the cyclic response of the structure eventually becomes elastic and the structure stabilizes. The stabilization of accumulated plastic deformations is termed as shakedown or adaptation. A significant feature of shakedown are residual stresses in the material that are self-equilibrating which remains constant with time (or number of cycles).

Figure 8: *General shakedown cases for an elasto-plastic material (Goldscheider, 1977).*

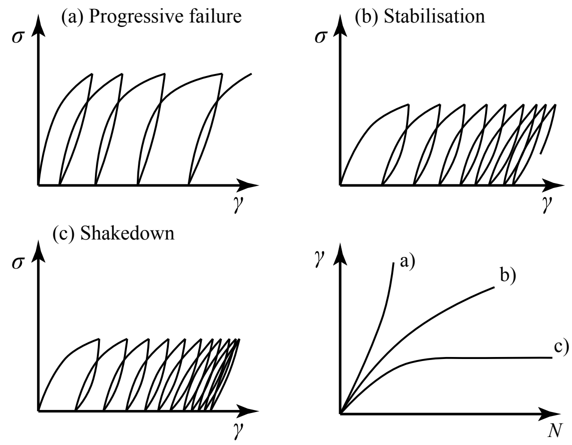

Figure 9: *Visualisation of the shakedown theorem.*

ment increases for every cycle. In Figure 9(b), which is also a form of incremental collapse, the strain increment decreases for larger number of cycles without ever reaching a stable state and therefore failure will eventually occur. Figure 9(c) illustrates shakedown, where the strain increment decreases with increasing number of cycles, but never reaches failure.

4.4 Liquefaction

A special failure mode is known as *liquefaction*. This failure mode can occur when cohesionless soils are exposed to cyclic loading in the undrained state. In this case, there is a probability that the effective stresses will reach zero due to pore pressure build-up and the soil will behave as a liquid with no bearing capacity, as shown in Figure 10. The first time the effective stress reaches zero the soil will try to dilate and negative pore pressure will be generated, which leads to an increase in effective stresses. As cyclic loading continues this pattern will repeat itself and an increase in shear strains is observed as illustrated in Figure 11.

5 Response Due to Cyclic Loading

The response from cyclic loading varies from the response of monotonic loaded tests. The effects of pore pressure build-up in undrained cyclic tests are especially critical for the effective stresses. Furthermore, the response is dependent on whether the test is performed as a direct simple shear test or a triaxial test, which will be outlined in the following sections.

5.1 Cyclic Simple Shear Test

Randolph and Gouvernec (2011) conducted an undrained cyclic simple shear test on cohesionless soil influenced by two-way symmetric loading with a cyclic shear stress, τ_{cy}, equal to 15 kPa as shown in

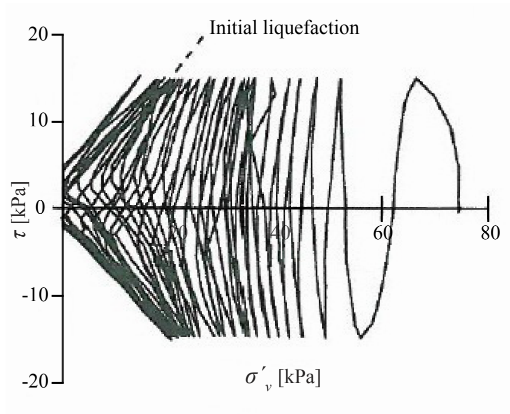

Figure 10: *Results of a consolidated anisotropical undrained simple shear test on seabed sand. Cyclic shear stress is equal to 15 kPa and effective vertical consolidation stress equal to 75 kPa. (Randolph and Gouvernec, 2011)*

Figure 10. The specimen will try to contract leading to an increase in excess pore pressure, which results in a decrease in effective vertical stress, σ'_v. Unlike a monotonic test excess pore pressure continues to increase with repeated load cycles until the effective vertical stress becomes zero. After this point has been reached the specimen tends to dilate which causes a decrease in excess pore pressure and thereby an increase in effective vertical stress. This leads to the butterfly shaped stress paths in Figure 10.

Figure 11 shows the τ - γ diagram from the same test performed by Randolph and Gouvernec (2011). From the figure it is seen that the shear strain is very small until initial liquefaction is reached. From this point additional load cycles leads to a significant increase in shear strain.

5.2 Cyclic Triaxial Test

As stated earlier the soil response from triaxial tests is different from the response obtained by cyclic sim-

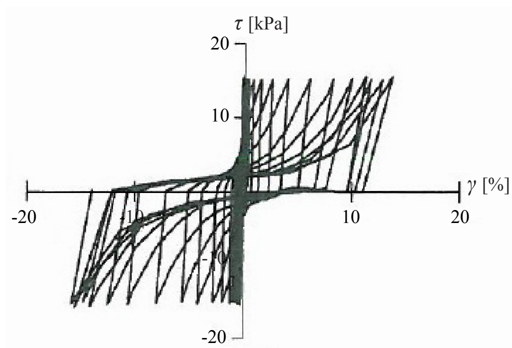

Figure 11: *Results of a consolidated anisotropical undrained simple shear test on seabed sand. Cyclic shear stress is equal to 15 kPa and effective vertical consolidation stress equal to 75 kPa. (Randolph and Gouvernec, 2011)*

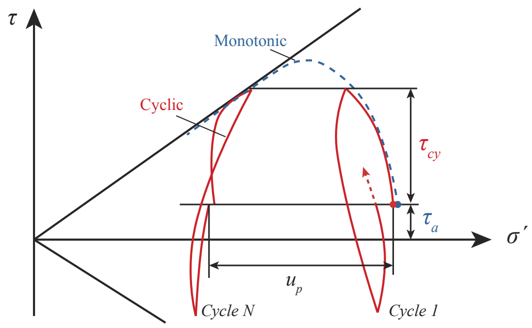

Figure 12: *Effective stress path for an undrained cyclic triaxial test. (Andersen, 2009)*

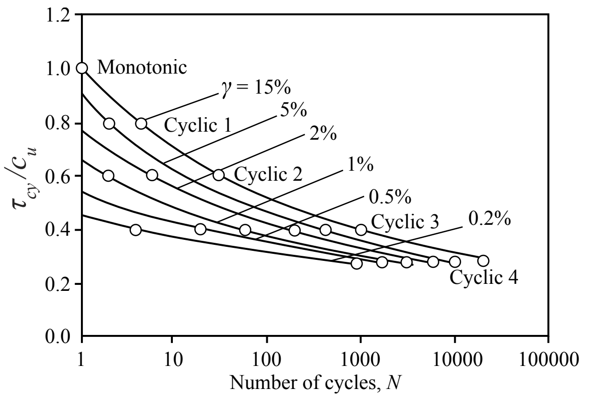

Figure 14: *Strain contour diagram for sand. Average shear stress equal to zero. (Randolph and Gouvernec, 2011)*

ple shear tests. The difference is that during triaxial response pore pressure is reduced when unloaded compared to a cyclic simple shear test where pore pressure still builds up during unloading. However, in cyclic triaxial tests pore pressure build-up still occurs during the course of one cycle (Andersen, 2009). This can be seen when comparing the $\sigma' - \tau$ diagram for a cyclic triaxial test in Figure 12 and a cyclic simple shear test in Figure 10. Moreover it can be observed that the initial stress path is the same as a monotonic test, i.e. until the shear stress reaches its maximum value for the first time, as seen in Figure 12.

Two-way loading is defined by Andersen (2009) as if the shear stresses changes sign and one-way loading if the shear stresses always have either a positive or negative value. In cyclic simple shear tests subjected to two-way loading the soil have the same strength when developing negative and positive shear strain. In two-way loaded triaxial tests the soil will be affected of both compression and extension. In this case the soil do not have the same strength when developing negative and positive shear strain, because the extension strength is lower than the compression strength. Figure 13 shows various cyclic loading conditions for both the cyclic simple shear test and the cyclic triaxial test with the differences in response in a γ - τ diagram.

5.3 Cyclic Load Ratio

Cyclic load ratio is a normalisation of the cyclic shear stress. For cohesive soils it is normalised with respect to the undrained shear strength, and for friction materials the normalisation parameter is the vertical effective consolidation stress. In order to determine how many cycles a sample can withstand before it reaches a maximum shear strain value, Randolph and Gouvernec (2011) made a strain contour diagram as seen in Figure 14. The figure illustrates strain contours for sand from one undrained monotonic and four undrained cyclic symmetric simple shear tests with a cyclic load ratio, τ_{cyc}/s_{uss}, equal to 0.8, 0.6, 0.4 and 0.28. The number of cycles to reach a shear strain with a magnitude of 0.2, 0.5, 1, 2, 5 or 15 % can be identified for any value of τ_{cyc}/s_{uss}.

Randolph and Gouvernec (2011) identified the cyclic load ratio as a very important factor for the bearing capacity of soils when subjected to cyclic loading. As an example it can be seen in Figure 14 that a cyclic load ratio of 0.28 will produce a shear strain of 0.2 % after approximately 1000 cycles. With an increase of the cyclic load ratio to 0.40 a shear strain of 0.2 % will be obtained after only 6 cycles.

5.4 Average Load Ratio

In addition to the cyclic load ratio, Andersen (2009) found that the *average load ratio* also has a large effect on the cyclic load-bearing capacity for soil. The average load ratio is defined as the average shear stress normalised in the same manner as the cyclic load ratio. Furthermore, he showed that the development of shear strain is not dependent on the maximum shear stress, but the ratio between cyclic and average shear stress. This can be seen in Figure 15, where different loadings that all have the same maximum shear stress yield very different results based on their average and cyclic shear stresses.

These effects are combined in Figure 16, together with the number of cycles to failure. This method was suggested by Andersen and Berre (1999), and has the advantage compared to the strain contour diagram, that the average load ratio is also taken into account. It should be noted that failure in Figure 16 is defined as only 3 % average or cyclic shear strain.

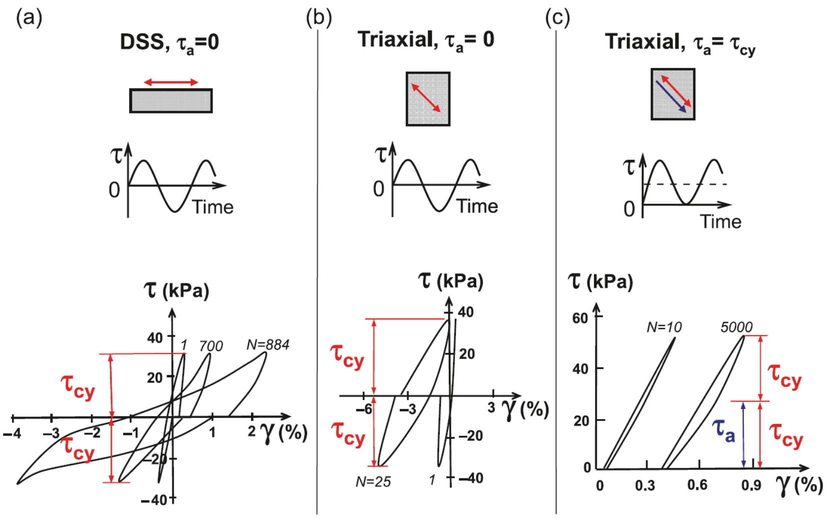

Figure 13: *Stress-strain behaviour under various cyclic loading conditions. (Andersen, 2009)*

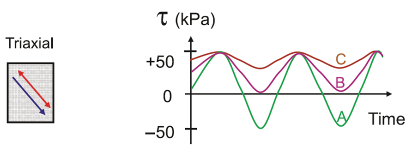

Test	τ_{max}	τ_a	τ_{cy}	Result
A	50	0	50	Failure (γ = 15%) 10 cycles
B	50	25	25	γ_p = 0.8%, γ_{cy} = 0.3% 2500 cycles
C	50	42.5	7.5	γ_p = 0.03%, γ_{cy} = 0.02% 2500 cycles

Figure 15: *Results from cyclic triaxial tests with the same maximum stress, τ_{max}. (Andersen, 2009)*

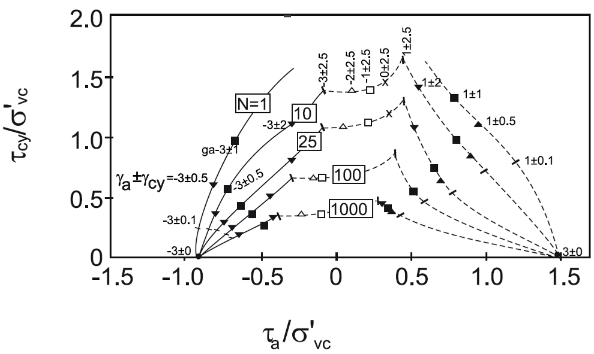

Figure 16: *Number of cycles to failure, depending on cyclic and average load ratio. (Andersen and Berre, 1999)*

6 Conclusion

Cohesionless soils subjected to cyclic loading are influenced by several factors. Most dominating are the average and cyclic load ratios. A small increase in load ratio can mean a significant reduction in the cyclic load bearing capacity. It is also important to take both load ratios into account at the same time and not just the cyclic load ratio.

Cyclic loading also has an influence on the pore pressure in the undrained case. As cyclic loading progresses pore pressure will build up and potentially become equal to the total stresses. When this happens the effective stresses will become zero and liquefaction occurs, producing large shear strains. The opposite can also occur when the stress state is located above the cyclic stable line, thereby creating negative pore pressure, and a subsequent increase in effective stresses. Lastly, shakedown can occur resulting in no pore pressure build-up or increase in shear strains.

The initial pore pressure is found to have a significant impact on the undrained shear strength when conducting monotonic triaxial tests. An increase in the initial pore pressure will give an increase in undrained shear strength due to extra pore pressure before cavitation occurs.

Another relevant parameter is the relative density and its influence on the drained failure envelope. A dense sample will have a higher bearing capacity due to its ability to dilate.

References

Andersen and Berre, **1999**. Knut Andersen and Toralv Berre. *Behaviour of a dense sand under monotonic and cyclic loading*. ECSMGE XII Geotechnical Engineering for transportation Infrastructure., 2, 1999.

Andersen, **2009**. Knut H. Andersen. *Bearing capacity under cyclic loading - offshore, along the coast, and on land. The 21st Bjerrum Lecture presented in Oslo, 23 November 2007*. Canadian Geotechnical Journal, 46(5), pp. 513–535, 2009.

Goldscheider, **1977**. M. Goldscheider. *Shakedown and incremental collapse of structures in dry sand bodies*. Proceedings of Dynamical Methods in Soil and Rock, Plastic and Long-Term Effects in Soils, 1977.

Ibsen, **1998**. Lars Bo Ibsen. *The Mechanism Controlling Static Liquefaction and Cyclic Strength of Sand*. Proc. Int. Workshop on Physics and Mechanics of Soil Liquefaction, (27), 29–39, 1998.

Ibsen and Lade, **1998a**. Lars Bo Ibsen and Poul Lade. *The Role of the Characteristic Line in Static Soil Behavior*. Localization and Bifurcation Theory for Soils and Rocks, pages 221–230, 1998.

Ibsen and Lade, **1998b**. L.B. Ibsen and P.V. Lade. *The Strength and Deformation Characteristics of Sand Beneath Vertical Breakwaters Subjected to Wave Loading*. AAU Geotechnical Engineering Papers, (Soil Mechanics Paper No. 23), 1998.

Lesny, **2010**. Kerstin Lesny. *Foundations for Offshore Wind Turbines*. ISBN: 978-3-86797-042-6, 1. Edition. VGE Verlag GmbH, 2010.

Peralta, **2010**. Proserpine K. Peralta. *Dissertation: Investigations on the Behavior of Large Diameter Piles under Long-Term Lateral Cyclic Loading in Cohesionless Soil*, 2010.

Randolph and Gouvernec, **2011**. M. Randolph and S. Gouvernec. *Offshore Geotechnical Enigineering*. ISBN13: 978-0-415-47744-4, 1. Edition. Spon Press, 2011.

Article 2

Behaviour of Dense Frederikshavn Sand During Cyclic Loading

Behaviour of Dense Frederikshavn Sand During Cyclic Loading

Søren Kjær Nielsen
Amir Shajarati
Kris Wessel Sørensen
Lars Bo Ibsen

ISSN 1901-7278
DCE Technical Memorandum No. 15

AALBORG UNIVERSITY
Department of Civil Engineering

Aalborg University
Department of Civil Engineering
Geotechnical Engineering

DCE Technical Memorandum No. 15

Behaviour of Dense Frederikshavn Sand During Cyclic Loading

by

Søren Kjær Nielsen
Amir Shajarati
Kris Wessel Sørensen
Lars Bo Ibsen

June 2012

Scientific Publications at the Department of Civil Engineering

Technical Reports are published for timely dissemination of research results and scientific work carried out at the Department of Civil Engineering (DCE) at Aalborg University. This medium allows publication of more detailed explanations and results than typically allowed in scientific journals.

Technical Memoranda are produced to enable the preliminary dissemination of scientific work by the personnel of the DCE where such release is deemed to be appropriate. Documents of this kind may be incomplete or temporary versions of papers—or part of continuing work. This should be kept in mind when references are given to publications of this kind.

Contract Reports are produced to report scientific work carried out under contract. Publications of this kind contain confidential matter and are reserved for the sponsors and the DCE. Therefore, Contract Reports are generally not available for public circulation.

Lecture Notes contain material produced by the lecturers at the DCE for educational purposes. This may be scientific notes, lecture books, example problems or manuals for laboratory work, or computer programs developed at the DCE.

Theses are monograms or collections of papers published to report the scientific work carried out at the DCE to obtain a degree as either PhD or Doctor of Technology. The thesis is publicly available after the defence of the degree.

Latest News is published to enable rapid communication of information about scientific work carried out at the DCE. This includes the status of research projects, developments in the laboratories, information about collaborative work and recent research results.

Published 2012 by
Aalborg University
Department of Civil Engineering
Sohngaardsholmsvej 57,
DK-9000 Aalborg, Denmark

Printed in Aalborg at Aalborg University

ISSN 1901-7278
DCE Technical Memorandum No. 15

Behaviour of Dense Frederikshavn Sand During Cyclic Loading

Søren Kjær Nielsen[1] Amir Shajarati[1] Kris Wessel Sørensen[1] Lars Bo Ibsen[2]

Department of Civil Engineering, Aalborg University

Abstract

This article investigates how Frederikshavn Sand behaves when subjected to cyclic loading with emphasis on the development of deformations and the number of cycles, which it can withstand before failure is reached. The investigation is done by performing a series of undrained cyclic triaxial tests, at the Geotechnical Laboratory at Aalborg University. Tests were conducted with a relative density of 80 % in order to simulate offshore conditions where relative densities are relatively high. The purpose is to develop design diagrams, which can be used in order to estimate the undrained cyclic bearing capacity of Frederikshavn Sand for an arbitrary stress level and cyclic loading condition. It is discovered that the governing parameters regarding the response is dependent on the stress path and insitu conditions; initial pore pressure, stress state and the combination of average and cyclic shear stresses.

1 Introduction

The Fatigue Limit State is very often the limiting design condition for offshore wind turbine foundations, which is due to the fact that these foundations are subjected to severe cyclic loading through current, wave and wind actions. During the lifetime of an offshore wind turbine foundation, cyclic loading will correspond to a drained situation since excess pore pressure is able to dissipate between storms. However, during a single storm the drainage path may be long compared to the permeability of the soil, and cyclic loading from a storm may therefore lead to an undrained situation. The tests in this article should imitate cyclic loading during a storm, hence the tests are conducted undrained.

When designing an offshore wind turbine foundation no common design regulation exists regarding cyclic loading. Hence, different approaches have been made as an attempt to include cyclic loading in the design procedure. One method is by the application of design graphs, which accounts for the stresses generated by cyclic loads and the deformations they lead to. These graphs are based on laboratory work in the form of cyclic triaxial or cyclic direct simple shear tests.

The design graphs resulting from the cyclic triaxial tests are to be applied in connection with the construction of an offshore windturbine foundation in Frederikshavn, Denmark. The soil at this location is a marine sand defined as *Frederikshavn Sand*. This paper characterises the Frederikshavn Sand, which the cyclic triaxial tests have been conducted on, and the course of action regarding the execution of cyclic triaxial tests. Furthermore, it is described how Frederikshavn Sand reacts during undrained cyclic loading, which can be applied in a design diagram.

2 Characteristics of Cyclic Loading

Offshore cyclic loading is irregular, where both load period and amplitude changes over time. For laboratory work, however, the cyclic loads are simplified from irregular to regular with a constant period and amplitude. The cyclic load is defined by the cyclic shear stress, τ_{cy}, and the average shear stress, τ_a, with corresponding shear strain, γ_{cy} and γ_p, which is illustrated in Figure 1. τ_a consists of two parts: τ_0 which is the the shear stress obtained from the

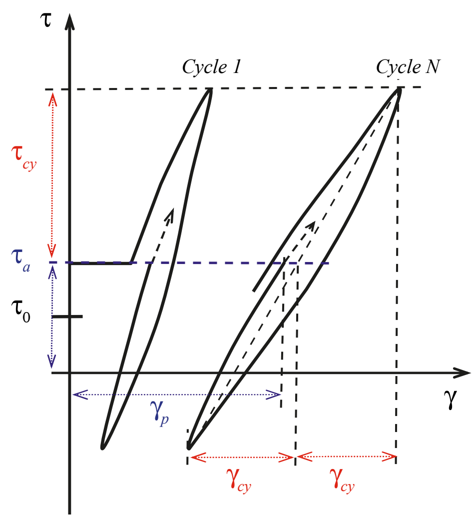

Figure 1: *Stress-strain behaviour under cyclic loading.*

[1] *M.Sc. Student, Department of Civil Engineering, Aalborg University, Denmark*

[2] *Prof., Department of Civil Engineering, Aalborg University, Denmark*

insitu condition, and $\Delta\tau_a = \tau_a - \tau_0$ which is the average shear stress from further loading. This can include the self-weight of a structure and the mean shear stress created by cyclic loading.

During a cyclic triaxial test the soil will experience the cyclic shear stress, τ_{cy}, about the average shear stress, τ_a, see Figure 2(a). The cyclic load depicted in Figure 2(a) gives rise to pore pressure build-up defined by a permanent pore pressure component, u_p, and a cyclic pore pressure component, u_{cy}, as seen in Figure 2(b). As the pore pressure components continue to increase over time it causes a decrease in effective stresses which results in larger and larger permanent shear strain, γ_p, and cyclic shear strains as well, γ_{cy}, see Figure 2(c) (Andersen, 2009). It should be noted, however, that the example given above is not always the case. There are situations where the pore pressure and shear strain evolution responds differently (Shajarati et al., 2012).

The undrained response of a sand is dependent on the relative density. A loose sand will try to compact, and positive pore pressure is generated, which reduces the effective stresses. A dense sand will try to dilate, which results in negative pore pressure. This entails that after initial undrained loading the effective stresses for a dense sand will be increased, and for a loose sand, it will decrease. This is decisive for how the initial stress path will look like. In Figure 3 an example of a loose sand is given. It is seen that the effective stresses decrease as cyclic loading continues, and the stress path will eventually intersect the failure envelope. For a dense sand the arc of the initial stress path will first go towards larger effective stresses, and thereafter the effective stresses will start to decrease as pore pressure builds up.

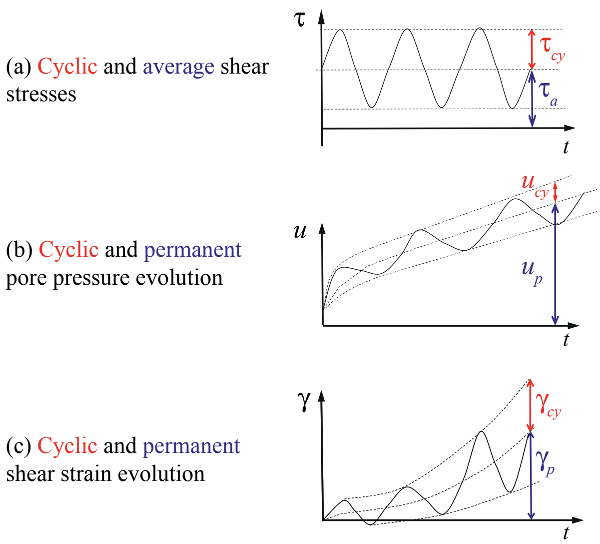

Figure 2: *Shear stress, pore pressure and shear strain as a function of time during undrained cyclic loading.*(Andersen, 2009)

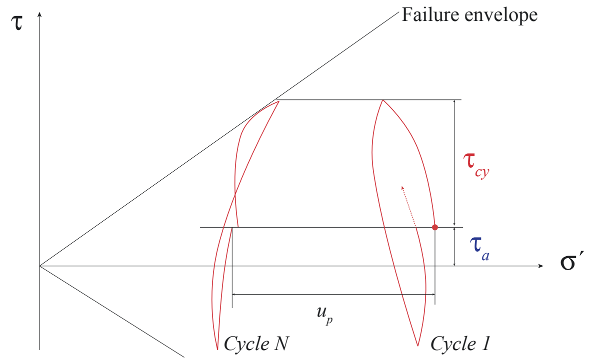

Figure 3: *Effective stress path for undrained cyclic triaxial test.*(Andersen, 2009)

3 Soil and Test Specifications

The Frederikshavn Sand has a minimum and maximum void ratio of $e_{min} = 0.64$ and $e_{max} = 1.05$. The preparation method for the triaxial sample was made by dry tamping to a relative density of $I_D =$ 80 %, using undercompaction with 5 layers. When saturating the specimens, the stiffness of the soil skeleton, i.e. the bulk modulus, K, and the pore pressure level were taken into account (Amar, 1992). Through a consolidation test K was determined to be 108 MPa and it was insured that the samples were at least 99.9 % saturated.

Drained preshearing of 400 cycles with an amplitude of $0.04\,\sigma'_{vc}$ was applied, at an effective mean stress level of 30 kPa, in order to remove any stress concentration from tamping and thereby creating a more homogeneous sample. The effective mean stress was afterwards raised to 60 kPa.

Through an earlier study made on Frederikshavn Sand by Hansson et al. (2005) an expression for the friction angle as a function of relative density, I_D, and confining pressure, σ'_3, was calibrated to

$$\varphi = 0.146\ I_D + 41\ \sigma_3'^{-0.0714} - 1.78° \qquad (1)$$

The expression has been validated by conducting three drained isotropic consolidated monotonic tests with an effective confining pressure in the range between 30 and 120 kPa. The deviation between the results and the expression is in the interval 1-5 %. From the monotonic tests the triaxial friction angle was found to be $\varphi = 39.6°$ for an effective isotropic consolidation stress of 60 kPa. Thereby giving a K_0 value of 0.36. This produces an anisotropic consolidation with an effective vertical consolidation stress, σ'_{vc}, of 166.7 kPa and an effective horizontal consolidation stress, σ'_{hc} of 60 kPa.

The test samples were cylindrical with an initial height, H_0, of 71 mm, and an initial diameter, D_0, of 70 mm, hence H/D ≈ 1. At the cap and base, two rubber membranes with high vacuum grease in between were placed to make the cap and base frictionless. These initiatives were performed in order

Table 1: *Average and cyclic shear stress used in the test programme. Test No. 1 is a monotonic test, and test No. 2-17 is cyclic triaxial tests.*

Test No.	τ_a [kPa]	τ_{cy} [kPa]	u_0 [kPa]
1	400.2	0.0	110.7
2	209.8	185.2	105.8
3	260.2	100.8	109.2
4	166.9	167.2	110.0
5	129.6	99.9	100.0
6	124.9	49.8	110.1
7	78.0	50.2	120.7
8	53.4	17.0	100.2
9	166.6	167.1	302.3
10	49.6	125.5	99.8
11	24.0	50.9	139.7
12	24.6	100.2	100.3
13	24.8	100.5	160.6
14	24.8	100.4	299.7
15	66.0	125.6	99.5
16	84.1	129.4	100.4
17	158.8	216.9	100.4

to ensure homogeneous stress distribution throughout the sample (Ibsen and Lade, 1998a).

During sample preparation, which included installation, pre-shearing and consolidation, it was found that the height decreased with a maximum value of 1 %.

4 Cyclic Test Programme

A total of 17 undraind triaxial tests were conducted; 1 monotonic and 16 cyclic tests. 13 of the cyclic triaxial tests were performed with different combinations of average shear stress, τ_a, and cyclic shear stress, τ_{cy}. These tests are used for constructing the design graphs described in section 6. A complete list of the conducted tests are shown in Table 1

4.1 Cyclic Triaxial Cell

In Figure 4 a sketch of the cyclic triaxial cell is shown. The principle of the system is that a cyclic load is applied via the hydraulic piston at the bottom of the cell.

In order to calculate the stresses and strains in the sample, the following parameters were measured from the triaxial apparatus:

- Axial deformations
- Cell pressure
- Pore pressure
- Piston force

4.2 Test Procedure

As mentioned, the dominating force on offshore wind turbine foundations is wave loads, which have

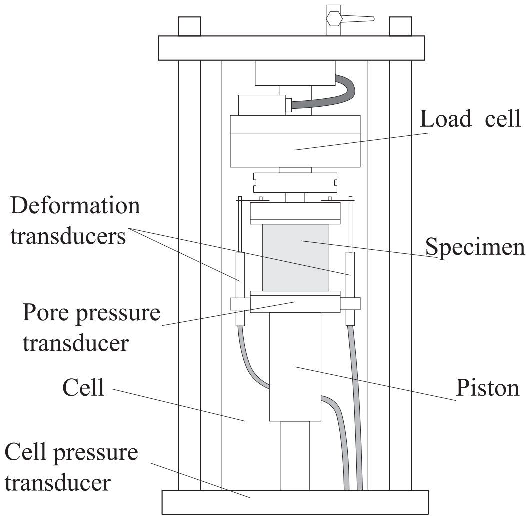

Figure 4: *Illustration of the cyclic triaxial cell.*

a period of 10 to 20 seconds (Lesny, 2010). According to Andersen (2009) the load period on sand seem to have no significant effect when a test is conducted undrained, and therefore the length of the period is only limited by the reaction time of the hydraulic piston. Based on this information the load period was kept as low as practically possible in the range from 10 to 100 seconds, to limit test duration.

To reflect the insitu conditions the sample was anisotropicly consolidated. The process of consolidating the sample and conducting cyclic tests is illustrated in Figure 5, and described in the following. **(a) isotropic consolidation 1**: The sample was set up in the triaxial cell where it was exposed to an isotropic stress level of 30 kPa. **(b) preshearing**: The sample was presheared in order to remove stress concentrations originating from tamping when using the undercompaction method. Preshearing was performed at lower isotropic stress levels, than when the K_0 procedure was applied in order not to consolidate the soil too much during preshearing. **(c) isotropic consolidation 2**: After preshearing the confining pressure was increased to an isotropic stress level of 60 kPa in order to have horizontal stresses corresponding to insitu conditions. **(d) Anisotropic consolidation**: This step is the actual K_0 procedure where the vertical stress was increased so it corresponds to insitu conditions (σ'_{vc} = 166.7 kPa, σ'_{hc} = 60 kPa). **(e) Cyclic loading**: The processes up till cyclic loading were conducted drained. From the K_0 point the increase in average shear stress, $\Delta\tau_a$, and the cyclic shear stress, τ_{cy}, was added undrained.

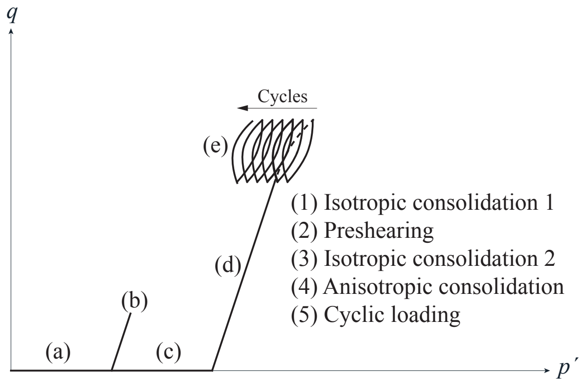

Figure 5: Illustration of test procedure during cyclic triaxial tests.

5 Cyclic Test Results

When analysing the cyclic test results it is observed that the failure modes can be separated into two main groups. One where cyclic shear strain, γ_{cy}, is dominating, and another where permanent shear strain, γ_p, is dominating. A common feature of the tests that fail with dominating γ_p is that they are all subjected to one-way loading, i.e. $\tau_a > \tau_{cy}$. The opposite effect is observed when γ_{cy} is dominating, i.e. $\tau_a < \tau_{cy}$. Another observation is that all one-way loaded tests fail by incremental collapse, while all two-way loaded tests fail by liquefaction. This will be outlined in the following sections.

For all the tests failure is defined as either $\gamma_p = 15$ % or $\gamma_{cy} = 15$ %. A plot of the different tests with number of cycles to failure can be seen in Figure 6.

5.1 Liquefaction

The stress path in the $p' - q$ space for a two-way loaded cyclic test with $\tau_a = 25$ kPa and $\tau_{cy} = 100$ kPa is depicted in Figure 7. The sample is subjected to cyclic loading with an amplitude so large, that the excess pore pressure, u, exceeds the effective mean stresses, p', which becomes zero, and thereby liquefaction occurs. The stress path has the characteristic butterfly shape as described in Randolph and Gouvernec (2011). At liquefaction the sample will start to dilate, which generates negative pore pressure, and effective stresses are again mobilised, and cyclic loading continues.

From Figure 8 it is observed that the initial pore pressure is equal to 300 kPa indicated by point (a), which means that the confining pressure is 360 kPa in order to keep effective mean stresses equal to 60 kPa. As the sample is exposed to more cycles the pore pressure will eventually increase to a value of 360 kPa, indicated by point (b), which is the point where liquefation occurs.

When liquefaction occurs the soil has lost its bearing capacity, which produces large shear deformations as seen in Figure 9. During all the cyclic tests where liquefaction occurs, liquefaction is observed two times in each cycle; once in compression and once in extension. For each time liquefaction occurs, the shear strain increases as cyclic loading continues, as seen in Figure 9.

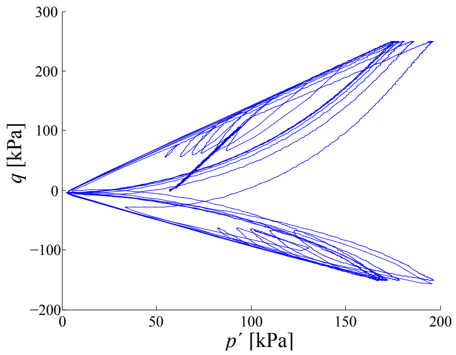

Figure 7: *$p'-q$ diagram for a cyclic triaxial test, where liquefaction is observed. The test failed at N = 8 with τ_a = 25 kPa and τ_{cy} = 100 kPa.*

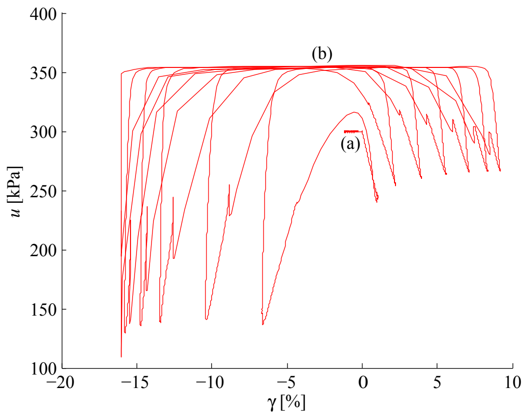

Figure 8: *Excess pore pressure development as a function of cyclic shear strains during cyclic triaxial test. The test failed at N = 8, with τ_a = 25 kPa and τ_{cy} = 100 kPa.*

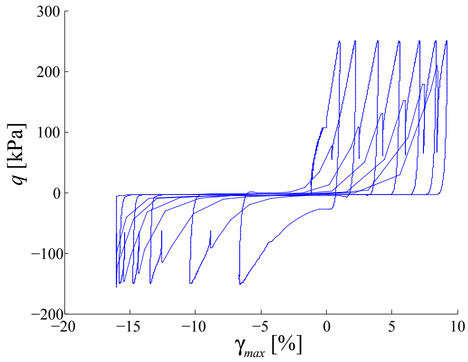

Figure 9: *γ - q diagram for a cyclic triaxial test, where liquefaction is observed. Large shear strains develops when q becomes zero. N = 8, τ_a = 25 kPa and τ_{cy} = 100 kPa.*

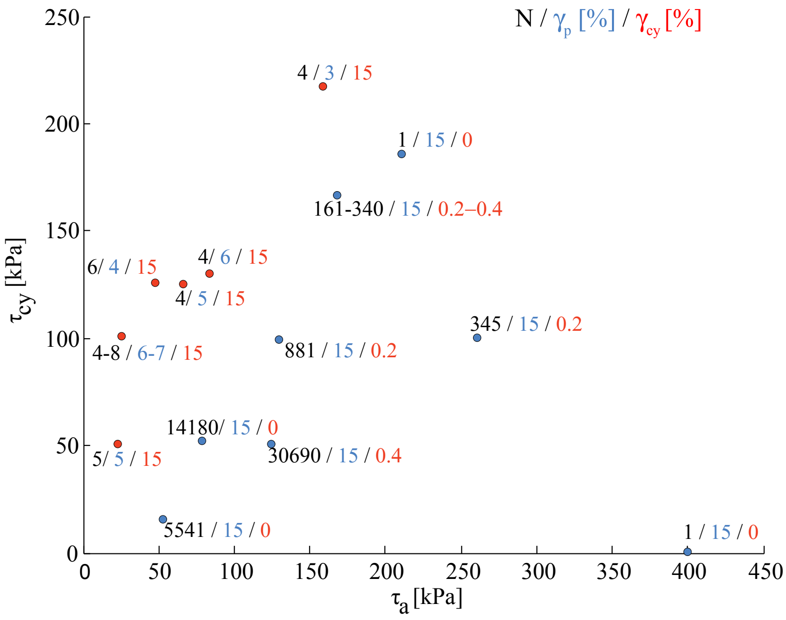

Figure 6: *Test results of the 13 different cyclic triaxial tests and 1 monotonic test.*

5.2 Incremental Collapse

Figure 10 shows a one-way loaded test with $\tau_a = 167$ kPa and $\tau_{cy} = 167$ kPa. The response shows that as cyclic loading is being applied p' decreases, which is due to pore pressure build up. The pore pressure development is illustrated in Figure 11, and it is observed that initially the pore pressure decreases because the sample tries to dilate resulting in an increase in effective mean stresses. As cyclic loading continues the pore pressure starts to increase entailing a reduction in effective mean stresses.

Moreover, from Figure 10 it is observed that the inclination of the cycles becomes steeper as more cycles are applied, which is due to an increase in soil stiffness. This means that γ_{cy} becomes smaller as N increases.

In Figure 12, which shows a γ - q diagram, it is observed that the incremental shear strain decreases, but the total shear strain increases with number of cycles. This type of failure is also defined as incremental collapse by Peralta (2010).

Figure 13 also confirms the statement that the incremental shear strain decreases with increasing number of cycles, while the permanent shear strain increases and eventually resulting in failure at $\gamma_p = 15$ % for $N = 340$ cycles.

6 Design Graphs

When constructing diagrams which can be applied in practical design situations, the average and cyclic shear stress are often normalised with respect to a

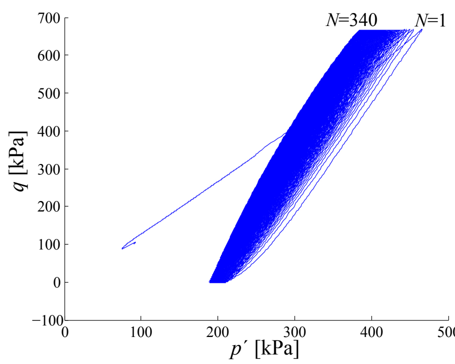

Figure 10: *Stress path in $p' - q$ space. The test is conducted with τ_a = 167 kPa and τ_{cy} = 167 kPa and failed at N = 340 cycles.*

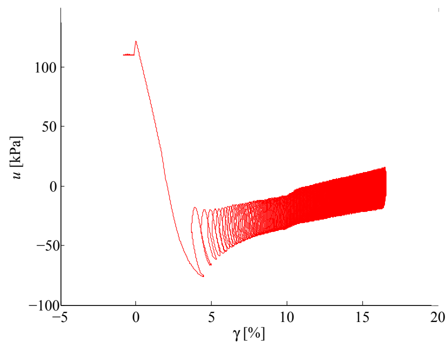

Figure 11: *Pore pressure development as a function of shear strains. The test is conducted with τ_a = 167 kPa and τ_{cy} = 167 kPa and failed at N = 340 cycles.*

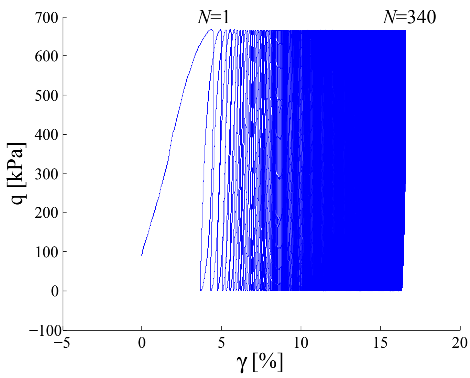

Figure 12: *$\gamma - q$ diagram for a test, which fails under incremental collapse. N = 340 cycles, τ_a = 167 kPa and τ_{cy} = 167 kPa.*

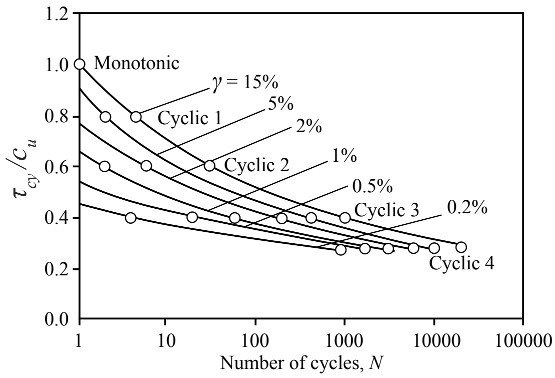

Figure 14: *Strain contour diagram for sand from cyclic simple shear tests with $\tau_a = 0$. (Randolph and Gouvernec, 2011)*

certain stress value. When this normalisation is performed the average and cyclic shear stresses are defined as *Average Load Ratio*, ALR, and *Cyclic Load Ratio*, CLR.

Different authors have proposed various types of design graphs for cyclic loading, which all take the cyclic shear stress into account via the cyclic load ratio. Randolph and Gouvernec (2011) made a *strain contour diagram*, shown in Figure 14, based on 1 undrained monotonic and 4 undrained cyclic simple shear tests on sand performed by Mao (2000). The diagram shows the strain contours as a function of the cyclic load ratio and number of cycles, and can thereby predict the shear strain from cyclic loading. However, during a literature study performed by Shajarati et al. (2012) and also by the conducted cyclic tests, it was found that both the cyclic and average shear stress level are very important, for the cyclic bearing capacity. Therefore strain contour diagrams, which only takes the cyclic load ratio into account, are insufficient for predicting the effects of cyclic loading.

Andersen and Berre (1999) made a study on the effects of cyclic loading, where both the cyclic load ratio and the average load ratio were taken into account. This produced the design graph in Figure 15, which was made for Baskarp sand with a relative density of 95 %. The normalisation in this diagram is performed with the effective vertical consolidation stress, σ'_{vc}, and it can be observed that failure is dependent on the combination of average and shear stresses. It should be noted that in this graph cyclic failure is defined as either 3% cyclic or permanent shear strain, and the tests were conducted with H/D = 2.

When cyclic soil testing is conducted on sand, the cyclic and average shear stress is most often normalised with respect to σ'_{vc}, as shown in Figure 15 (Andersen and Berre, 1999). This is useable under drained conditions since the drained failure envelope is only dependent on the friction angle and effective mean stress, and σ'_{vc} can therefore be used as a normalisation parameter.

In the undrained case however, the undrained shear strength for a dilative sand is not only dependent on the friction angle and mean effective stresses, but also the amount of initial pore pressure (Ibsen and Lade, 1998b). This is due to the fact that the undrained shear strength is influenced by cavitation. Before a dense sand reaches failure (both in tension and extension) it tries to dilate, which generates negative excess pore pressure and thereby an

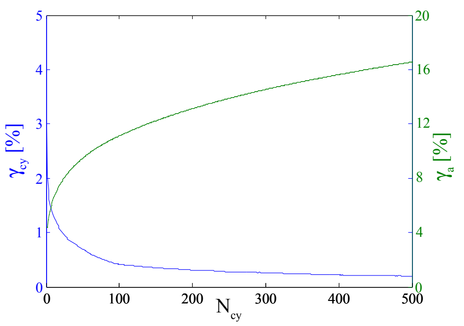

Figure 13: *Number of cycles - γ diagram. N = 340 cycles, τ_a = 167 kPa and τ_{cy} = 167 kPa.*

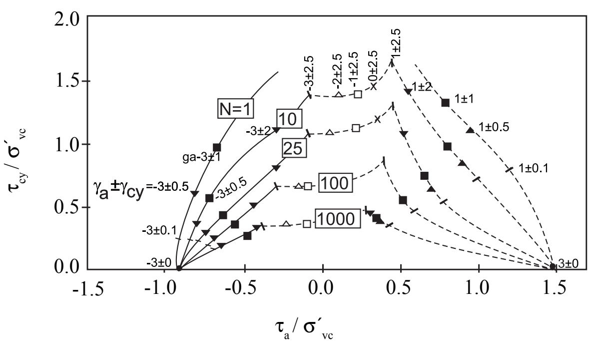

Figure 15: *Strain contour diagram for dense Baskarp sand in the undrained state. (Andersen and Berre, 1999)*

increase in effective stresses. At first this will "eat" the initial pore pressure and afterwards cavitation will occur at around u = -95 kPa, which will lead to failure. Even though this is a well known problem, the normalisation parameter for dense sand in the undrained state is still most often σ'_{vc}, as seen in Figure 15, which does not account for cavitation and the initial pore pressure.

6.1 Undrained Shear Strength

As mentioned σ'_{vc} can in the drained case be related to the drained shear strength, τ_f. The drained shear strength accounts for the friction angle, the effective mean stress and cohesion, and is given as

$$\tau_f = \frac{1}{2} \cdot \frac{6\,\sin\varphi}{3 - \sin\varphi}\,(p' + c'\cot\varphi') \qquad (2)$$

where $c' = 0$ for cohesionless soils. Instead of using σ'_{vc} as a normalisation parameter in the undrained case for sand, the undrained shear strength, c_u, is used. Therefore, the use of the above expression is extended to the undrained case by adding the initial pore pressure, u_0, and the pore pressure at which cavitation occurs u_{cav}, which results in equation (3). Furthermore, the used effective mean stress corresponds to failure in the drained case, p'_{df}.

$$c_u = \frac{1}{2} \cdot \frac{6\,\sin\varphi}{3 - \sin\varphi}\,\left(p'_{df} + u_0 + u_{cav}\right) \qquad (3)$$

The argument for using the above expression is that the undrained bearing capacity for a dense sand is governed by cavitation, as negative pore pressure develops during loading (Ibsen and Lade, 1998b). It is therefore important to include the pore pressure when calculating c_u in the undrained case for sand. The effect of adding the initial pore pressure, u_0, and the pore pressure at cavitation, u_{cav}, is illustrated in Figure 16. The figure illustrates the effective stress paths for two examples with the same initial effective mean stress, p'_0. The two examples end up having a different undrained shear strength, because of differences in initial pore pressure. Following the total stress path will lead to drained failure in point (a), which is the point where p'_{df} is measured. From this point the amount of initial pore pressure and the pore pressure at cavitation is added to p'_{df}. This means that a higher amount of initial pore pressure will lead to a higher value of the undrained shear strength before failure is reached, which is illustrated by point (b) and (c).

6.2 Modified Design Graph

Based on the expression for undrained shear strength in equation (3), a *modified design diagram* is constructed for the Frederikshavn Sand in the undrained case with I_D = 80 %. The modified design diagram is based on the 17 conducted tests and normalised with respect to c_u, as shown in Figure 17. It is seen that the graph shares the same tendency as the design graph by Andersen and Berre (1999) in Figure 15. However, an important feature of the modified design graph is that it accounts for the initial pore pressure, which is important when dealing with the undrained bearing capacity.

To illustrate the limitations of the design graph when normalising with σ'_{vc} as proposed by Andersen and Berre (1999), a comparison between the two design graphs can be seen in Figure 18. To make the comparison, three cyclic tests were conducted with the same average shear stress, τ_a = 25 kPa, and same cyclic shear stress, τ_{cy} = 100 kPa, but with different values of initial pore pressure, u_0, namely 100, 160 and 300 kPa. The calculated cyclic and average load ratios for the two design graphs can be seen in Table 2.

Table 2: *Three cyclic tests with τ_a = 25 kPa, τ_{cyc} =100 kPa and different initial pore pressure, u_0.*

	Design Graph		Modified Design Graph	
u_0	τ_a/σ'_{vc}	τ_{cy}/σ'_{vc}	τ_a/c_u	τ_{cy}/c_u
100 kPa	0.15	0.6	0.07	0.29
160 kPa	0.15	0.6	0.06	0.26
300 kPa	0.15	0.6	0.05	0.20

Figure 18(a) plots the three tests in the same point since they have the same ALR and CLR when normalising with σ'_{vc}. However, Figure 18(b) normalises with c_u and plots the three tests in different positions, because ALR and CLR is dependent on the initial pore pressure. The example given above illustrates that it is very important to construct a design diagram in a manner which represent the in-situ conditions as good as possible. Therefore, if the drained state is the design case it is sufficient to apply σ'_{vc} as a normalisation parameter. On the other hand if the undrained state is the design case, the initial pore pressure should be taken into consideration, and therefore c_u should be used when normalising the design diagram.

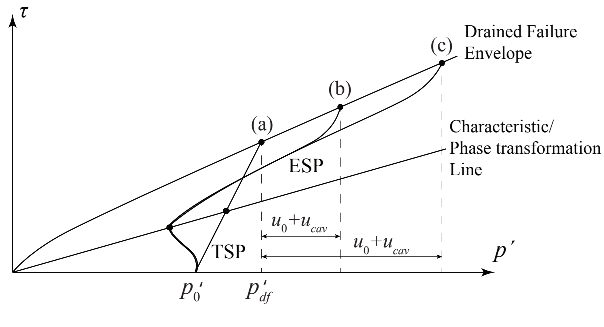

Figure 16: *Illustration of the theoretically effect of including initial pore pressure and the pore pressure at cavitation to the drained failure criterion.*

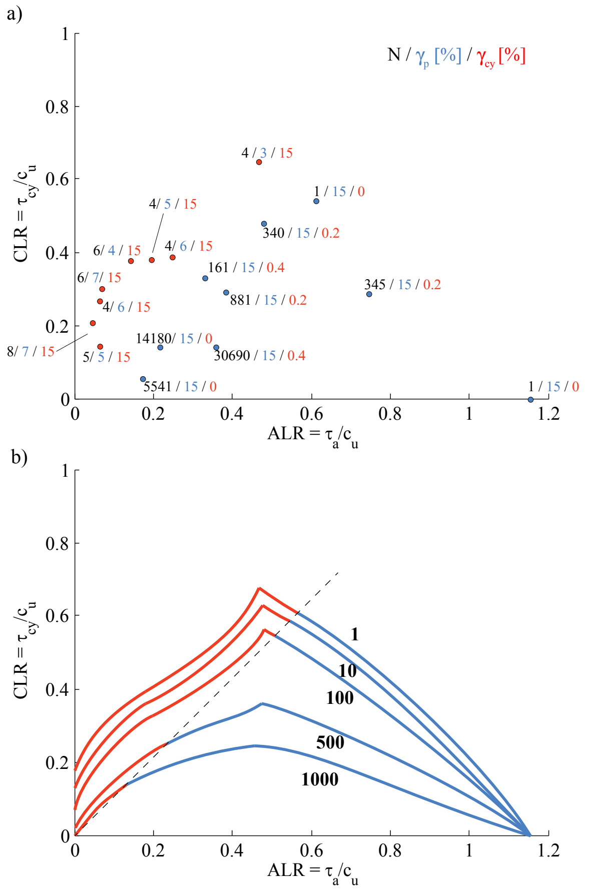

Figure 17: *Modified design diagram for Frederikshavn Sand in the undrained case with I_D = 80 %. Red corresponds to two-way loading, while blue is one-way loading.*

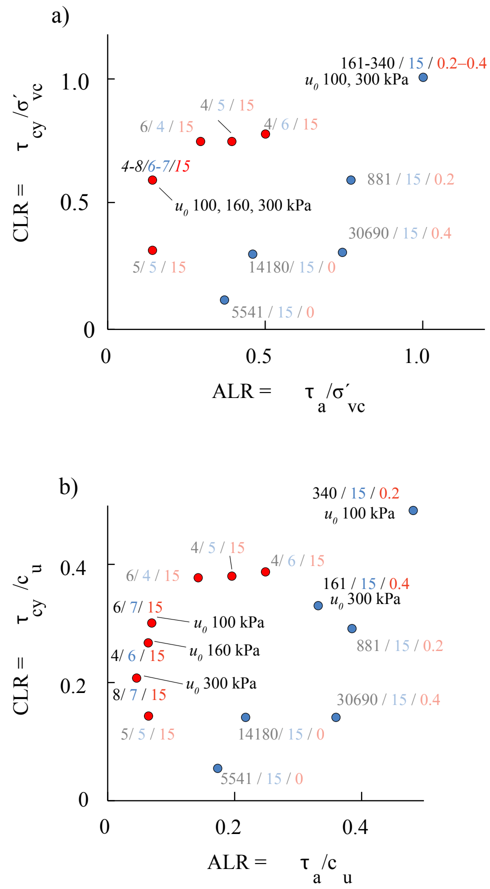

Figure 18: *Comparison between design graphs. (a) Normal design graph (σ'_{vc}). (b) Modified design graph (c_u)*

7 Conclusion

A modified design diagram is created for the Frederikshavn Sand in the undrained case for a relative density of $I_D = 80$ %. It can be used to estimate the number of cycles to failure for a given combination of pore pressure, average and cyclic load ratio.

When normalising cyclic and average shear stresses for use in design diagrams σ'_{vc} is found insufficient to use as a normalisation parameter in the undrained case, as it does not take pore pressure into account. This is important, since the undrained shear strength for a dense sand is governed by cavitation. Therefore the undrained shear strength, c_u, is used as a normalisation parameter for the modified design graph and should be used for other design graphs in the undrained case.

When comparing Figure 15 and Figure 17 a considerable difference is observed at ALR = 0. The difference can be explained by a large difference in applied back pressure. In the tests performed by Andersen and Berre (1999) a backpressure in the range from 500 - 1800 kPa was applied. Compared to the tests conducted to make Figure 17 with a backpressure at around 100 kPa, the limit in τ_{cy} without reaching cavitation is raised significantly. This makes it possible to perform tests with a load ratio combination of $\tau_a/\sigma'_{vc} = 0$ and $\tau_{cy}/\sigma'_{vc} = 1.5$. If the same test is performed with a low back pressure, cavitation will occur, and the test will correspond to a monotonic test. This observation strengthens the argument, for choosing c_u as the normalisation parameter for the undrained case.

References

Amar, **1992**. Samuel Amar. *Triaxial testing.* Divisions de Mecanique des sols et Foundations, (Re.document no. ETC5-N 91.12), 1992.

Andersen, **2009**. Knut H. Andersen. *Bearing capacity under cyclic loading - offshore, along the coast, and on land. The 21st Bjerrum Lecture presented in Oslo, 23 November 2007.* Canadian Geotechnical Journal, 46(5), pp. 513–535, 2009.

Andersen and Berre, **1999**. Knut H. Andersen and Torlav Berre. *Behaviour of a dense sand under monotonic and cyclic loading.* ECSMGE XII Geotechnical Engineering for Transportation Infrastructure. Proc.,, 2, pages 667–676, 1999.

Hansson, Hjort, and Thaarup, **2005**. Martin Hansson, Troels H. Hjort, and Martin Thaarup. *Static and transient loading of the bucket foundation for offshore wind-turbines.* M.Sc. Thesis, Aalborg University, 2005.

Ibsen and Lade, **1998a**. Lars Bo Ibsen and Poul Lade. *The Role of the Characteristic Line in Static Soil Behavior.* Localization and Bifurcation Theory for Soils and Rocks, pages 221–230, 1998.

Ibsen and Lade, **1998b**. L.B. Ibsen and P.V. Lade. *The Strength and Deformation Characteristics of Sand Beneath Vertical Breakwaters Subjected to Wave Loading.* AAU Geotechnical Engineering Papers, (Soil Mechanics Paper No. 23), 1998.

Lesny, **2010**. Kerstin Lesny. *Foundations for Offshore Wind Turbines.* ISBN: 978-3-86797-042-6, 1. Edition. VGE Verlag GmbH, 2010.

Mao, **2000**. X. Mao. *The Behaviour of Three Calcareous Soils in Monotonic and Cyclic Loading.* Ph.D. Thesis, University of Western Australia, 2000.

Peralta, **2010**. Proserpine K. Peralta. *Dissertation: Investigations on the Behavior of Large Diameter Piles under Long-Term Lateral Cyclic Loading in Cohesionless Soil*, 2010.

Randolph and Gouvernec, **2011**. M. Randolph and S. Gouvernec. *Offshore Geotechnical Enigineering.* ISBN13: 978-0-415-47744-4, 1. Edition. Spon Press, 2011.

Shajarati, Sørensen, Nielsen, and Ibsen, **2012**. Amir Shajarati, Kris W. Sørensen, Søren K Nielsen, and Lars Bo. Ibsen. *Manual for Cyclic Triaxial Test.* ISSN: 1901-726X, DCE Technical Repor No. 114. Aalborg University, 2012.

Article 3

Modified Critical State Two-Surface Plasticity Model for Sands

Modified Critical State Two-Surface Plasticity Model for Sands

Kris Wessel Sørensen
Søren Kjær Nielsen
Amir Shajarati
Johan Clausen

ISSN 1901-7278
DCE Technical Memorandum No. 16

AALBORG UNIVERSITY
Department of Civil Engineering

Aalborg University
Department of Civil Engineering
Geotechnical Engineering

DCE Technical Memorandum No. 16

Modified Critical State Two-Surface Plasticity Model for Sands

by

Kris Wessel Sørensen
Søren Kjær Nielsen
Amir Shajarati
Johan Clausen

June 2012

Scientific Publications at the Department of Civil Engineering

Technical Reports are published for timely dissemination of research results and scientific work carried out at the Department of Civil Engineering (DCE) at Aalborg University. This medium allows publication of more detailed explanations and results than typically allowed in scientific journals.

Technical Memoranda are produced to enable the preliminary dissemination of scientific work by the personnel of the DCE where such release is deemed to be appropriate. Documents of this kind may be incomplete or temporary versions of papers—or part of continuing work. This should be kept in mind when references are given to publications of this kind.

Contract Reports are produced to report scientific work carried out under contract. Publications of this kind contain confidential matter and are reserved for the sponsors and the DCE. Therefore, Contract Reports are generally not available for public circulation.

Lecture Notes contain material produced by the lecturers at the DCE for educational purposes. This may be scientific notes, lecture books, example problems or manuals for laboratory work, or computer programs developed at the DCE.

Theses are monograms or collections of papers published to report the scientific work carried out at the DCE to obtain a degree as either PhD or Doctor of Technology. The thesis is publicly available after the defence of the degree.

Latest News is published to enable rapid communication of information about scientific work carried out at the DCE. This includes the status of research projects, developments in the laboratories, information about collaborative work and recent research results.

Published 2012 by
Aalborg University
Department of Civil Engineering
Sohngaardsholmsvej 57,
DK-9000 Aalborg, Denmark

Printed in Aalborg at Aalborg University

ISSN 1901-7278
DCE Technical Memorandum No. 16

Modified Critical State Two-Surface Plasticity Model for Sands

Kris Wessel Sørensen[1] Søren Kjær Nielsen[1] Amir Shajarati[1] Johan Clausen[2]

Department of Civil Engineering, Aalborg University

Abstract

This article describes the outline of a numerical integration scheme for a critical state two-surface plasticity model for sands. The model is slightly modified by LeBlanc (2008) compared to the original formulation presented by Manzari and Dafalias (1997) and has the ability to correctly model the stress-strain response of sands. The model is versatile and can be used to simulate drained and undrained conditions, due to the fact that the model can efficiently calculate change in void ratio as well as pore pressure. The objective of the constitutive model is to investigate if the numerical calculations can be performed with the Forward Euler integration scheme. Furthermore, the model is formulated for a single point.

1 Introduction

With the rapidly growing increase in computational power over the last decades, constitutive models that accurately simulate the stress-strain behaviour of different materials have been used within different engineering fields. However, for granular materials only simple classical plasticity models such as Mohr-Coulomb or Cam-Clay have been widely used in most engineering codes. These models may be sufficient for many simple geotechnical problems, but fail to simulate accurate stress-strain behaviour when dealing with complex problems. Therefore more advanced models are required when dealing with offshore geotechnical problems. Effects from cyclic loading such as accumulation of pore pressure, cyclic liquefaction and cyclic mobility are typically needed to be taken into account.

The framework of Critical State Soil Mechanics (CSSM) developed by Schofield and Wroth (1968) provides a broad framework to explain the fundamental behaviour of different soil materials. Within this framework, Manzari and Dafalias (1997) developed a versatile constitutive model named *Critical State Two-Surface Plasticity Model for Sands*, that is able to model both drained an undrained behaviour of cohesionless soils subjected to cyclic loading. LeBlanc (2008) made modifications to the model by introducing an alternative multi-axial surface formulation based on shape functions used to prescribe a family of smooth and convex contours in the octhahedral plane.

This article outlines the physical aspects of the model proposed by LeBlanc (2008), and seeks to describe the different model parameters. When implementing the constitutive model, a simple integration scheme in form of *Forward Euler* is used instead of the proposed *Return Mapping Method* used by LeBlanc (2008). This is done in order to simplify the calculations and investigate if the accuracy of the model is still preserved.

2 Formulation of Model

The following section describes the modified critical two-surface plasticity model for sands in detail, and has its point of reference in LeBlanc (2008).

2.1 Peak Shear Strength

A dense sand specimen will dilate when sheared and therefore has a larger shear strength due to the increased amount of energy needed in order to get the granular particles to slide over adjacent particles. The peak shear strength described as the upper limit in a stress space, normally known as the failure envelope, is in the model described as a *bounding line*. At high effective mean stresses the bounding line will coincide with the critical state line. The bounding line as well as the critical state line can be seen in Figure 1, where the bounding line for a dense sample is curved due to the increased peak shear strength.

The path of the bounding line is highly dependent on the void ratio, and therefore the shape of the bounding line is formulated by the *state parameter*, ψ, along with the *critical stress ratio*, M_{cr}. The state parameter in equation (1) is defined as the difference between the current void ratio, e, and the critical void ratio, e_{cr}, and is shown in Figure 2. The state parameter is used in the constitutive model

[1] *M.Sc. Student, Department of Civil Engineering, Aalborg University, Denmark*

[2] *Associate Professor, Department of Civil Engineering, Aalborg University, Denmark*

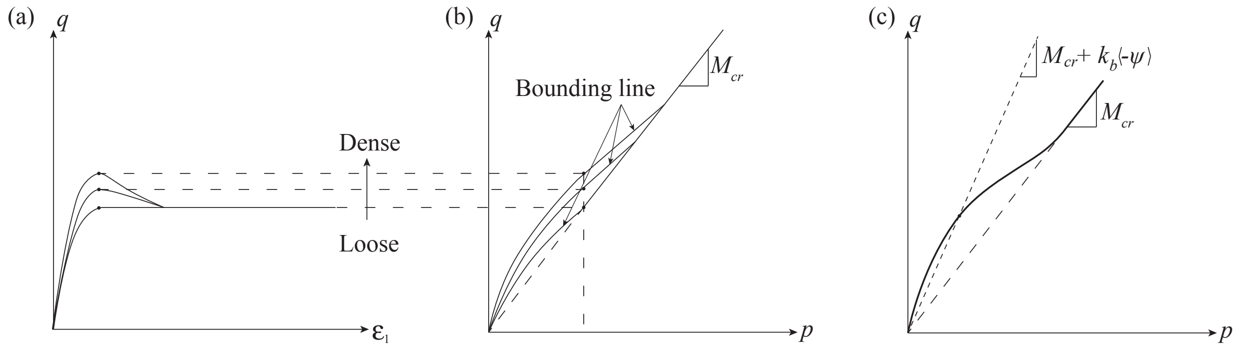

Figure 1: *Peak shear strength (failure envelope) for different deposit densities. (a) $\varepsilon_1 - q$ diagram. (b) $p - q$ diagram (Cambridge diagram). (c) Model formulation of bounding line.*

to prescribe the peak stress level and dilatancy behaviour.

$$\psi = e - e_{cr} \tag{1}$$

The critical stress ratio prescribes the inclination of the critical state line, and is defined as the ratio between the deviatoric and mean stresses, $M_{cr} = q/p$. The critical stress ratio along with the state parameter results in the bounding line, M_b, which is formulated as

$$M_b(\psi) = M_{cr} + k_b \langle -\psi \rangle \tag{2}$$

where k_b is a dimensionless model parameter and $\langle\ \rangle$ is defined as Macauly brackets where $\langle x \rangle = 0$ if $x < 0$ else $\langle x \rangle = x$.

2.2 Characteristic Line

To model the change from compactive to dilative behaviour the use of *characteristic line* is implemented into the model. For monotonic tests this behaviour can be represented by a straight line through origo in p - q space and is independent of relative density (Ibsen, 1998). However, when dealing with cyclic loading a reformulation of the characteristic line is needed because the line is no longer constant and independent of relative density according to Manzari and Dafalias (1997). Therefore the definition of the characteristic line is also formulated by the critical stress ratio and the state parameter, given as

$$M_c(\psi) = M_{cr} + k_c \psi \tag{3}$$

where k_c is a dimensionless model parameter and the characteristic line is illustrated in Figure 3.

2.3 Stress Dependent Moduli

Both the bulk modulus, K, and the shear modulus, G, are stress dependent, and in order to take this dependency into account, the model uses the following equations

$$K = K_0 \left(\frac{p}{p_{ref}} \right)^b \qquad G = G_0 \left(\frac{p}{p_{ref}} \right)^b \tag{4}$$

where p_{ref} is the reference pressure for which $K = K_0$ and $G = G_0$. The pressure exponent, b, is a model parameter expressing the variation of the elastic modules with the isotropic pressure. The value of b is reported to vary from 0.435, at very

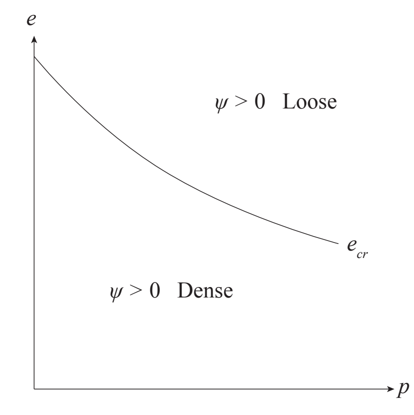

Figure 2: *State parameter used to model peak shear stress and dilatancy behaviour.*

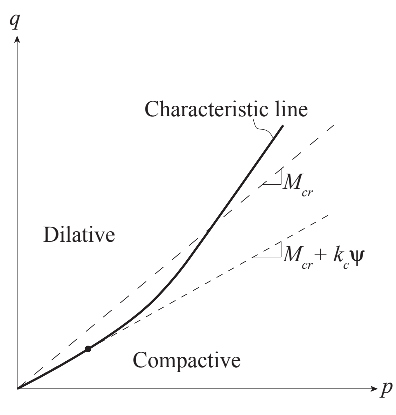

Figure 3: *Characteristic line accounting for the transition from compactive to dilative soil behaviour.*

small strains, to 0.765, at very large strains according to Wroth et al. (1979). A value of 0.5 captures most of the important features of increased shear stiffness with pressure (Wroth and Houlsby, 1985).

2.4 Yield Surface

The constitutive model has its underlying basis in non-associated plasticity and the elastic domain is enclosed by a yield surface with the function given in equation (5). The yield surface has a cone type shape and has its origin positioned in origo, see Figure 4. It should be noted that bold letters characterise tensors and the operators $\mathbf{u}$:$\mathbf{v}$ and $|u|$ refer to the tensor product and tensor norm, respectively. Moreover $p = (\sigma_{11} + \sigma_{22} + \sigma_{33})/3$ and $\boldsymbol{s} = \boldsymbol{\sigma} - p\boldsymbol{I}$ refer to the hydrostatic stress and the deviatoric stress tensor, where $\boldsymbol{I}$ is the identity matrix.

$$f = |\boldsymbol{r}| - \sqrt{\frac{2}{3}}mp \qquad \boldsymbol{r} = \boldsymbol{s} - p\,\boldsymbol{\alpha} \tag{5}$$

The value $\sqrt{\frac{2}{3}}m$ and $\boldsymbol{\alpha}$ define the radius and axis direction of the cone respectively.

The normals to the yield surface, $\partial f/\partial\boldsymbol{\sigma}$, and plastic potential surface, $\partial g/\partial\boldsymbol{\sigma}$, defining the direction of the loading and plastic flow direction are defined as

$$\frac{\partial f}{\partial\boldsymbol{\sigma}} = \boldsymbol{n} - \frac{1}{3}N\boldsymbol{I} \tag{6}$$

$$\frac{\partial g}{\partial\boldsymbol{\sigma}} = \boldsymbol{n} + \frac{1}{3}D\boldsymbol{I} \tag{7}$$

where $\mathbf{n} = \mathbf{r}/|\mathbf{r}|$ is the deviatoric normal to the yield surface as shown in Figure 4. N and D are parameters which determine the magnitude of the isotropic components. The latter is a dilatancy parameter and it controls the isotropic flow direction and thereby the volumetric behaviour of the constitutive model.

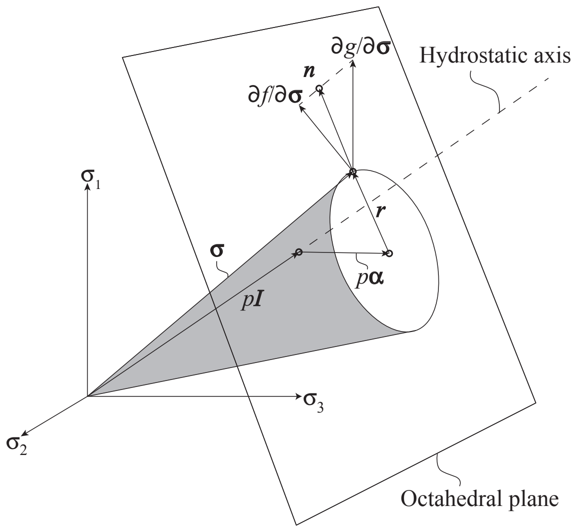

Figure 4: *Illustration of yield surface.*

2.5 Volumetric Behaviour

The magnitude of the isotropic components can be determined by equation

$$N = \boldsymbol{\alpha} : \boldsymbol{n} + \frac{2}{3}m \tag{8}$$

$$D = (A_0 + A_z)(\boldsymbol{\beta_c} : \boldsymbol{n}) \tag{9}$$

where $A_z = \langle \boldsymbol{z} : \boldsymbol{n} \rangle$ is an unloading dilatancy parameter, which allows the model to take dilatancy during unloading into account and is dependent on the fabric tensor $\boldsymbol{z}$. Furthermore, A_0 is a dimensionless scaling parameter also accounting for dilantancy. The sign of $\boldsymbol{\beta_c} : \boldsymbol{n}$ defines the limit between compressive and dilative behaviour. $\boldsymbol{\beta_c} : \boldsymbol{n} > 0$ indicates stress states inside the characteristic surface and therefore compressive behaviour, whereas loading beyond the characteristic surface gives $\boldsymbol{\beta_c} : \boldsymbol{n} < 0$ and therefore dilative behaviour. The development of the fabric tensor, $\boldsymbol{z}$, is defined by the evolution law

$$d\boldsymbol{z} = \tilde{\boldsymbol{z}}d\lambda \qquad \tilde{\boldsymbol{z}} = -C_z(A_z^{max}\boldsymbol{n} + \boldsymbol{z})\,\langle -D \rangle \tag{10}$$

The two parameters C_z and A_z^{max} are positive dimensionless model parameters, and A_z^{max} becomes an upper threshold for A_z. $\boldsymbol{z}$ enables the model to dilate under reversed loading and develop accordingly. $\boldsymbol{z}$ evolves in an opposite direction of $\boldsymbol{n}$ whenever the specimen dilates ($D > 0$) such that the tensor product $\boldsymbol{z} : \boldsymbol{n}$ becomes positive, only when the load direction shifts to unloading.

2.6 Kinematic and Isotropic Hardening

The kinematic evolution law is based on the expression given in equation (11). C_α is a positive model parameter and $b_r = 2\sqrt{2/3}(M_b - m)$ and must abide $b_r > |\boldsymbol{\beta_b} : \boldsymbol{n}|$. The rate of evolution will converge to zero as $\boldsymbol{\alpha}$ approaches the bounding surface which implies that the stress state remains inside the bounding surface during hardening.

$$d\boldsymbol{\alpha} = \tilde{\boldsymbol{\alpha}}d\lambda \qquad \tilde{\boldsymbol{\alpha}} = C_\alpha \left(\frac{|\boldsymbol{\beta_b} : \boldsymbol{n}|}{b_r - |\boldsymbol{\beta_b} : \boldsymbol{n}|} \right) \boldsymbol{\beta_b} \tag{11}$$

The size of the plastic multiplier, $\Delta\lambda$, can be determined from equation

$$\Delta\lambda = \frac{f(\boldsymbol{\sigma})}{\partial f/\partial\boldsymbol{\sigma} : \boldsymbol{C} : \partial g/\partial\boldsymbol{\sigma} + H} \tag{12}$$

where $\boldsymbol{C}$ is the hypoelastic constitutive matrix and H is the hardening module, which is determined from

$$H = p\left(\boldsymbol{n} : \tilde{\boldsymbol{\alpha}} + \sqrt{\frac{2}{3}}\tilde{m} \right) \tag{13}$$

2.7 Multi-axial Formulation

Granular materials are strongly dependent on the third deviatoric stress invariant, which can be proven by comparing triaxial compression and extension tests, which shows that a lower shear strength can be sustained in triaxial extension. In order to account for the third stress invariant and thereby a more correct behavioural simulation of granular materials, the bounding and characteristic lines are reformulated into bounding and characteristic surfaces defined in a multi-axial stress space. The bounding and characteristic surfaces are described by a versatile shape function, $g(c, \theta)$, which was first presented by Krenk (1996). The formulation is based on the second, J_2, and third, J_3, deviatoric stress invariants and the Lode angle, θ. The shape function is defined as

$$g(c, \theta) = \frac{\cos(\gamma)}{\cos\left(\frac{1}{3}\arccos\left(\cos(3\gamma)\cos(3\theta)\right)\right)} \quad (14)$$

$$\gamma = \frac{\pi}{3} + \arctan\left(\frac{1-2c}{\sqrt{3}}\right) \quad (15)$$

$$\cos(3\theta) = \frac{3\sqrt{3}}{2}\frac{J_3}{(J_2)^{\frac{3}{2}}} \quad (16)$$

The shape parameter, c, can attain any value between 0.5 and 1. A value equal to 1 produces a circular surface contour in the octahedral plane and a value of 0.5 produces a triangle. Any value in between creates a cross between the two shapes as seen in Figure 5.

2.8 Image Points

The constitutive model is formulated by applying image points, $\boldsymbol{\alpha}_i$, which defines points on a surface in the octahedral plane, pointing from the hydrostatic axis to the image point in the direction of $\mathbf{n}$, see equation (17) and Figure 6. These image points are used in the formulation to model dilatancy and the evolution laws for hardening parameters.

$$\boldsymbol{\alpha}_i = \sqrt{\frac{2}{3}}\left(g(c_i, \theta_{\boldsymbol{n}})M_i(\psi) - m\right)\boldsymbol{n}, \quad i = b, c \quad (17)$$

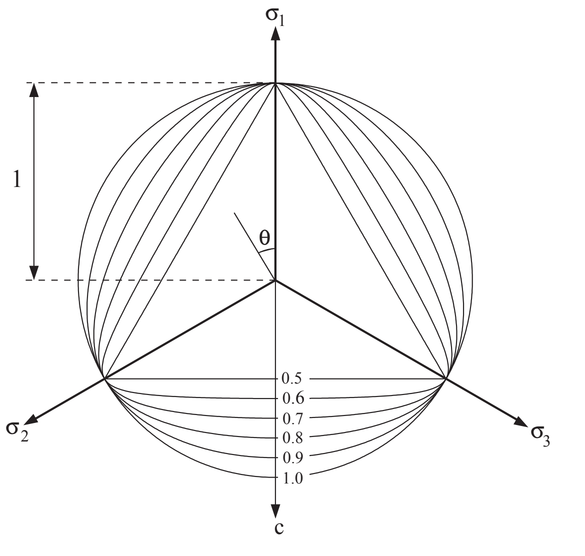

Figure 5: *Family of shape contours prescribed by the shape function $g(c, \theta)$.*

3 Integration Scheme

When an integration scheme is used the infinitesimal changes, $d\boldsymbol{\sigma}$, now becomes finite, $\Delta\boldsymbol{\sigma}$. This implies that the constitutive relation can be expresses as

$$\Delta\boldsymbol{\sigma}_{j+1} = \boldsymbol{D}^{ep}(\boldsymbol{\sigma}_j)\,\Delta\,\boldsymbol{\varepsilon}_{j+1} \quad (18)$$

The Forward Euler integration scheme is choosen, of which the principles for updating the stress tensor can be expressed as

$$\boldsymbol{\sigma}_{j+1} = \boldsymbol{\sigma}_j + \Delta\boldsymbol{\sigma}_{j+1} \quad (19)$$

This implies that the stress increment, $\Delta\boldsymbol{\sigma}$, only depends on the previous stress state j. This is problematic as the scheme may lead to stresses outside the yield surface, which can not exist. In the Forward Euler integration scheme these errors are not corrected. Errors may therefore accumulate and stresses drift away from the yield surface, as more steps are taken, as illustrated in Figure 7. When the step length is reduced the error is reduced as well, hence this method demands a relative small step length, which require a lot of computational power (Krabbenhøft, 2002).

3.1 Implementation strategy

In general the course of action regarding the implementation of the model is outlined in Table 1, where $\mathbf{D}^*$ is either the elastic, $\mathbf{D}^{el}$, or elasto-plastic, $\mathbf{D}^{ep}$, constitutive tensor dependent on elastic or plastic material response.

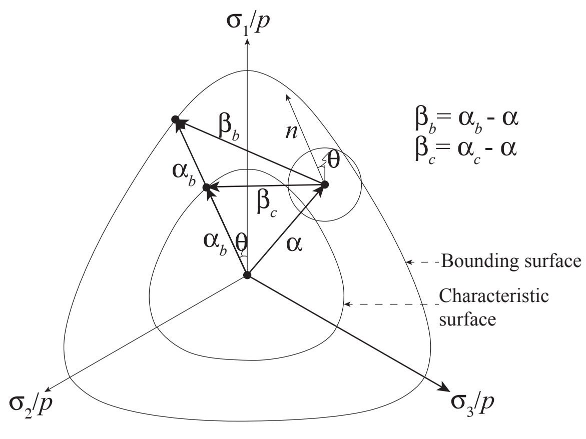

Figure 6: *Illustration of bounding, characteristic and yield surface in the octahedral plane.*

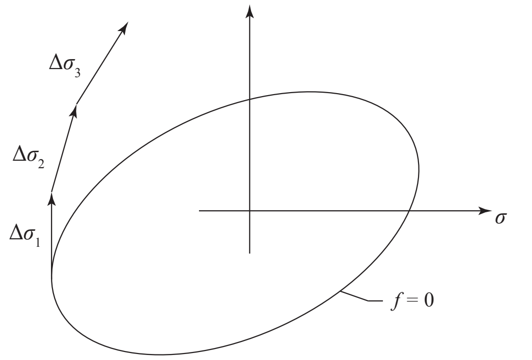

Figure 7: *Illustration of errors by using the Forward Euler integration scheme. (Krabbenhøft, 2002)*

Table 1: *Procedure regarding the implementation of the Forward Euler integration scheme to the modified two-surface elasto-plasticity model.*

Modified Manzari (Forward Euler)

Initial state:

$\boldsymbol{\alpha_0}$, c_b, c_c, b, G_0, K_0, p_{ref}
m_0, A_0, A_z, $\mathbf{z}$, C_z, A_z^{max}, C_α, $\mathbf{D}_0^*$

Iterations $i = 1, 2, ..., i_{max}$
Given parameters: $\Delta\varepsilon_{1,i}$, $\Delta\sigma_{2,i}$, $\Delta\sigma_{3,i}$

Calculate unknown stresses and strains from $\mathbf{D}^*$:
$\Delta\varepsilon_{3,i}$, $\Delta\varepsilon_{2,i}$, $\Delta\sigma_{1,i}$

Determine hydrostatic-, deviatoric stress and yield function:
$\mathbf{s}$, p, $\mathbf{r}$, $f(\boldsymbol{\sigma})$

if $f(\boldsymbol{\sigma}) < 0$
$\mathbf{D}^* = \mathbf{D}^{el}$

else:
θ, γ, g, M_b, M_c, α_b, α_c, β_b, β_c, N, $\frac{\partial f}{\partial \boldsymbol{\sigma}}$, A_z, D_{dil}, $\tilde{\boldsymbol{z}}$, $\frac{\partial g}{\partial \boldsymbol{\sigma}}$, $\Delta\lambda$, $\tilde{\boldsymbol{\alpha}}$

$$\mathbf{D}^* = \mathbf{D}^{ep} = \boldsymbol{D} - \frac{\boldsymbol{D}\frac{\partial g}{\partial \boldsymbol{\sigma}}\frac{\partial f}{\partial \boldsymbol{\sigma}}^T\boldsymbol{D}}{H + \frac{\partial f}{\partial \boldsymbol{\sigma}}^T\boldsymbol{D}\frac{\partial g}{\partial \boldsymbol{\sigma}}}$$

Update Variables:
$\boldsymbol{\alpha} = \boldsymbol{\alpha} + \Delta\lambda\tilde{\boldsymbol{\alpha}}$
$\mathbf{z} = \mathbf{z} + \Delta\lambda\tilde{\mathbf{z}}$

end

4 Efficiency, Accuracy and Stability

The Forward Euler integration scheme is evaluated on efficiency, accuracy and stability to evaluate the performance and determine if the integration scheme in Table 1 is applicable for this particular model. Simulations of drained monotonic and cyclic tests are performed for the analysis. The adopted model parameters are based on the original formulation of the constitutive model by Manzari and Dafalias (1997) and can be seen in Table 2.

Table 2: *Model parameters adopted for analysis of efficiency, accuracy and stability.*

K_0=31.4 MPa	M_c=1.1	k_b=4.0	A_0=2.64
G_0=31.4 MPa	λ=0.025	k_c = 4.2	A_z^{max}=100
	e_r=0.93	C_α=1200	C_z=100

Both the monotonic and cyclic tests simulates a medium-dense sample with a mean stress of $p = 60$ kPa with ε_1 ranging from 0 - 10 %. The simulations are illustrated in Figures 8 and 10. To evaluate the accuracy of the integration scheme an error measure is used, defined by

$$error = \frac{1}{N}\sum_{i=1}^{N}\frac{|\boldsymbol{\sigma}_i - \boldsymbol{\sigma}_{i,exact}|}{\boldsymbol{\sigma}_{i,exact}} \tag{20}$$

where N is the number of steps and $\boldsymbol{\sigma}_{i,exact}$ refers to the exact solution approximated by simulations having a very small step size and where convergence has occurred. The accuracy is measured as a function of the imposed strain increments, $\Delta\varepsilon_1$. The results are listed in Table 3.

Table 3: *Results from accuracy analysis of the Forward Euler integration scheme, applied at the Modified Critical State Two-Surface model (1-6) and a Drucker Prager model with non linear isotropic hardening (DP1-DP4).*

No.	Loading	N	$\Delta\varepsilon_1$	Error [%]
1	Monot.	10,000	10^{-5}	21.41
2	Monot.	100,000	10^{-6}	13.39
3	Monot.	1,000,000	10^{-7}	1.18
4	Cyclic	10,000	10^{-5}	42.05
5	Cyclic	100,000	10^{-6}	22.71
6	Cyclic	1,000,000	10^{-7}	Unstable
DP1	Monot.	10	10^{-2}	2.24
DP2	Monot.	100	10^{-3}	0.26
DP3	Monot.	1000	10^{-4}	0.07
DP4	Monot.	10000	10^{-5}	0.01

4.1 Monotonic CD Response

For the monotonic simulations a triaxial compression test has been simulated. A convergence analysis proved that an accurate simulation is performed with an increment in the order of $\Delta\varepsilon_1 = 10^{-8}$, which is a rather small increment size and therefore demands relatively large computational costs at the expense of efficiency. Larger increments have been attempted to improve the efficiency, but the approximated solution diverges too far away from the exact solution and the error becomes too large, as seen in Table 3.

The convergence rate for the Modified Critical State Two-Surface model is compared with a Drucker Prager constitutive model with nonlinear isotropic hardening, where the Forward Euler integration scheme also is applied. The ε_1 - q diagram is depicted in Figure 9, and the relative error is given in Table 3. From this it is seen that convergence is reached with a step length of 10^{-3} to 10^{-4}, which is much faster than the Modified Critical State Two-Surface model, which need increments smaller than 10^{-7} to obtain convergence. This indicate that when the complexity of a constitutive model increases, the needed step size and thereby the usability of the Forward Euler integration scheme decreases. This makes the importance of return mapping more relevant, when constitutive models becomes more complex.

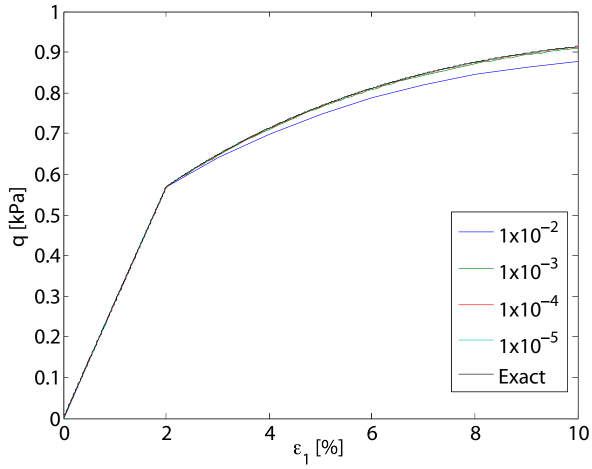

Figure 9: *Results of monotonic simulation with Drucker Prager model with nonlinear isotropic hardening and the accuracy of different strain increments.*

4.2 Cyclic CD Response

When simulating cyclic response the model shows reasonably good stress-strain behaviour, as seen in Figure 10. As with the monotonic simulation the accuracy increases with decreasing strain increments. However, at some point the increments become too small and produce a problem with stability in the model. As seen in Table 3, when the strain increments becomes $\Delta\varepsilon_1 = 10^{-7}$ the model becomes unstable. This makes it difficult to estimate the error of the different strain increments because convergence has not been established. The error measures have therefore been compared to the last stable increment size, which is $\Delta\varepsilon_1 = 0.5 \times 10^{-6}$. This means that the calculated error for the cyclic simulations must be considered with a high amount of uncertainty.

However, the instability problems that the model faces during cyclic loading indicates that there is a problem with the implementation of the integration scheme into the constitutive model. Instability problems does not make physical sense when reducing the increments, because a reduction of the increment size will entail a solution approaching the exact value.

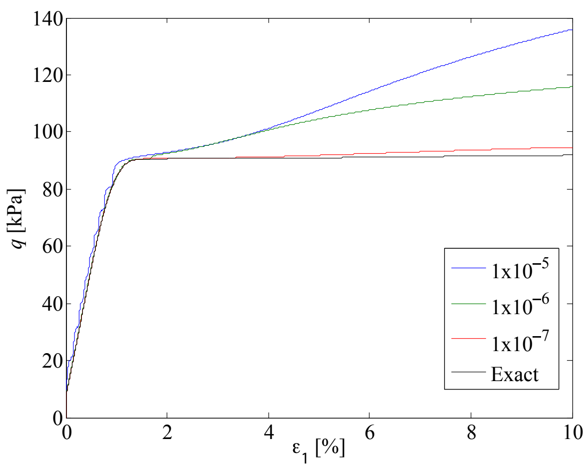

Figure 8: *Results of monotonic simulation with Modified Critical State Two-Surface model and the accuracy of different strain increments.*

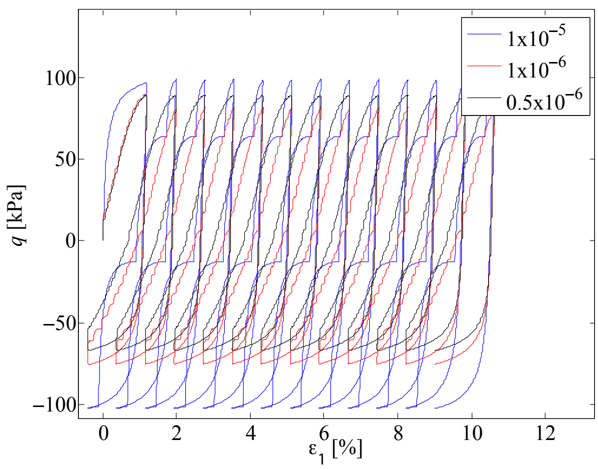

Figure 10: *Results of cyclic simulation and the accuracy of different strain increments.*

5 Conclusion

The Forward Euler integration scheme is implemented into the Modified Critical State Two-Surface model originally formulated by Manzari and Dafalias (1997) and modified by LeBlanc (2008). The objective was to investigate if a simple integration scheme could be implemented into an advanced constitutive model and still model correct stress-strain behaviour of a cohesionless soil. Monotonic and cyclic simulations are performed on a medium-dense sand in order to measure the accuracy of the integration scheme for different strain increments. It is found that with the Forward Euler method the step size will be inappropriately small ($\Delta\varepsilon_1 < 10^{-7}$) for monotonic loading. More importantly the model becomes unstable for cyclic loading, thereby inducing a large inaccuracy into the model. However, this is not believed to be a problem with the integration scheme itself, but the implementation of the constitutive model. Still, the conclusion is that a simple integration scheme, such as the Forward Euler method, can not be recommended for a model of this complexity.

References

Ibsen, 1998. Lars Bo Ibsen. *The Mechanism Controlling Static Liquefaction and Cyclic Strength of Sand.* Proc. Int. Workshop on Physics and Mechanics of Soil Liquefaction, A. A Balkema, Rotterdam, (27), pages 29–39, 1998.

Krabbenhøft, 2002. Kristian Krabbenhøft. *Basic Computational plasticity*, 2002.

Krenk, 1996. S. Krenk. *Family of Invariant Stress Surfaces.* Journal of Engineering Mechanics - Proceedings of the ASCE, Vol. 122(3), pages 201–208, 1996.

LeBlanc, 2008. Christian LeBlanc. *A modified critical state two-surface plasticity model for sand - theory and implementation.* ISSN: 1901-7278, DCE Technical Memorandum no. 8. Aalborg University, 2008.

Manzari and Dafalias, 1997. M.T. Manzari and Y.F. Dafalias. *Critical state two-surface plasticity model for sands.* Géotechnique, Vol. 47(2), pages 255–272, 1997.

Schofield and Wroth, 1968. A.N. Schofield and C.P. Wroth. *Critical State Soil Mechanics.* ISBN: 978-0641940484. McGraw-Hill, 1968.

Wroth and Houlsby, 1985. C.P. Wroth and M.F. Houlsby. *Soil mechanics: property characterisation and analysis procedures.* Proc. 11th International Conf. Soil Mech. Found. Engng. San Fransisco, pages 1–50, 1985.

Wroth, Randolph, Houlsby, and Fahey, 1979. C.P. Wroth, M.F. Randolph, G.T. Houlsby, and M. Fahey. *A review of the engineering properties of soils with particular reference to the shear modulus.* Tech. Report CUED/D-SOILS TR75. University of Cambridge, 1979.

Manual

Manual for Cyclic Triaxial Test

Manual for Cyclic Triaxial Test

Amir Shajarati
Kris Wessel Sørensen
Søren Kjær Nielsen
Lars Bo Ibsen

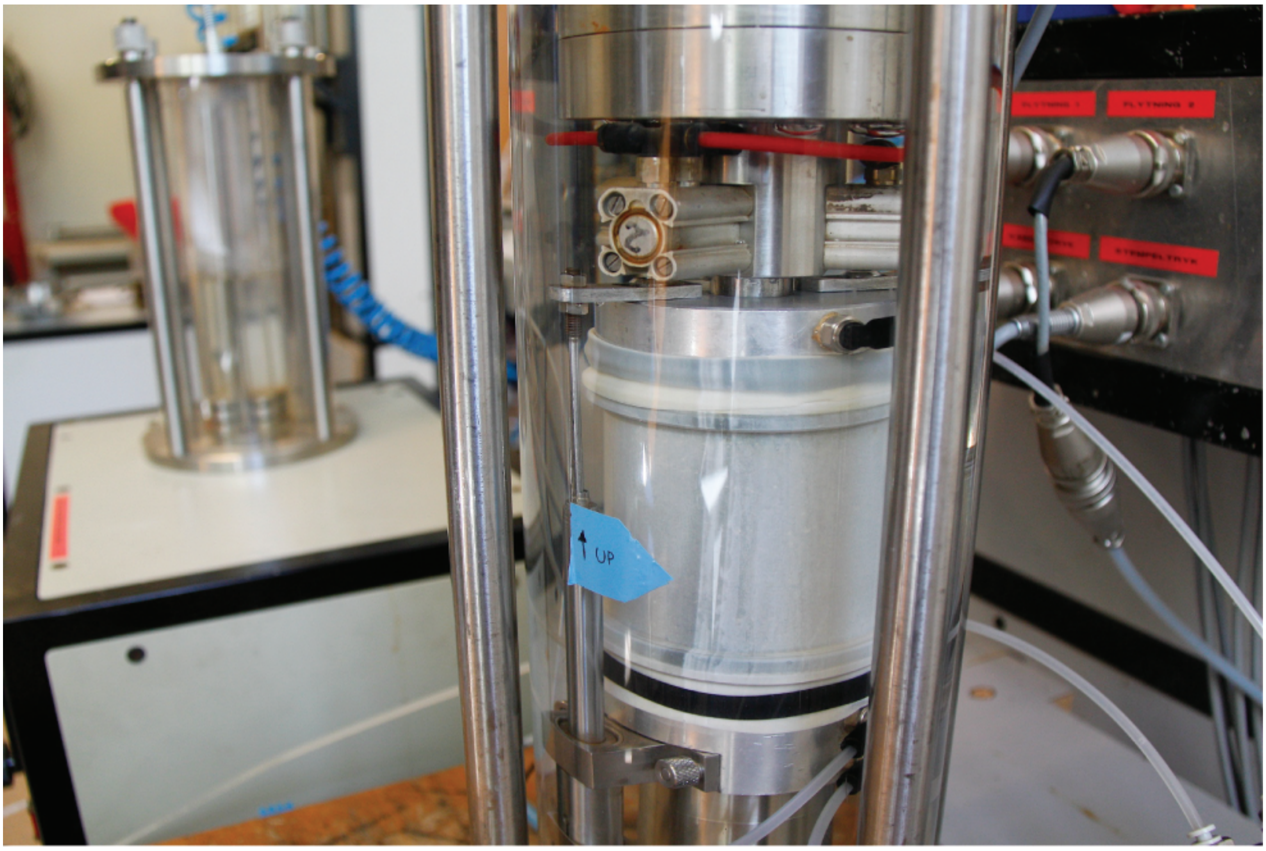

ISSN: 1901-726X
DCE Technical Report No. 114

AALBORG UNIVERSITY
Department of Civil Engineering

Aalborg University
Department of Civil Engineering
Geotechnical Engineering

DCE Technical Report No. 114

Manual for Cyclic Triaxial Test

by

Amir Shajarati
Kris Wessel Sørensen
Søren Kjær Nielsen
Lars Bo Ibsen

June 2012

Scientific Publications at the Department of Civil Engineering

Technical Reports are published for timely dissemination of research results and scientific work carried out at the Department of Civil Engineering (DCE) at Aalborg University. This medium allows publication of more detailed explanations and results than typically allowed in scientific journals.

Technical Memoranda are produced to enable the preliminary dissemination of scientific work by the personnel of the DCE where such release is deemed to be appropriate. Documents of this kind may be incomplete or temporary versions of papers—or part of continuing work. This should be kept in mind when references are given to publications of this kind.

Contract Reports are produced to report scientific work carried out under contract. Publications of this kind contain confidential matter and are reserved for the sponsors and the DCE. Therefore, Contract Reports are generally not available for public circulation.

Lecture Notes contain material produced by the lecturers at the DCE for educational purposes. This may be scientific notes, lecture books, example problems or manuals for laboratory work, or computer programs developed at the DCE.

Theses are monograms or collections of papers published to report the scientific work carried out at the DCE to obtain a degree as either PhD or Doctor of Technology. The thesis is publicly available after the defence of the degree.

Latest News is published to enable rapid communication of information about scientific work carried out at the DCE. This includes the status of research projects, developments in the laboratories, information about collaborative work and recent research results.

Published 2012 by
Aalborg University
Department of Civil Engineering
Sohngaardsholmsvej 57,
DK-9000 Aalborg, Denmark

Printed in Aalborg at Aalborg University

ISSN 1901-726X
DCE Technical Report No. 114

Contents

Part I

Manual

1 Introduction

This manual describes the different steps that is included in the procedure for conducting a cyclic triaxial test at the geotechnical Laboratory at Aalborg University. Furthermore it contains a chapter concerning some of the background theory for the static triaxial tests.

The cyclic/dynamic triaxial cell is overall constructed in the same way as the static triaxial cell at Aalborg University, but with the ability to apply any kind of load sequence to the test sample.

When conducting cyclic triaxial tests, it is recommended that the manual is followed **very** tediously since there are many steps and if they are done improperly or in the wrong order there is a risk of destroying the test sample or obtaining invalid results.

Cyclic Triaxial Test Set-up 2

In this chapter the test set-up and an overall description of how the system works will be described. In Pedersen and Ibsen [2009] a more detailed description of each component can be found.

2.1 Description

The cyclic triaxial apparatus consists of different elements, both electrical and mechanical. Figure 2.1 shows the set-up of the cyclic triaxial test. The *control board*, in Figure 2.1 is only used for sample preparation. It controls the vacuum and the saturation process needed in order to prepare the sample for testing. The purpose of the *backpressure system* is to apply a pressure inside the sample in order to get water out into all the voids and to dissolve any gas. When a CU triaxial test is performed the backpressure system assures that the sample has a constant volume and that no drainage in the sample is allowed. During a CD triaxial test the backpressure system measures the amount of dissipated water and hereby the volumetric changes, which is used when calculating the radial deformations. Furthermore, the backpressure system is used to obtain the desired in-situ effective stresses in the sample.
Notice in Figure 2.1 that the water level in the large outer tube of the backpressure system should be aligned to the middle of the sample height. This is to ensure that there is no geometrical pressure difference added to the backpressure.

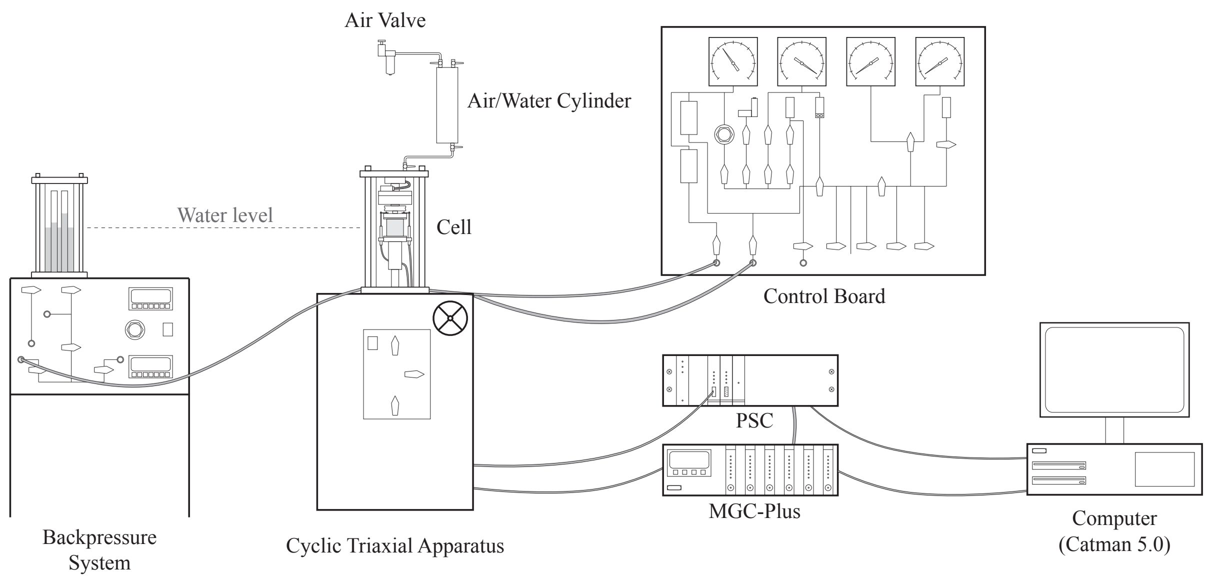

Figure 2.1: Cyclic triaxial test set-up.

The cell is enclosed with a plastic tube, which makes it possible to fill the cell with water. With water in the cell it is possible to increase the cell pressure and thereby the confining pressure on the sample. This is done with the *air valve* and the *air/water cylinder*, which is connected directly to the cell, see Figure 2.1. By opening the air valve, compressed air is let into the air/water cylinder and thereby increasing the pressure in the cell. The air/water cylinder also works as a spring that keeps the cell pressure constant when the piston is moving.

2.2 Cyclic Triaxial Cell

A close-up of the cyclic triaxial cell is shown in Figure 2.2. The cyclic triaxial cell consists of the test specimen and different measuring systems. The measuring systems consists of the *deformation transducers*, the *load cell*, the *pore pressure* and *cell pressure transducers*. The deformation transducers measures the axial deformation of the specimen. The load cell measures the load that the specimen is exposed to. The pore pressure transducer and the cell pressure transducer measures the pore pressure and cell pressure, respectively.

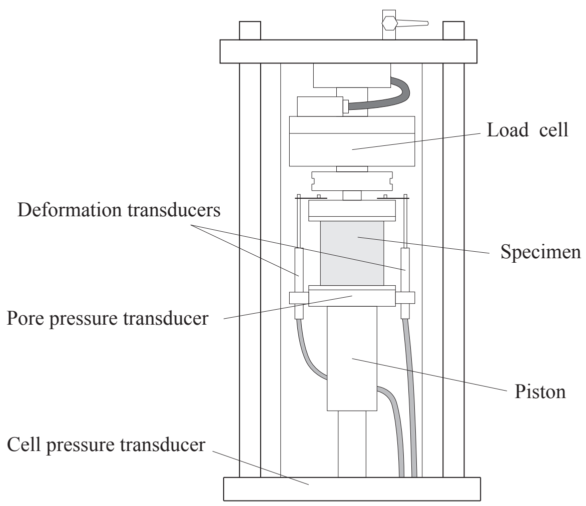

Figure 2.2: *Cyclic triaxial cell.*

When conducting a test a load file is sent from the computer to the *PSC-rack*. The load file consists of a string of numbers which indicate either a value in Newton or a value in millimetres, depending on if the test is conducted as force or deformation[1] controlled. In this way the loading can either be applied static or cyclic dependent on what kind of load path that needs to be simulated.

From the PSC a voltage signal is sent to the piston in the bottom of the cell which then applies a force to the sample. The force is measured in the load cell, which sends a signal to the *MGC-Plus*. From the MGC-Plus a feedback signal is sent to the PSC, and if the feedback signal does not correspond to the signal sent from the computer, adjustments are made automatically so the wanted load is applied.

The measured data is being collected by the MGC-Plus and logged in the computer. Both the MGC-Plus and the PSC are controlled from the computer by the program *Catman 5.0*.

[1]The deformation control does not work properly in the given set-up.

3 Preparing the sample

As mentioned before there are many steps to be executed when conducting a cyclic triaxial test. Overall there are two main points; sample preparation and the actual test execution. The different steps needed in order to prepare the sample for testing are described in the following chapter.

3.1 Boiling the water

Start boiling the water. This is done by filling up the large water container by opening the valves from "TILLØB" up to "VANDBEHANDLING" on the control board, see Figure 3.1. Afterwards vacuum is applied by turning on the vacuum pump on the left side column and opening the valves from "VACUUM PUMPE" up to "VANDBEHANDLING". **Remember to close the valves from "TILLØB" first.** Lastly, the blue button labelled "VANDBEHANDLING" on the left side column is pressed in order to spin the small rod in the bottom of the tube. The water will then start boiling.

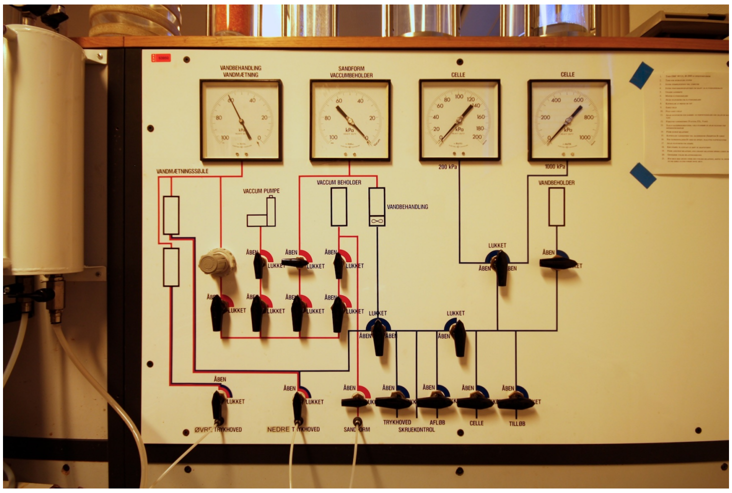

Figure 3.1: Control board for controlling vacuum and saturation of the sample.

3.2 Blowing the cables

All cables from the control board into the triaxial cell are blown with compressed air in order to remove any excess water. Otherwise it will let water into the sample, which foils the saturation process later on. The same operation should be performed on the small valve panel, shown in Figure 3.2, along with the two pressure heads. The compressor must **not** be used on the pressure heads as it applies too much pressure (8 bar). The pore pressure transducer has an upper limit of 7 bar, and may be destroyed when exposed to 8 bar.

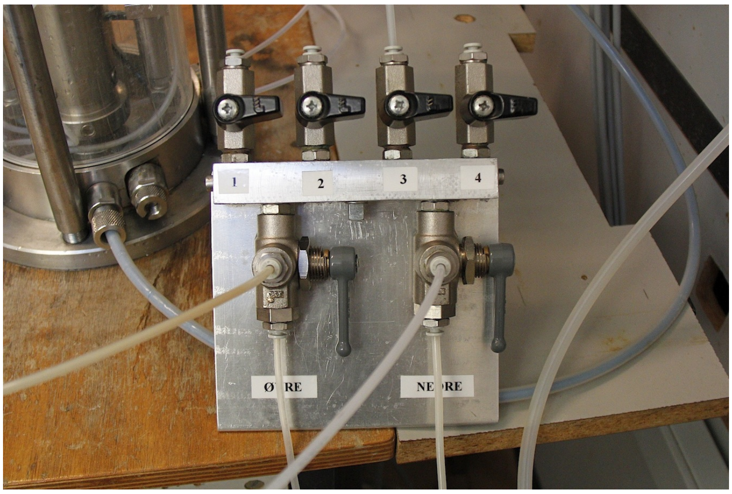

Figure 3.2: Valve panel.

3.3 Cable connection

The cable connections between the control board, the triaxial cell and the backpressure apparatus are as dictated in Table 3.1. It should be noted that the lower pressure head has two valves, the valve nearest the glass plate covering the base of the pressure head is defined as the upper valve. Moreover there is only one cable connection between the cell and the backpressure apparatus when a test is being performed.

Table 3.1: *Cable connections between the control board, the triaxial cell and the backpressure apparatus.*

Cable connection	Controlboard valve	Valve panel valve	Cell valve	Backpressure valve
1	"Øvre trykhoved"	Lower "ØVRE"		
2		Upper "ØVRE"	Upper pressure head	
3	"Nedre trykhoved"	Lower "NEDRE"		
4		Upper "NEDRE"	Lower pressure head lower valve	
5		3	Lower pressure head upper valve	
6		1		Backpressure

3.4 Preparing the pressure heads

Start by mounting the filterstones (Ø 7 mm) into the pressure heads and cut them flush with a knife. Hereafter, rub a decent amount of grease evenly out onto the pressure heads with a finger. Be sure to **not** get any grease on the filterstones. When the grease is evenly distributed over the pressure head it is "dabbed" with a finger in order to make it stick better. Next four rubber membranes are cut into circles with a hole in the center (Ø 8 mm) by using the plastic template. One rubber membrane is placed on top of the greased pressure head. Then a small steel rod is used to squeeze out air bobbles and distributing the grease evenly, see Figure 3.3. Start from the inside near the filterstone and always roll out towards the edge. Then a second coating of grease is applied on top of the first rubber membrane, and lastly the second rubber membrane is applied followed by squeezing out bubbles again. This procedure is done to ensure smooth end plates (see section 8.2) and has to be done on both pressure heads. A finished pressure head can be seen in Figure 3.4.

Figure 3.3: Steel rod squeezes out the air bobbles and distributes the grease evenly.

Figure 3.4: Rubber membrane rings mounted onto the pressure head with grease in between.

3.5 Rubber membrane

A cylindrical rubber membrane is wrapped over the lower pressure head with the two rubber bands mounted to make the fit tight, as shown in Figure 3.5. The membrane should be cut to a length of 15 cm. Next the sand form is mounted onto the lower pressure head. On top of the sand form the small brass ring is mounted and the rubber membrane is pulled over both the ring and the sand form, see Figure 3.6. It should be noted that the rubber membrane should not be stretched to much because this can cause defects in the membrane which foils the saturation process later on. When the rubber membrane is in place the sand form is connected to the control board in order to get vacuum on the sand form by opening the valve "SANDFORM". This ensures that the rubber membrane is smooth and fills out the sand form completely, as shown in Figure 3.7.

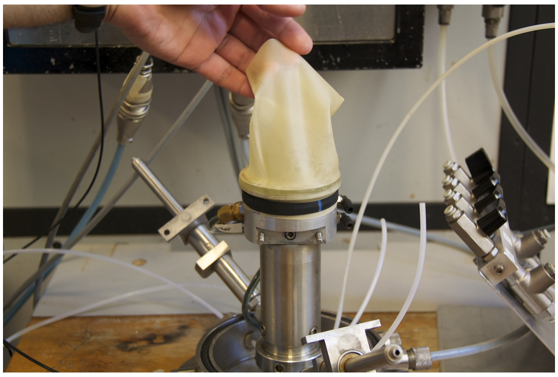

Figure 3.5: Membrane on lower pressure head with the two rubber membranes.

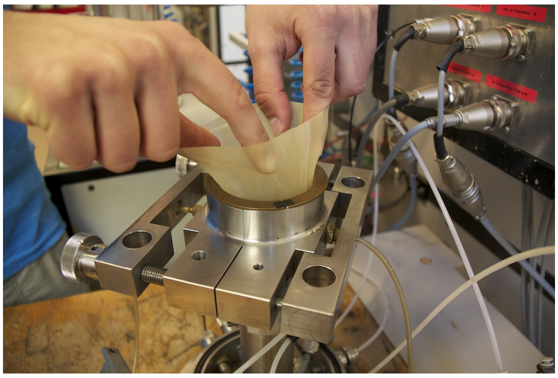

Figure 3.6: Wrapping the membrane over the sand form and brass ring.

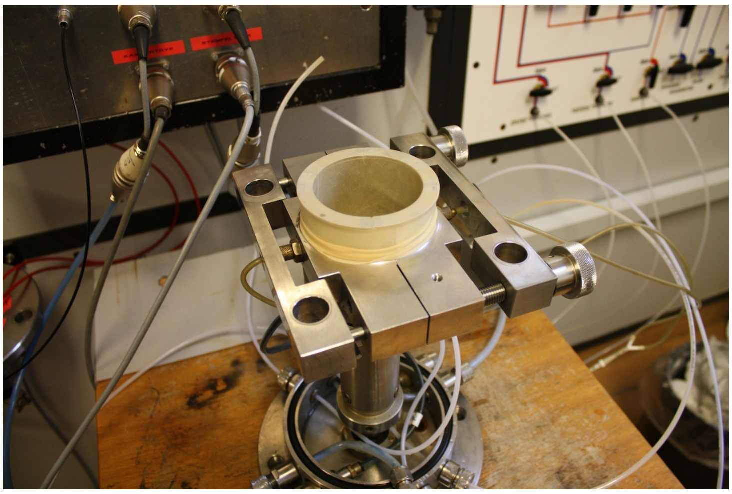

Figure 3.7: Sandform mounted onto the sample with the small brass ring and rubber membrane in place.

3.6 Hydraulic piston

Activate the hydraulic piston by turning the knob to "ON" and pressing the green button on the *circuit breaker panel*, see Figure 3.8. When the piston is turned on it will go all the way to the top position. Therefore MOOG needs to be started so the piston can be moved down (position -900).

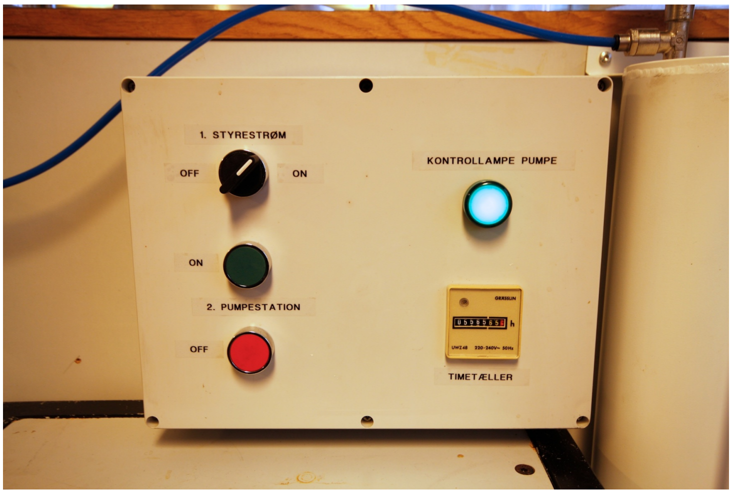

Figure 3.8: Circuit breaker for the hydraulic piston.

3.7 Undercompaction

To get the desired relative density, I_D, of the sample the *sample calculation sheet* is used, which applies the method of undercompaction, see Appendix. This makes it possible to calculate the weight of the individual sand layers needed to get the correct relative density. The sand layers are filled into the sand form one at a time and compacted using the *compaction rod* between each layer, see Figure 3.9. The height and number of blows needed depends on the wanted relative density. However, the number of blows should always be doubled, i.e. 1, 2, 4, 8 or 5, 10, 20, 40 etc.

3.8 Mounting the upper pressure head

When the sand has been compacted the upper pressure head is placed on top of the sand form. Remember to put the small rubber bands loosely onto the pressure head and attach the small tube to the pressure head **before** placing the pressure head on the sand form, see Figure 3.10. Afterwards, suction is applied to the upper pressure head. Then the rubber membrane is wrapped around the upper pressure head and sealed with the two rubber rings. This ensures that there is still vacuum on the specimen. The sand form can now be disassembled along with the small brass ring by closing the valve to "SANDFORM". Remove the sand form first, then remove the small brass ring. Figure 3.11 shows the sample when the sand form has been removed.

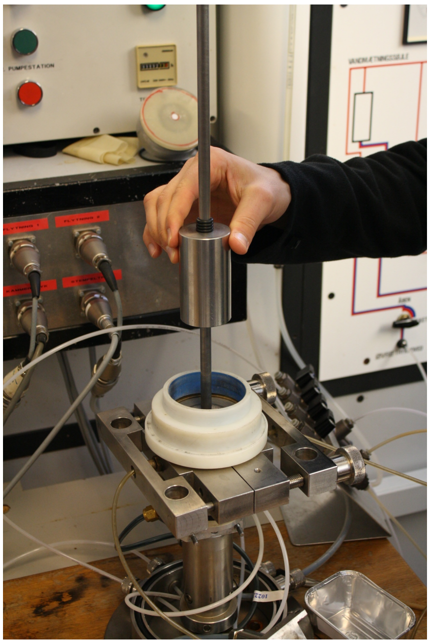

Figure 3.9: Compaction rod used to compact the sand down to the desired relative density, I_D.

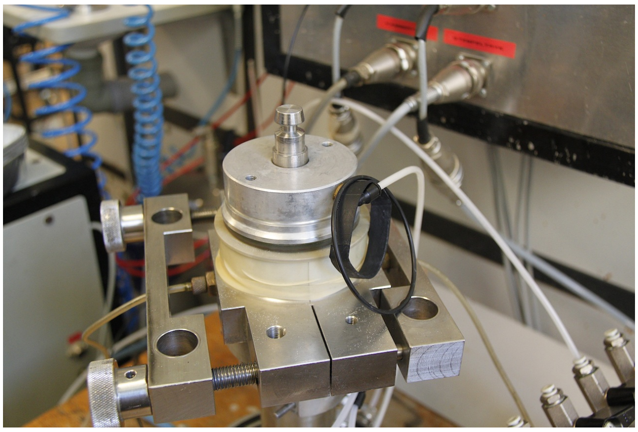

Figure 3.10: Upper pressure head with rubber bands loosely hanging on the side.

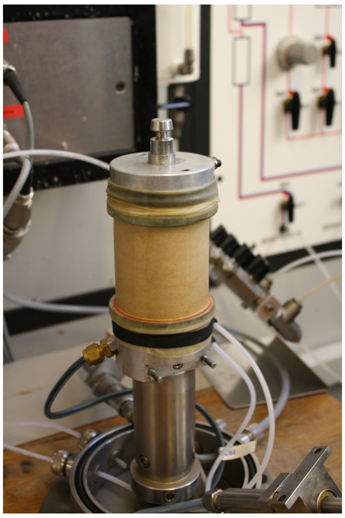

Figure 3.11: Sample when sand form has been removed.

3.9 Mounting the displacement transducers

The displacement transducer are mounted to the sides of the specimen via the small finger screws. On top of the upper pressure head the pins that go into the transducers are mounted via umbraco screws (the short srews) as seen in Figure 3.12. It is a good idea at this point to blow away sand on the table with compressed air. Hereafter the plastic tube is slided onto the entire specimen. Be sure to check that "UP" on the blue sticker is pointing up, see Figure 3.13.

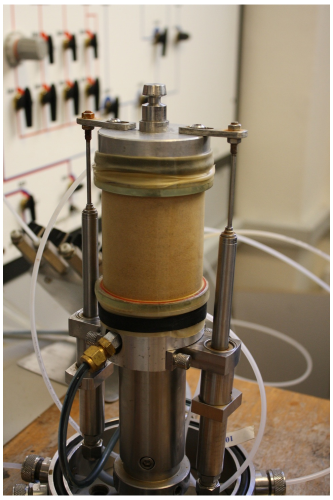

Figure 3.12: Sample with displacement transducers mounted.

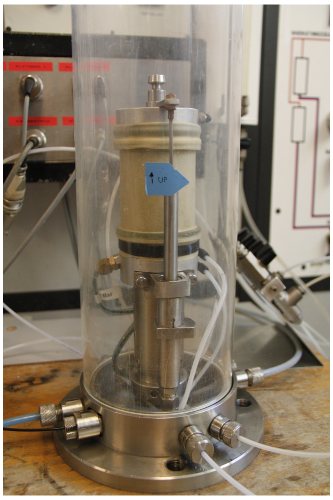

Figure 3.13: Plastic tube mounted with the blue sticker.

3.10 Mounting the load cell

With the piston in the bottom position the load cell is placed on top of the plastic tube. Be sure to align both the plastic tube and the metal ring properly at top and bottom. The locking mechanism in the load cell should be **open**, see Figure 3.14. The locking mechanism consists of three small steel rods that spring into place and holds the sample tight. The mechanism is set to open by opening the valve labelled "Åben" that is connected to the red tubes leading to the load cell. Then the valve below, labelled "Lukket" is closed. Lastly the small brass valve in front of "Lukket" is turned so that the air will escape. Figure 3.15 shows the correct position of the valves.

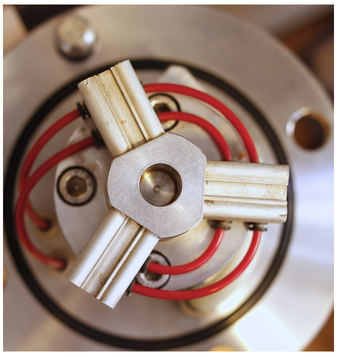

Figure 3.14: Locking mechanism in the load cell set to open.

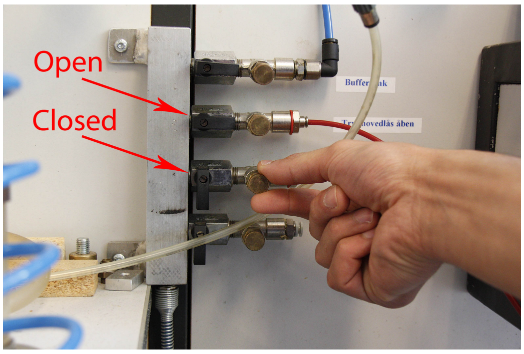

Figure 3.15: Valve position for keeping the locking mechanism open.

Then the steel rods are slided into position and tightened. Remember to "cross-tighten" the rods individually until you cannot even get a finger-nail underneath the rods in the bottom. The final sample is shown in Figure 3.16.

Figure 3.16: Final sample with load cell and plastic tube mounted.

4 Filling the cell with water

When the aforementioned have been conducted, the cell has to be filled with water. Before the filling starts it should be ensured that all cable connections leading to the cell in the bottom are closed and tightened (hard), see Figure 4.1. With over 500 kPa of pressure water will find a way out if they are not tightened hard.

Figure 4.1: Cable connections into the cell. Make sure to tighten them hard.

4.1 Letting water into the cell

Water is let into the cell by turning the valve ”CELLE” on the control board and the valve ”FYLDNING AF CELLE” on the triaxial table control board (see Figure 4.2) to ”ÅBEN”. Be sure to **close the vacuum** for "VAND-BEHANDLING" but still maintaining vacuum for the sample. Also, the black valve on top of the load cell has to be open so the air can get out. The black valve should later be connected to the pressure cylinder.
The cell should be filled half way up (up till the blue sticker) and a reading of the confining pressure should be noted down. This should be the new zero-value for the confining pressure. This is done because the pressure transducer is located in the bottom of the cell and therefore the value it reads is not the same pressure as the sample is subjected to at its higher position.

4.2 Connection of air/water cylinder

Continue filling the cell with water until a few water drops comes out of the black valve on top of the cell. Connect the lower right valve from the air/water cylinder with the black valve on top of the cell and open the lower right valve, see Figure 4.3. Continue the filling of water until the transparent measuring cable on the pressure cylinder is approximately half full. On the air/water cylinder the upper valve should be open during filling the cell with water

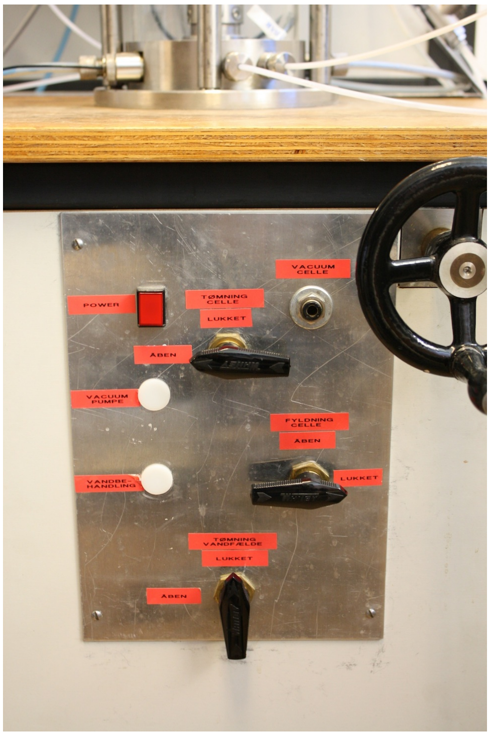

Figure 4.2: Triaxial table control board.

and closed when filling is completed.
The air in the air/water cylinder acts as a spring when the piston is moving, because during movement of the piston the volume of steel inside the cell changes and therefore the amount of water also has to change.

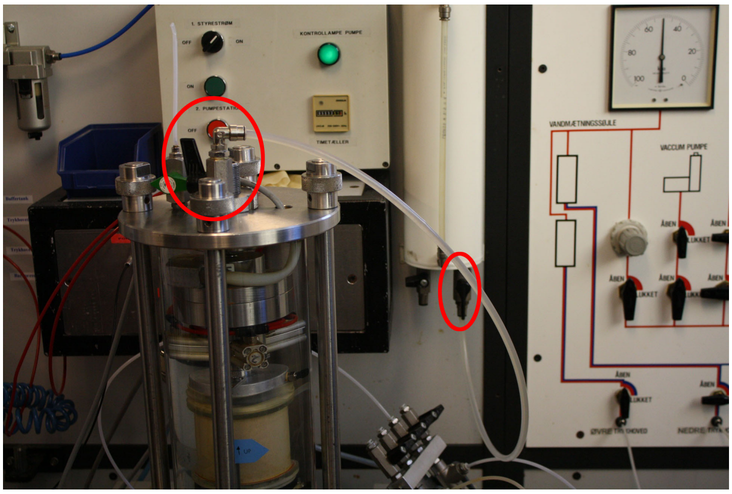

Figure 4.3: Connection between the pressure cylinder and cell marked with red circles.

4.3 Reducing vacuum

The next step is to reduce the vacuum inside the sample while increasing the cell pressure. This is done with an interval of 10 kPa. First negative pore pressure is increased 10 kPa (e.g. from -30 kPa to -20 kPa) and afterwards the cell pressure is increased by 10 kPa. The cell pressure is applied by turning the knob connected to the air/water cylinder. Before opening the black valve labelled "Buffertank" for the pressure cylinder placed to the left, it should be made sure, that the knob is loose so that a large cell pressure will not be added instantly, thereby destroying the sample, see Figure 4.4.

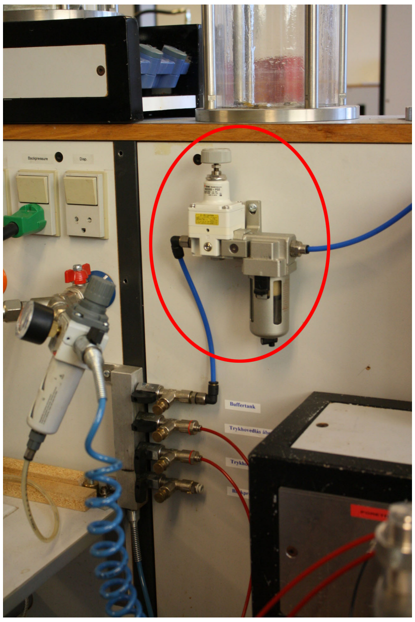

Figure 4.4: Valve for the buffertank along with the knob that adjusts the pressure.

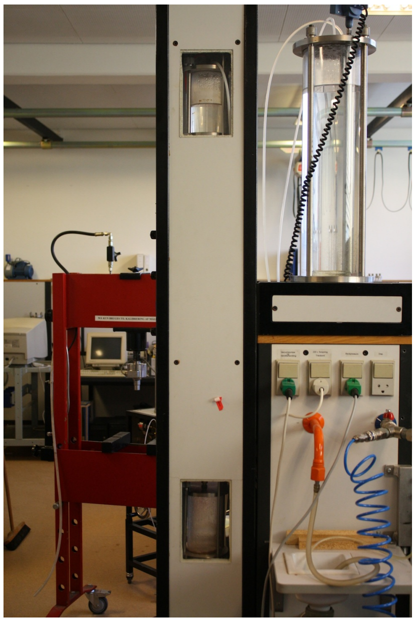

Figure 4.5: Small water containers used when saturating the sample.

4.4 Saturation column

It should be insured that the upper water container in the left column (saturation column) is filled with water which is used later on to saturate the sample. This container is filled with water from "VANDBEHANDLING". This is done by making vacuum in the upper water container while making sure that there is no vacuum in the "VANDBEHANDLING" container.
The lower water container in the left column should be emptied every time before conducting a test. Otherwise it will let unwanted water into the sample. The two water containers in the left column are shown in Figure 4.5.

5 Saturation of the sample

After the cell is filled with water, the test specimen has to be fully saturated. Before the sample is saturated with water it first needs to be saturated with carbon dioxide (CO_2) because this is easier dissolved than air. CO_2 is heavier than atmospheric air, and when let into the soil from the lower pressure head the atmospheric air will be driven out. CO_2 is let in via the lower pressure head through the sample and up into the upper pressure head, where it is lead out into a plastic bag. The pressure from the CO_2 tank should be low enough to still maintain a decent amount of effective stresses. Proceed with the saturation process until the plastic bag is filled with CO_2. Remember to also fill the valve panel with CO_2.

5.1 Saturation of the sample

Next the soil sample has to be saturated with water. This is done by letting water from the small water container (top in the left column) through the lower pressure head. The water has to pass through the sample and out through the upper pressure head over into the small water container (bottom of the left column). This process takes approximately 30 min. If there is no water left in the small water container in the top after the sample is saturated, it needs to be filled again for later use. This is done in the same way as before, by making vacuum and opening the valves to "VANDBEHANDLING".

5.2 Saturation of the valve panel

Now the valve panel needs to be fully saturated. This is done by making sure that the left grey valve is in the upward position while the right grey valve is in the downward position, as shown in Figure 5.1. Meanwhile all the black valves needs to be open. Now water can be let from the small water container in the top via the lower pressure head and out through the valve panel, thereby assuring that the entire valve panel is saturated.

5.3 Saturation of backpressure system

After the saturation of the valve panel is complete, it is time to saturate the tube connecting the valve panel with the backpressure system, see Figure 5.2. First close black valve numbers 2 and 4. Secondly, close the valve on the back of the backpressure system and disconnect the blue tube, as shown in Figure 5.3. Now water can be let through in the same way as before (via the small water container in the top) and over into the backpressure system. Be sure to set the valves up to "MÅLERØR" to "ÅBEN". The tube labeled 85 cm3 needs to be approximately half full.

Next, level the backpressure system with the sample. Make sure that the water-level in the largest cylinder (the surrounding cylinder) in the backpressure system is at the same height as the middle of the sample (blue sticker marks the spot). Afterwards the blue tube on the back is reconnected and the valve is opened again.

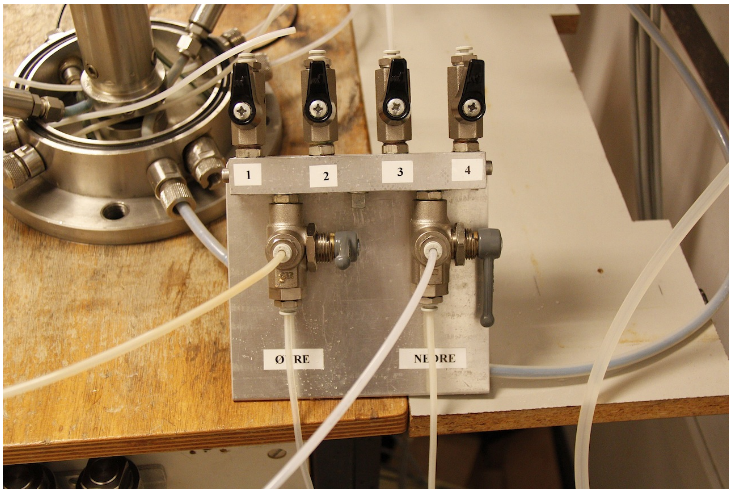

Figure 5.1: Position of grey valves on valve panel for saturating the valve panel.

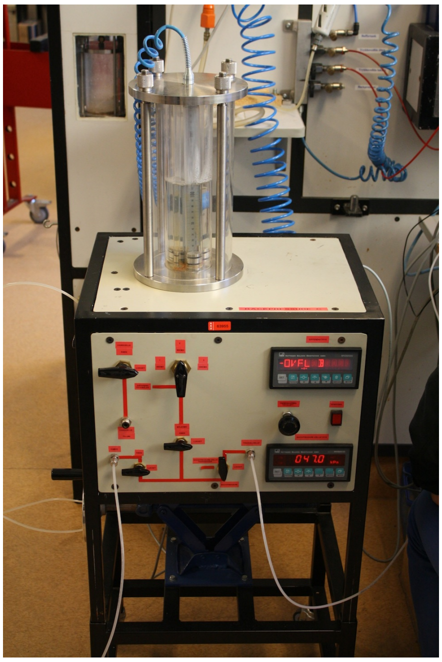

Figure 5.2: Backpressure apparatus.

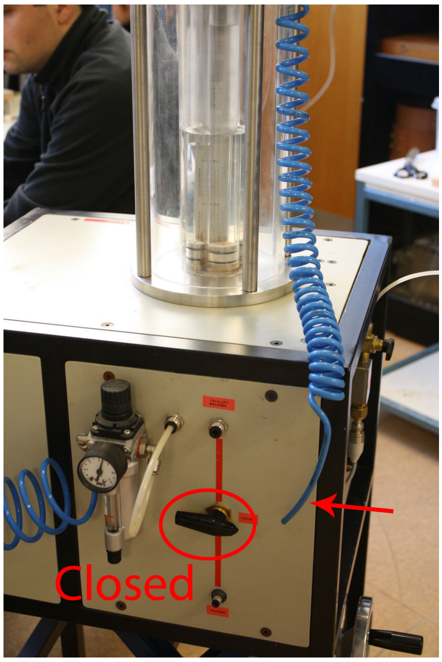

Figure 5.3: Blue tube on the back of the back pressure system.

5.4 Activation of backpressure system

When saturation of both the sample and the tubes to the backpressure system are complete, both grey valves on the valve panel are turned upwards so the backpressure system is activated and the control board is deactivated. The position of the valves can be seen in Figure 5.4.

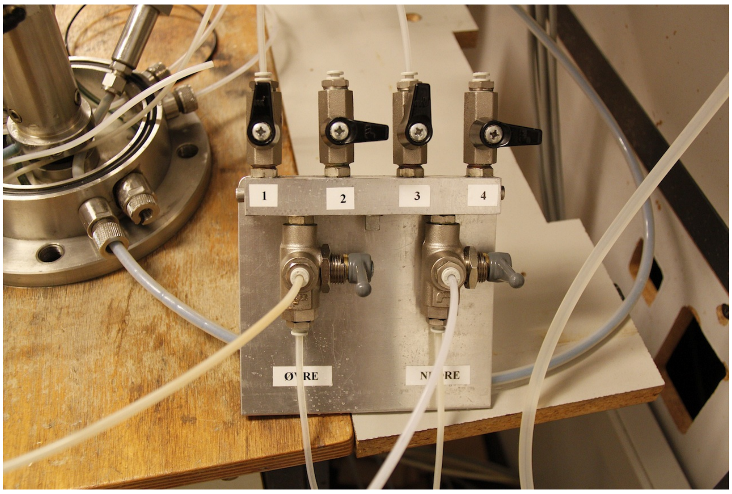

Figure 5.4: Valve panel with the backpressure system activated.

The system is now ready for the backpressure to be applied. On the front of the backpressure system the lower right valve is turned to "BACKPRESSURE". The lower left valve should be set to "LUKKET" and the lower middle valve should be set to "ÅBEN". The next phase is to apply the same amount of cell pressure as backpressure. Firstly the backpressure is increased by e.g. 10 kPa, and at the same time the cell pressure is increased by the same amount. In order to apply the backpressure the lower left valve is set to "ÅBEN" in a few seconds so the pressure can stabilise, and then turned to "LUKKET" again.

6 Skempton's constant B

The cyclic triaxial apparatus is used for investigating the effects that cyclic loading will have on a soil sample. These effects will primarily have an impact on pore pressure. It is therefore important that all test samples that are used in the cyclic triaxial apparatus are completely saturated. The criterion for saturation of the test is given by the Skempton's constant, B, which is 1 for a fully saturated specimen. A completely saturated sample is difficult to obtain in the cyclic triaxial apparatus. Therefore a lower boundary is established which is dependent on the relative density, I_D, of the sample.

When testing Skempton's constant B a reading of the cell pressure and the pore pressure is made. Next the cell pressure is raised by 10 kPa and new readings are made. From this the Skempton's constant B is calculated from (6.1)

$$B = \frac{\Delta u}{\Delta \sigma_3} \tag{6.1}$$

If the criterion is not fulfilled then both the backpressure and cell pressure is raised e.g. 100 kPa so the effective stresses are still kept constant. Then the procedure is repeated until Skempton's constant B satisfies the lower boundary value for a given index density.

When a specimen is 100 % saturated and the cell pressure, σ_3, is increased in an undrained test, the pore pressure, u, will theoretically increase exactly the same amount. In practice a saturation of 100 % is not possible and therefore the tests have to be conducted on specimens with a lower saturation. For soils with a saturation lower than 100 % the value of Skemptons B is highly dependent on the stiffness of the soil skeleton.
When conducting triaxial tests on dense sand this is important to consider because a fully saturated sample will only give relative small values of Skemptons B. In Holtz et al. [2011] an example of a very dense sand is given, which is shown in Table 6.1.

Soil Type	S = 100 %	S = 99 %
Soft, normally consolidated clays	0.9998	0.986
Compacted silts and clays; lightly overconsolidated clays	0.9988	0.930
Overconsolidated stiff clays; sands at most densities	0.9877	0.51
Very dense sands	0.9130	0.10

Table 6.1: *Skemptons B as a function of degree of saturation, S. Holtz et al. [2011]*

In order to take this into account when preparing samples, a minimum value of B must be calculated for each soil, i.e. the relative density and grain size distribution. This can be done from equation (6.2), which take into account the saturation and the relative stiffness of the soil compared to water.

$$B(u) = \frac{1}{1 + \frac{n\,S\,K_s}{K_w} + \frac{n\,K_s}{u + p_{atm}}(1-S)} \tag{6.2}$$

where

n	Porosity [-]
S	Degree of saturation [-]
K_s	Bulk Modulus of soil sketelon [Pa]
K_w	Bulk Modulus of water [Pa]
u	Pore pressure [Pa]
p_{atm}	Atmospheric pressure [Pa]

From a consolidation test the Bulk Modulus of the soil skeleton, K_s, is calculated to approximately 108 MPa. Note that this is for the sand deposit from Frederikshavn. If another sand is being used then new consolidation tests has to be conducted in order to calculate the correct bulk modulus. An overview of the used parameters can be seen in Table 6.2.

Parameter	Symbol	Value	Unit
Porosity	n	0.42	-
Degree of saturation	S	0.9-1.0	-
Bulk Modulus of soil sketelon	K_s	$108 \cdot 10^6$	Pa
Bulk Modulus of water	K_w	$2000 \cdot 10^6$	Pa
Atmospheric pressure	p_{atm}	101325	Pa

Table 6.2: *Parameters used in calculating the necessary value of Skemptons B to gain a given degree of saturation.*

A degree of saturation of 99 % will be considered as sufficient, and the dependency of Skemptons B as a function of pore pressure is given in Figure 6.1.

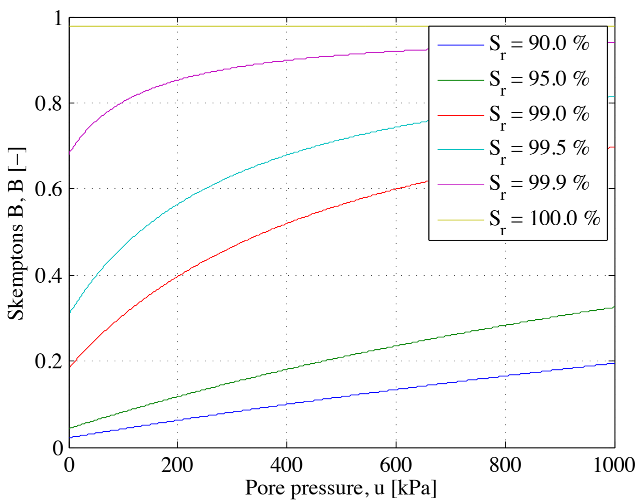

Figure 6.1: *Skemptons B as a function of pore pressure.*

7 Conducting a test

When the cell pressure and backpressure is high enough to fulfil the lower value of Skempton's B, the piston should be force controlled up into the right position in the load cell in order to lock the load cell onto the sample. To do this open MOOG on the computer. Write "*upar1*" and press enter. Press F2 and write "*dyntriax.log*" and press enter. When it is done loading press shift+F1 and shortly after press F2. This should bring up the *Engineering User Interface* as seen in Figure 7.1.

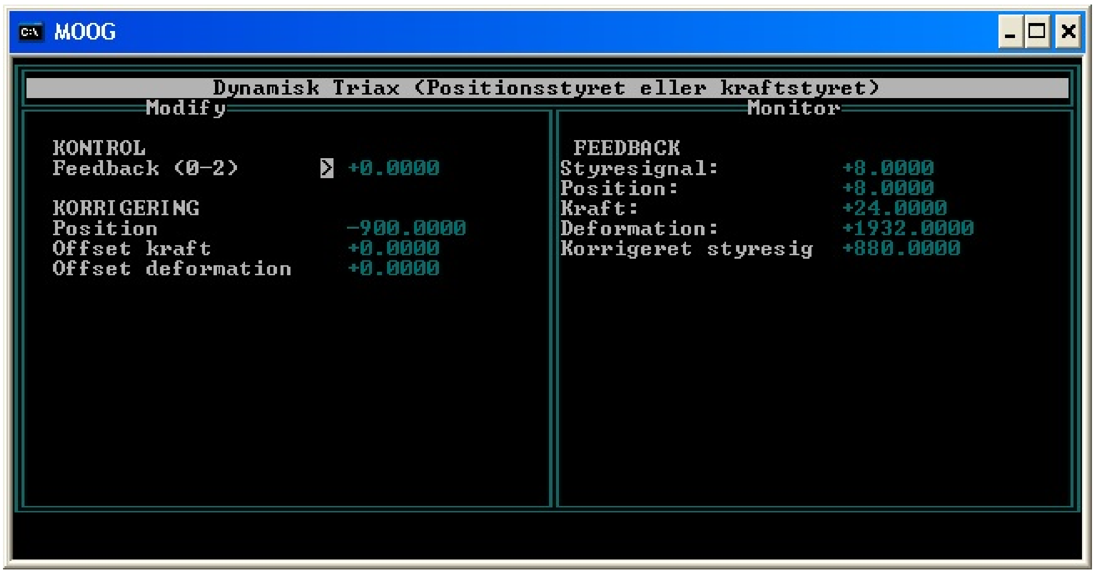

Figure 7.1: Engineering User Interface. This program controls the piston.

At the Engineering User Interface screen "KONTROL" should be set to "1". This makes the piston force controlled. Under "KORRIGERING" the value of "Offset kraft" (Offset force) is changed in order to get the piston to move up to the correct position. To find the right value of offset force for the piston to start moving takes some practice, but do note that a negative value will make the piston go up and a positive value will make it go down.

With the piston in the right position the load cell needs to be locked to the sample. This is done by closing the valve labelled "Åben" that is connected to the red tubes leading to the load cell. Then the valve below, labelled "Lukket" is opened. Lastly the small brass valve in front of "Åben" is turned so that the air will escape and then it's closed again (see Figure 7.3).

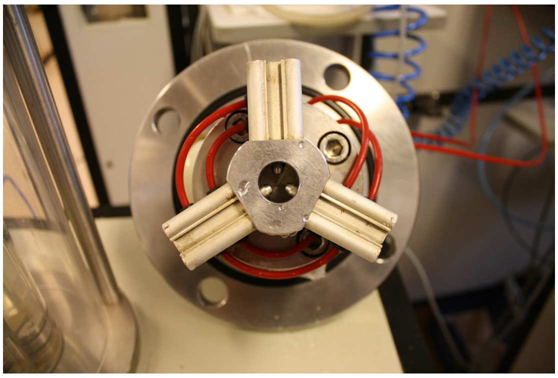

Figure 7.2: The locking mechanism consists of three steel rods that spring into place.

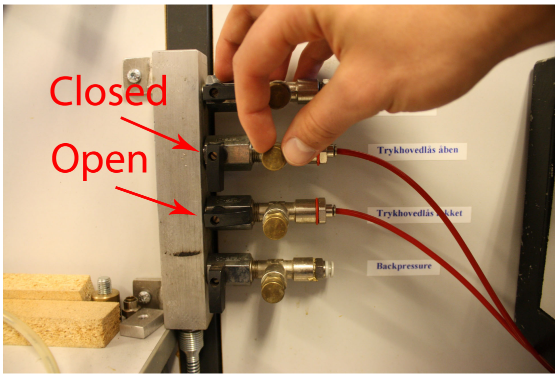

Figure 7.3: Valve position for locking the load cell.

When the sample has been locked into place, MOOG needs to be closed down. This is done by pressing escape, then type "q", press enter, lastly type "n" and press enter.

7.1 Uploading the load file

In order to apply the desired load to the sample, an input file (.inp) is created by using the matlab script *CyclicLoad-Generator.m* from Pedersen and Ibsen [2009]. When the file is created it needs to be uploaded to the PSC-rack. This is done by opening the *Online page* found on the desktop. A screenshot can be seen in Figure 7.4.

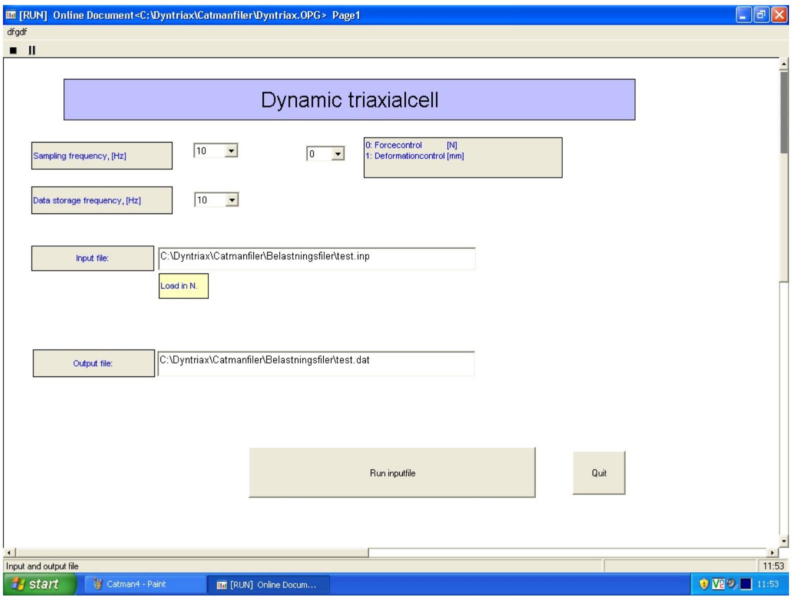

Figure 7.4: Online page where the load file is uploaded to the PSC-rack.

From the online page it is possible to select the desired input file, and where to place the output file (.dat). If deformation-controlled is selected[1] the data from the input file should be in *mm*, and if force controlled is selected

[1] Deformation control does not work properly at present time

it should be in *N*. Furthermore, it is possible to select the sampling frequency[2] and the data storage frequency. When everything is set-up, press "Run inputfile". This will bring up the second online page, shown in Figure 7.5.

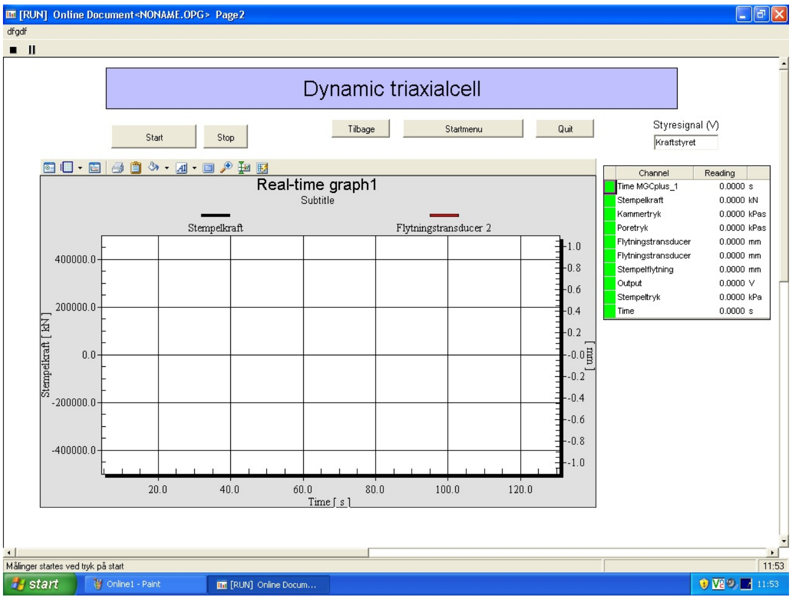

Figure 7.5: Online page where the data storage can be monitored.

The test will not start yet, but the input file is being uploaded to the PSC-rack. This can take some time depending on the size of the input file. Figure 7.6 shows how long it takes for a certain file size to upload. After the file is finished uploading the test is started by pressing "Start".

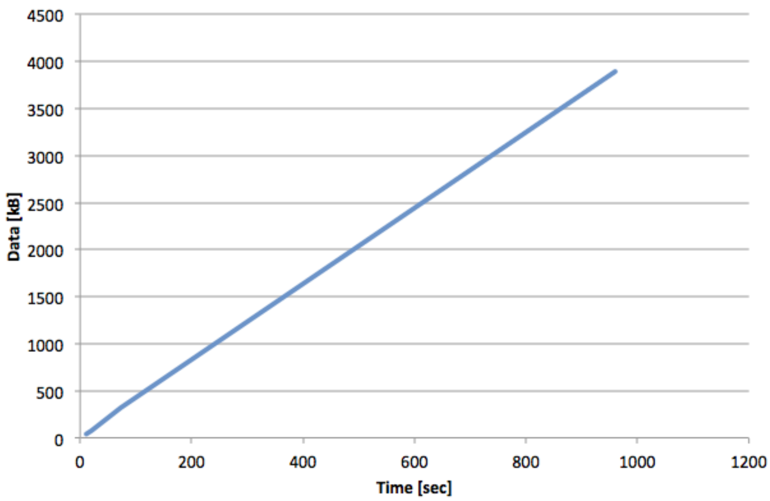

Figure 7.6: Time it takes to load an input file into the PSC-rack.

[2]50 Hz and 25 Hz seems to be too high. It is therefore recommended not to go above 10 Hz.

Part
II
Theory

8 Theory

When conducting triaxial tests it is necessary to construct different types of diagrams in order characterise the soil. The following chapters treats basic triaxial test theory and different aspects regarding the analysis of triaxial test data.

8.1 Output from Triaxial apparatus

The output data obtained when performing a cyclic triaxial test (cTxT) at Aalborg University is described in Chapter 2, and an overview is given in Table 8.1.

Table 8.1: *Output data from cyclic triaxial test apparatus.*

Measurement		Unit
Piston force	F_{pist}	[kN]
Confining pressure	σ_{conf}	[kPa]
Pore pressure	u	[kPa]
Axial def. transducer 1	d_1	[mm]
Axial def. transducer 2	d_2	[mm]
Piston position	d_3	[mm]
Differential pressure	ζ	[g]
Elapsed time	t	[s]

From the output data, stresses and strains are calculated in order to construct the necessary geotechnical diagrams, which are applied when analysing soil behaviour in order to characterise soil parameters. The equations in Table 8.2 are used in order to calculate stresses and strains.

Table 8.2: *Equations used for calculating stresses and strains.*

Deformations	Strains	Stresses
$\Delta H = \frac{(d_1+d_2)}{2}$	$\varepsilon_1 = \frac{\Delta H}{H_0}$	$\sigma_3 = \sigma_{conf}$
$\Delta V = \frac{\zeta}{\rho_w}$	$\varepsilon_2 = \frac{\Delta D}{D_0}$	$\sigma_1 = \frac{F_{pist}}{A} + \sigma_3$
$\Delta D = \sqrt{\frac{\Delta V+V_0}{\Delta H+H_0}\frac{4}{\pi}} - D_0$	$\varepsilon_3 = \varepsilon_2$	$\sigma_3^{'} = \sigma_{conf} - u$
$A = \frac{V_0-\Delta V}{H_0-\Delta H}$	$\gamma = \varepsilon_1 - \varepsilon_3$	$\sigma_1^{'} = \frac{F_{pist}}{A} - u + \sigma_3^{'}$
	$\varepsilon_v = \frac{\Delta V}{V_0}$	$p^{'} = \frac{\sigma_1^{'}+2\cdot\sigma_2^{'}}{3}$
		$q = \sigma_1 - \sigma_3$

8.2 Homogeneous and uniform conditions

A prerequisite for the above equations to be applicable is homogeneous and uniform stress and strain conditions. Ibsen and Lade [1998] proved that for a sample with a height/diameter (H/D) ratio larger than one failure will occur in a localised narrow rupture zone (shear band) where two solid bodies will slide with respect to one another along a failure line, see illustration (a) in Figure 8.1. If this is the case shear deformations and volume changes will take place in the rupture zone and not uniformly throughout the entire test specimen. However, the height of this localized failure zone is unknown and inconsistent along the shear band. Even though, strains and stresses are calculated from the full specimen height giving rise to misleading soil behaviour and a shortening of the stress-strain curve, which may only be correct at the very beginning of test, see Figure 8.2.

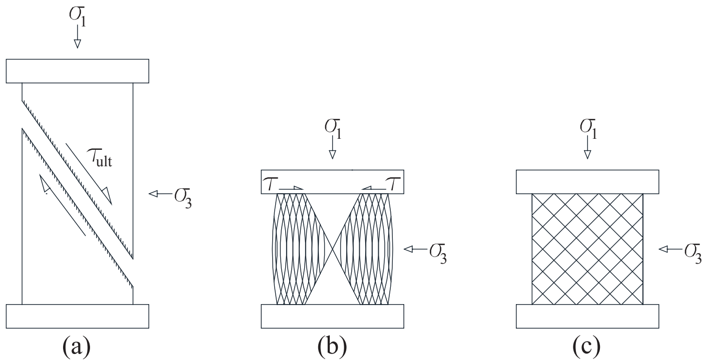

Figure 8.1: *Failure mechanism for triaxial specimen. (a) H=2D with a shear band. (b) H=D with rough end plates causing inhomogeneous conditions because of shear forces at end plates. (c) H=D with smooth end plates which entails uniform conditions.*

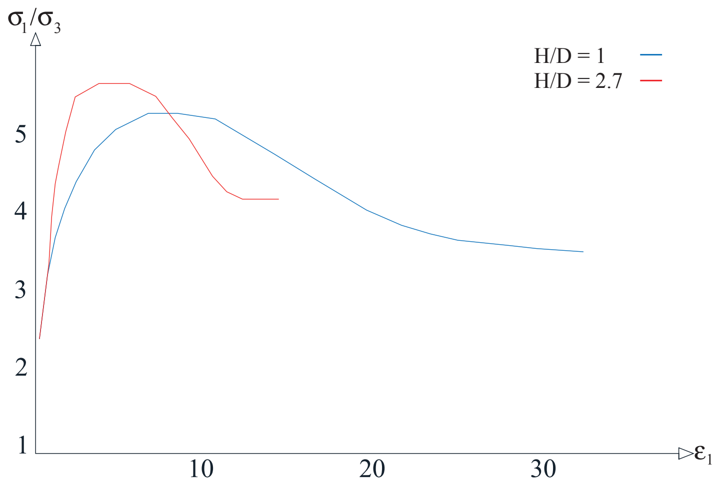

Figure 8.2: *Axial strain as a function of longitudinal and transversal stress ratio for Santa Monica Beach sand with* $D_R = 90\%$*. Red graph shows the path of a specimen with H/D=2.7 and blue graph is for H/D=1 [Ibsen and Lade, 1998].*

According to Ibsen and Lade [1998], when undrained triaxial tests are conducted on specimens with a H/D ratio larger than one, both compaction and dilation occurs at the same time throughout the shear band. This results in zero volumetric strain since water will flow from contracting areas to zones that dilate. Therefore the test is not truly undrained although the overall volumetric strains are zero.
Homogeneous an uniform stress and strain conditions are obtained if the test specimen have a H/D ratio equal to one with smooth end plates, see illustration (c) in Figure 8.1. If the end plates are rough shear forces will develop at the pressure heads causing a drum shaped specimen where strain and stresses are no longer homogeneous, see illustration (b) in Figure 8.1.

8.3 Data analysis

When the stresses and strains are calculated from the measured data, different diagrams are constructed in order to characterise soil behaviour and soil parameters. The response and parameters of the soil is different depending on if it is a drained or undrained triaxial test. The different diagrams are listed in Table 8.3.

Table 8.3: *Necessary diagrams for the analysis of triaxial test.*

Diagram		Drainage state
Deviatoric stress as a function of effective mean stresses	$p' - q$	Drained/undrained
Deviatoric stress as a function of axial strain	$\varepsilon_1 - q$	Drained/undrained
Volumetric strain as a function of axial strain	$\varepsilon_1 - \varepsilon_v$	Drained
pore pressure as a function of axial strain	$\varepsilon_1 - \Delta u$	Undrained
Shear stress as a function of effective stresses	$\sigma' - \tau$	Drained/undrained

8.3.1 Drained vs. Undrained

When conducting a drained triaxial test the soil behaviour can be characterised by plotting volumetric strain, ε_v, as a function of axial strain, ε_1. If it is a loose sample the test specimen will compact and positive volumetric strains will develop. If the sample is dense it will initially compact and then shift to dilation, which leads to expansion of the specimen and negative volumetric strain will develop, see illustration (a) in Figure 8.3.
When performing an undrained triaxial test the soil behaviour can be characterised by plotting change in pore pressure, Δu, as a function of axial strain, ε_1. This is due to the fact that when conducting an undrained test the volumetric strains are zero and therefore the overburden pressure is carried by the pore water. This means that positive change in pore pressure indicates compactive behaviour and negative pore pressure change indicates dilative behaviour, see illustration (b) in Figure 8.3.

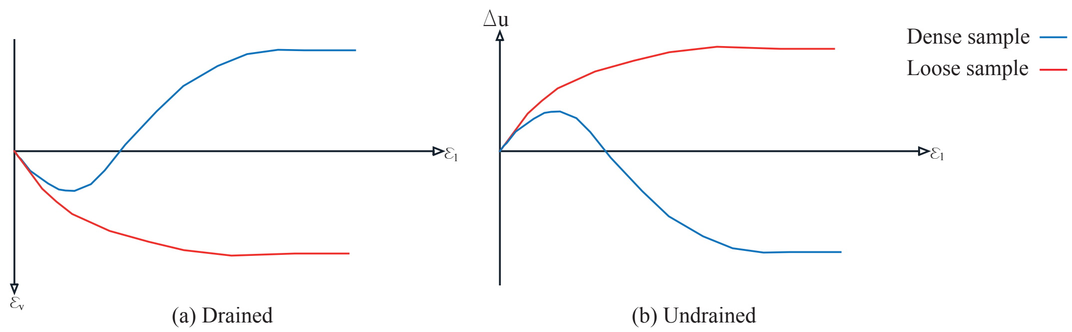

Figure 8.3: *(a) Volumetric strain as a function of axial strain. (b) Pore pressure as a function of axial strain.*

8.3.2 Deviatoric Stress

The same behaviour characteristics can be established by plotting deviatoric stress, q, as a function of the axial strain, ε_1. When a dense specimen is sheared the deviatoric stress reaches a maximum value after which the curve softens and goes towards a constant ultimate value (critical state), see Figure 8.4. When a loose specimen is sheared the deviatoric stress increases with no distinct peak towards an ultimate value, see Figure 8.4. The deviatoric stress for a loose specimen will have approximately the same ultimate value as the dense specimen.[Holtz et al., 2011]

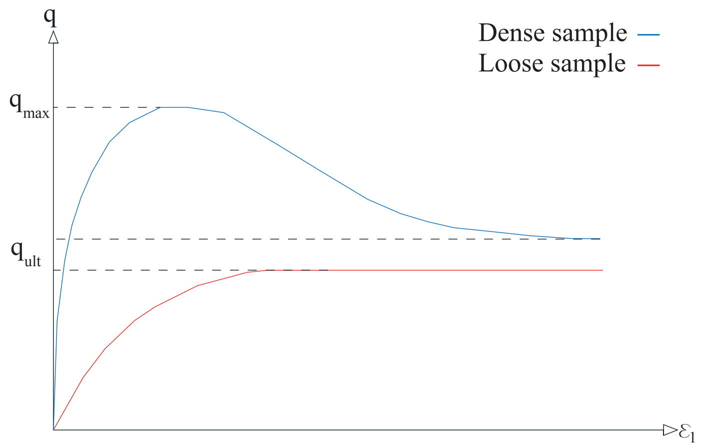

Figure 8.4: *Deviatoric stress as a function of axial strain.*

8.3.3 Void ratio

When a sample is sheared the void ratio, e, evolves in such a manner that it will move towards a critical void ratio, e_{crit}, see Figure 8.5. When a soil has reached the critical void ratio the volumetric strains and the deviatoric stress will be constant for continuous longitudinal and transversal strains. At this critical state a rearranging of the soil particles is possible but the relative density will remain constant hence the constant volume. The value of the critical void ratio depends on the isotropic stress level, particle shape and grain size distribution.
The critical void ratio for the loose and dense sample are not coinciding in Figure 8.5. In theory the value of the void ratio at failure should be the same for the loose and dense specimen but due to the absence of precise measurements of ultimate void ratio as well as non uniform stress and strain distribution a small deviation will be observed. Similarly the ultimate value at critical state of the deviatoric stress should be the same for the two tests.

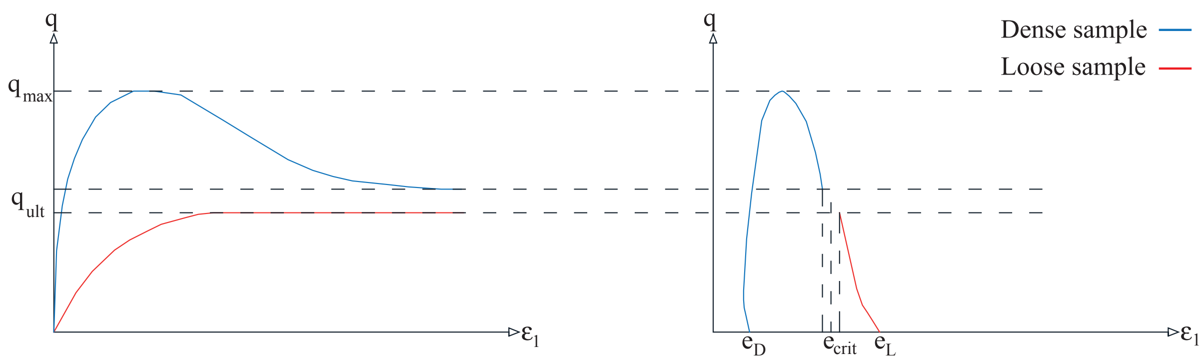

Figure 8.5: *Triaxial test on loose and dense specimens of a typical sand. The blue graph indicates the path of the dense sample whereas the red indicates the loose sample.*

8.3.4 Mohr's Circle Diagram

Once the maximum deviatoric stress value is obtained for different confining pressures, e.g. by a $\varepsilon_1 - q$ or $e - q$ diagram, σ_{conf}, Mohr's circle diagram can be constructed. Hereby the the angle of internal friction, φ, can be determined and thereby the ultimate shear strength of a given soil, see illustration (a) in Figure 8.6. The failure envelope in Figure 8.6 has its origion in origo because the sand is cohesionless. The angle of internal friction is determined by equation (8.1), where the numerator is the radius of a circle and the denominator is the center position of a circle.
If a dense specimen is sheared, dilative behaviour can be observed except at high confining pressures because crushing of the particles takes place. This will entail that Mohr's failure envelope is no longer linear but curved instead, see illustration (b) in Figure 8.6.

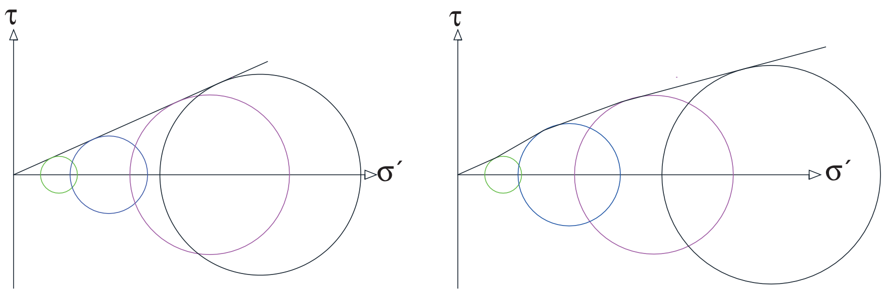

(a) Loose (b) Dense

Figure 8.6: Illustration of Mohr's circle diagram. Applied in order to determine the angle of internal friction.

$$sin(\varphi) = \frac{1/2\left(\sigma'_{1f} - \sigma'_{3f}\right)}{1/2\left(\sigma'_{1f} + \sigma'_{3f}\right) + c\ cot(\varphi)} = \frac{\left(\sigma'_{1f} - \sigma'_{3f}\right)}{\left(\sigma'_{1f} + \sigma'_{3f}\right)} \tag{8.1}$$

The amount of dilative behaviour is determined by the dilation angle, ν, which is defined as the slope of the gradient in a $\varepsilon_1 - \varepsilon_v$ diagram, see Figure 8.7.

Progression of the circles in Mohr's circle diagram in the undrained and drained case can be seen in Figure 8.8. The reason for the progression in different directions is caused by the change in stresses due to excess pore pressure. In the undrained case the overburden pressure is carried entirely by the excess pore pressure as listed in Table 8.4. From the tabular it is seen that the effective axial stress is constant during an undrained test and that the effective transversal stress is constant when performing a drained test.
It should be noted that in a laboratory test it is difficult to achieve a 100 % porepressure response, this is due to the fact that it is hard to obatin a fully saturated sample. In consequence of this the effective axial stress in the undrained case will not be completely constant.

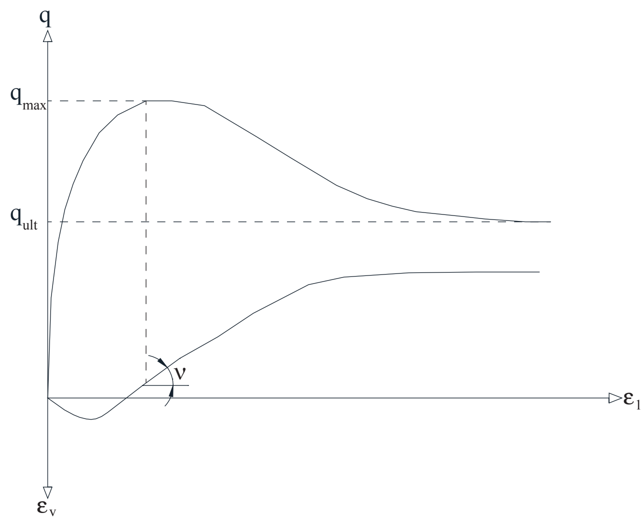

Figure 8.7: *Illustration of dilation angle,* ν.

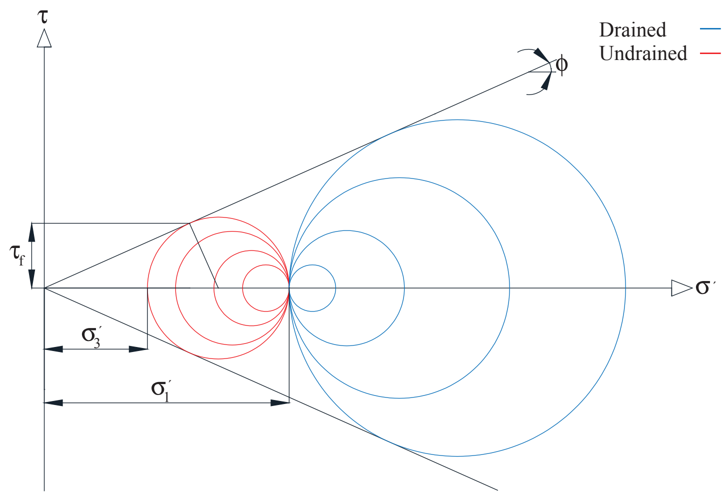

Figure 8.8: *Circle development in Mohr's circle diagram. Circles evolving to the left are showing stress conditions in a undrained triaxial test and circle evolving to the right is the drained case. It should be noted that the major and minor principle stress is different for the drained case*

Table 8.4: *Stresses during drained and undrained triaxial test.*

Undrained triaxial test	Drained triaxial test
$\sigma_3 = \sigma_{conf}$	$\sigma_3 = \sigma_{conf}$
$\sigma_3' = \sigma_{conf} - u$	$\sigma_3' = \sigma_3$
$\sigma_1 = \sigma_3 + p$	$\sigma_1 = \sigma_3 + p$
$\sigma_1' = \sigma_3 + p - u = \sigma_3'$	$\sigma_1' = \sigma_1$

8.3.5 *p* - *q* Diagram

It is impractical to use Mohr's circles in a σ - τ diagram when analysing soil behaviour during cyclic triaxial testing. This is due to the fact that it contains many informations since changes in stress conditions will appear as different circles changing both in size and position. Therefore it is more convenient to picture stress conditions as deviatoric stress, q, as function of effective mean stresses, p', see Figure 8.9.
When the coefficient of lateral earth pressure, K, is less than one it corresponds to a condition where the vertical stresses are larger than the lateral (axial compression) and vice versa. The failure envelope in this diagram is indicated by the coefficient of lateral earth pressure at failure, K_f. The slope of this line, ψ in relation to Mohr's failure envelope is established through (8.2).

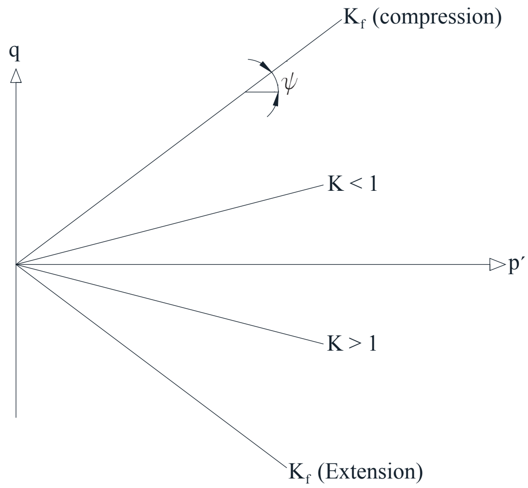

Figure 8.9: *p'-q diagram applied in the analysis of triaxial testing.*

$$sin\ \varphi = tan\ \psi \tag{8.2}$$

The initial stress condition is given by the coefficient of lateral earth pressure at rest, K_0, and can be depicted in a $p' - q$ diagram. This is point A in Figure 8.10 where K is less than one (axial compression). When a specimen is sheared from this configuration both the effective stress path, ESP, as well as the total stress path, TSP, can be outlined in the diagram. For drained cases theses two stress paths will be identical because no excess pore pressure is generated when the specimen is sheared. During undrained shearing the TSP is not coinciding with the ESP because excess pore pressure develops, which thereby has an effect on the effective stresses.

A loose specimen will try to contract when sheared, and therefore positive excess pore pressure, Δu, is generated in the undrained case. This entails that the mean effective stresses will be reduced and the ESP is lower than the TSP. The excess pore pressure can be read off as the horizontal distance between the TSP and the ESP as illustrated in Figure 8.10. In situations where a static ground water table exists there is a initial pore water pressure (hydrostatic) which implies that in reality there are three stress paths; effective stress path ESP, total stress path TSP and total stress path corrected for hydrostatic pore water $TSP - u_0$ see Figure 8.10.

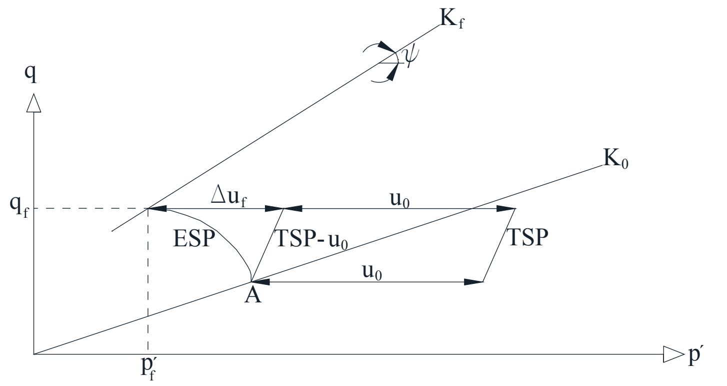

Figure 8.10: *Different stress paths for a given initial condition with coefficient of earth pressure at rest less than one.*

A dense specimen will initially generate a positive excess pore pressure due to contraction, and thereafter a negative excess pore pressure due to dilation, during undrained shearing. The evolution of the ESP will therefore initially be lower than TSP and eventually become higher than TSP, as seen in Figure 8.11.

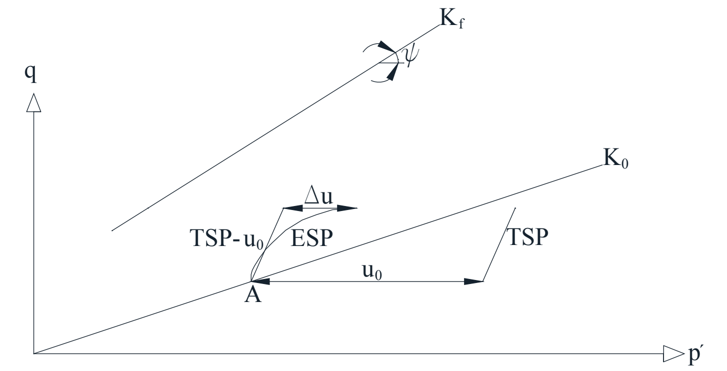

Figure 8.11: *Stress path for dense specimen. Negative excess pore pressure is generated therefore the ESP is to the right of the TSP.*

When failure takes place there will be no further development of the stress paths, in $p' - q$ diagram, since failure is defined as constant volume and constant principle stress difference for strains going towards infinity.

PART III

APPENDIX

Vann. $\Delta W_w - \Delta W_i - \Delta W_s =$ $\boxed{}$

) Kontroller

1) $\Delta W_{i1} + \sum \Delta W_i = W_i$? 448.09

2) $\Delta W_{s1} + \sum \Delta W_s = W_s$? 448.09

Vi må regnes to ganger

Materiale: NC Sandprøve 1 *)

Dybde: ______ *) m, P_o': ______ *) kPa

γ_s = ______ *) kN/m^3

Type forsøk: *)

Rutineundersøkelse ved innbygging: *)

H_i = 71 mm, D_i = 70 mm

V_i = 273.2 cm^3, w_i = 0 %

$w_i = 0$ hvis problemer med våt

Fin silt:	w_i = 5-10	Fin sand:	w_i = 2-5 %
Mid. "	w_i = —"—	Mid. "	w_i = —"—
Grov "	w_i = —"—	Grov "	w_i = —"—

γ_{dmax} = 16.92 *) kN/m^3 ($g = 9.81\ \frac{m}{s^2}$)

γ_{dmin} = 12.97 *) kN/m^3, D_{ri} = 80 *) %

I lab. økes med +2 hvis $w_i = 0$, ellers økes med + 2.5

$$\gamma_{di} = \frac{\gamma_{dmax} \cdot \gamma_{dmin}}{\gamma_{dmax} - D_{ri}(\gamma_{dmax} - \gamma_{dmin})} = 16.09\ kN/m^3$$

$$\text{(Kontr. } D_{ri} = \frac{\gamma_{dmax}}{\gamma_{di}} \cdot \frac{(\gamma_{di} - \gamma_{dmin})}{(\gamma_{dmax} - \gamma_{dmin})} = \text{ ______)}$$

Kontroller

$W_i = \frac{\gamma_{di}}{g} \cdot (1+w_i) \cdot V_i$ = 448.09 g

$W_s = W_i/(1+w_i)$ = 448.09 g, $\gamma_{di} = \frac{W_s \cdot 9.81}{V_i}$ = 16.09

$W_w = W_i - W_s$ = 0 g, $w_i = \frac{W_w}{W_s}$ = 0

Lag nr. 1

0.01

Total vekt: $\Delta W_{i1} = \frac{W_i}{n_{tot}}(1 - U_1) =$ 88.72 g

Vekt sand: $\Delta W_{s1} = \frac{\Delta W_{i1}}{1 + w_i} =$ $\boxed{88.72}$ g

Vekt vann: $\Delta W_{w1} = \Delta W_{i1} - \Delta W_{s1} =$ $\boxed{0}$ g

Alle andre lag

$$\Delta W_i = \frac{W_i}{n_{tot}}\left[2 - \left(U_1 \frac{n_{tot} - 2}{n_{tot} - 1}\right)\right] - \Delta W_{i1}$$

= 89.84 g

Sand: $\Delta W_s = \frac{\Delta W_i}{1 + w_i} =$ $\boxed{89.84}$ g

(n_{tot} er vanligvis lik 6.)

For D_r = 40%	velges U_1	= 0.03
" " = 50%	"	= 0.04
" " = 60%	"	= 0.05
" " = 70%	"	= 0.03
" " = 80%	"	= 0.01
" " = 90%	"	= 0.005
" " = 100%	"	= 0

Valgt verdi av U_1 = ______

Sug: ______ k/cm

Glatte endeplater? ______ Antall gum.lag? ______

Spyling med CO_2? ______ Nold-vann? ______

Saltinnhold i vann som spyles gj. prøve? ______

—"— filtere? ______

Topp st. ______ Tilt { >0.6/30, 0.5/25 ? ______ ; = —"— ? ______ ; = 0 (ingen tilt)? ______ }

Cellevæske: ______ Type celle: ______

Konsolidering:

σ'_{acmax} = ______ *) kPa = ______ kp/cm^2

σ'_{rcmax} = ______ *) kPa = ______ kp/cm^2

σ'_{acmin} = ______ *) kPa = ______ kp/cm^2

σ'_{rcmin} = ______ *) kPa = ______ kp/cm^2

σ'_{ac} = ______ *) kPa = ______ kp/cm^2

σ'_{rc} = ______ *) kPa = ______ kp/cm^2

Mottrykk: ______ kp/cm^2 B-verdi: ______ %

Skal prøven sykles? ______ *) Bruk tilleggsskjema for eventuell syklisk del.

Statisk skjæring:

Maks tenkelige verdi av skjærstyrke:

S = ______ *) kPa $\dot{\varepsilon}_a$ = ______ % pr. time

eller V = ______ min/mm Max def.: ______ *)

Viktig å ta ut moduler fra forsøket? ______ *

Utbygging: Foto før splitting? ______ *

Skal c-verdi måles? ______ etter splitting? ______

Skal prøven { kastes ☐ ; Lagres i 3 mnd ☐ ; > —"— ☐ } *)

Rutineundersøkelser ved utbygging: (på tørket prøve) *

Sign lab.:

Tidsfrist for ferdige tegninger: *

Sign. prosjektleder *

SPESIFIKASJONSSKJEMA FOR TREAKSIALFORSØK MED UNDERKOMPRIMERING (stampet prøve)

PROSJEKTETS NAVN (MAKS 38 KARAKTERER) *)

Leiested nr.	Job. no *)	Boring *)	Tube *)	Part *)	Test *)
	Maks.: 6 siffer	Maks.: 10 karakterer	Tall: 1-99 (+1 bokst.)	Maks.: 2 store bok.	Maks.: 1 siffer (1-9)
171.					
	← Undernr. på tegning *)				

Revidert 31/5-91

Bibliography

Holtz, Kovacs, and Sheahan, **2011**. Robert D. Holtz, William D. Kovacs, and Thomas C.. Sheahan. *An Introduction to Geotechnical Enigineering*. ISBN-13: 978-0-13-701132-2, 2. Edition. PEARSON, 2011.

Ibsen and Lade, **1998**. Lars Bo Ibsen and Poul Lade. *The Role of the Characteristic Line in Static Soil Behavior*, 1998.

Pedersen and Ibsen, **2009**. Thomas Schmidtt Pedersen and Lars Bo Ibsen. *Manual for Dynamic Triaxial Cell*, 2009.

ISSN 1901-726X
DCE Technical Report No. 114

PART III

CONCLUDING REMARKS

Conclusion 2

The objective of this Master's thesis was to investigate the behaviour of cohensionless soils when subjected to cyclic loading. More specifically a marine sand taken from an offshore site in Frederikshavn was investigated. The specific sand, named Frederikshavn Sand, was used because an offshore wind turbine is to be erected at Frederikshavn in late 2012 on a suction caisson. Therefore, a feasibility study was needed in order to investigate the cyclic load bearing capacity of the soil. The evaluation was performed by the following three approaches; A litterature study, Laboratory testing and by nummerical modeling, the conclusion of these are stated below.

A literature study was performed with emphasis on understanding current theories describing cyclic loading. The behaviour of a soil subjected to cyclic loading was found to be dependent on; relative density, mean effective stresses prior to cyclic loading, cyclic and average shear stresses and the drainage conditions. The number of cycles which soils subjected to cyclic loading can undergo were found to be governed by the average and cyclic load ratios. A small increase in load ratio can mean a significant reduction in the cyclic load bearing capacity.

Cyclic loading has a major influence regarding the excess pore pressure in the undrained case. In situations were the mean deviatoric stress is less than the cyclic stable state, pore pressure will build up and potentially become equal to the total stresses as cyclic loading progresses, assumed that the positive and negative pore pressure does not cancel each other out during each cycle. When this happens the effective stresses will become zero and liquefaction occurs which produces unacceptable shear strains.

The initial pore pressure was also found to have a significant impact on the undrained shear strength when conducting triaxial tests. An increase in the initial pore pressure will give an increase in undrained shear strength, due to extra pore pressure before cavitation occurs, meaning that a larger cyclic load can be applied when the initial pore pressure is higher. This is due to the fact that the undrained shear strength is governed by cavitation.

In order to investigate the behaviour of Frederikshavn Sand subjected to cyclic loading, 16 cyclic and 1 monotonic undrained triaxial tests were conducted. Before the tests could be performed the cyclic triaxial apparatus had to be assembled and function properly, which was done over the course of the 3rd semester. This work spawned a manual for conducting cyclic triaxial tests at the Geotechnical Laboratory at Aalborg University.

A modified design diagram was created for the Frederikshavn Sand in the undrained case for a relative density of I_D = 80 %. It can be used to estimate the number of cycles to failure for a given combination of pore pressure, average and cyclic load ratio.

σ'_{vc} was found insufficient to use as a normalisation parameter in the undrained case, as it does not take pore pressure into account. This is important, since the undrained shear strength for a dense sand is governed by cavitation. Therefore the undrained shear strength, c_u, was used as a normalisation parameter for the modified design graph and should be used for other design graphs in the undrained case.

An advanced constitutive model in form of the Modified Critical State Two-Surface Plasticity Model for Sand using the Forward Euler integration scheme was modelled in Matlab. The objective was to investigate if a simple integration scheme could be implemented into an advanced constitutive model and still capture correct stress-strain behaviour of a cohesionless soil. Monotonic and cyclic simulations were performed on a medium-dense sand in order to measure the accuracy of the integration scheme for different strain increments. It was found that with the Forward Euler method the step size would be inappropriately small ($\Delta\varepsilon_1 < 10^{-7}$) for monotonic loading. More importantly the model became unstable for cyclic loading, thereby inducing a large inaccuracy into the model. However, this was not believed to be a problem with the integration scheme itself, but the implementation of the constitutive model. Still, the conclusion is that a simple integration scheme, such as the Forward Euler method, can not be recommended for a model of this complexity.

Beside the Modified Critical State Two-Surface model the Drucker-Prager constitutive model was also modelled in order to compare the Forward Euler integration scheme between the two models. It was found that for the Drucker-Prager model convergence was reached with a step length of 10^{-3} to 10^{-4}, which is much faster than the Modified Critical State Two-Surface model. This also indicate that when the complexity of a constitutive model increases, the needed step size and thereby the usability of the Forward Euler integration scheme decreases. This makes the importance of return mapping more relevant, when constitutive models become more complex.

Discussion 3

Several assumptions have been made through the course of this thesis, especially regarding the cyclic triaxial tests. This was due to both time and mechanical constraints. Therefore some of these assumptions are outlined and discussed in the following sections.

During the sample preparation dry tamping was used until $I_D = 80$ %. For the first cyclic triaxial test, the used drop height was 5 cm. After several tests it was found necessary to reduce the drop height so a relative density of 80 % was maintained. Every time the sand was reused a reduction in drop height was observed. Since no grain size distribution was made prior to triaxial testing, it was not possible to investigate if particle crushing occurred.

During drained cyclic triaxial tests volume changes are measured, which makes a calculation of the cross-sectional area possible. Due to the test set up, this feature is disabled when a test is conducted undrained, and therefore it was not possible to account for cross sectional changes. Stress levels might therefore be slightly overestimated, as an increase in cross sectional area will reduce the stress from the hydraulic piston. For an applied force of 1000 N, the deviation between using the initial cross sectional area and the cross sectional area at 15 % shear strain is in the range of 1-2 %, which is found of minor importance. During liquefaction clear deformation occurs, which indicate a noticeable change in cross sectional area. This makes uncertainties in the calculated stresses, but not in the reached number of cycles before failure occurs.

During cyclic loading, $\Delta\tau_a = \tau_a - \tau_0$ is applied undrained. Furthermore, it is mentioned that a triaxial test should reflect the site conditions. As $\Delta\tau_a$ is the average stress ratio applied besides the isotropic/anisotropic consolidation, it covers the self-weight of a structure and the mean shear stress from loads. Depending on the time between installation of an offshore structure until a storm event, some of $\Delta\tau_a$ will be drained and some undrained. In the end of the consolidation from the structure, only the part of $\Delta\tau_a$ which is created by loading is undrained. As $\Delta\tau_a$ is applied fully undrained during the cyclic triaxial tests, it corresponds to a situation immediately after installation of an offshore structure exposed to cyclic loading.

Another similar topic to discuss is; does sand under real condition experience a 100 % undrained state? The pore pressure build-up measured in element tests, may be an over-estimation of the response of an offshore wind turbine foundation. In the real case the pore pressure build-up may be reduced, by the fact that some pore water is able to dissipate between load cycles. Therefore, estimation of the drainage situation, is thought to be dependent on the load frequency, amplitude and drainage path.

During liquefaction the deformations exceeded the range of the deformation transducers. This entailed that the deformation at failure had to be extrapolated, which leads to uncertainties regarding estimations of number of cycles to failure. However, when liquefaction occurred the number of cycles to failure was relatively low. Another scenario where extrapolation was used was when tests had not reached 15 % shear strain after a certain number of cycles. In these cases the test was stopped before failure, and the number of cycles to failure was extrapolated. This entailed that shakedown may have happened, and an overestimation of numbers of cycles to failure may therefore be possible. Nevertheless shakedown was not observed during the performance of the cyclic test programme.

The making of the contours in the modified design diagram, is connected to a certain amount of uncertainty, as it is created on the basis of relatively few cyclic triaxial tests with a large deviation in number of cycles until failure is obtained. On these grounds the use of the modified design graph is only recommended in the preliminary design phase.

Bibliography

Achmus, Kuo, and Abdel-Rahman, **2009**. Martin Achmus, Yu-Shu Kuo, and Khalid Abdel-Rahman. *Behaviour of monopile foundations under cyclic lateral load*. Computers and Geotechnics, 36, pages 725–735, 2009.

Energistyrelsen, **2012**. Energistyrelsen. *Energiaftalen 22. Marts 2012*. URL: `www.ens.dk/da-DK/Politik/Dansk-klima-og-energi-politik/politiskeaftaler/Sider/Marts2012Aftalefor2012-2020.aspx`, 2012.

Hansson, Hjort, and Thaarup, **2005**. Martin Hansson, Troels H. Hjort, and Martin Thaarup. *Static and transient loading of the bucket foundation for offshore wind-turbines*. M.Sc. Thesis, Aalborg University, 2005.

LeBlanc, **2008**. Christian LeBlanc. *A modified critical state two-surface plasticity model for sand - theory and implementation*. ISSN: 1901-7278, DCE Technical Memorandum no. 8. Aalborg University, 2008.

Lesny, **2010**. Kerstin Lesny. *Foundations for Offshore Wind Turbines*. ISBN: 978-3-86797-042-6, 1. Edition. VGE Verlag GmbH, 2010.

Manzari and Dafalias, **1997a**. M.T. Manzari and Y.F. Dafalias. *Critical state two-surface plasticity model for sands*. Géotechnique, Vol. 47(2), pages 255–272, 1997.

Manzari and Dafalias, **1997b**. M.T. Manzari and Y.F. Dafalias. *Critical state two-surface plasticity model for sands*. Géotechnique, Vol. 47(2), pages 255–272, 1997.

Universal Foundation, **2012**. *Universal Foundation*. URL: `http://www.universalfoundation.dk/`, 2012.

UpWind, **2011**. UpWind. *Design limits and solutions for very large wind turbines*. URL: `www.ewea.org/fileadmin/ewea_documents/documents/upwind/21895_UpWind_Report_low_web.pdf`, 2011.

U.S. Energy Information Administration, **2011**. U.S. Energy Information Administration. *International Energy Outlook*. URL: `www.eia.gov/ieo/pdf/0484(2011).pdf`, 2011.

Part IV

Appendix

A1 Frederikshavn Sand

The test material used during this Master's Thesis is a marine sand from Frederikshavn. Previous to triaxial testing, different laboratory tests were performed in order to obtain the needed material parameters. The parameters that was found are:

- Specific gravity, d_s
- Minimum and maximum void ratios
- Bulk Modulus
- Friction angle

The findings of these parameters described in the following.

A1.1 Specific gravity for Frederikshavn Sand

The specific gravity, d_s, is the ratio between the density of a soil compared to water and is needed in order to determine the minimum and maximum void ratios. It is determined by a standardised method used at Aalborg University. The results is given in Table A1.1, and the specific gravity is found to 2.64.

Prøve		nr	1
Pyknometer		nr	103
W_1	$(W_{\text{pyk}} + W_s + W_{\text{vand}}$	g	734.305
Temperatur,t		$^\circ C$	23.3
W_2	$(W_{\text{pyk+vand}})$	g	642.022
Bægerglas		nr	C128
$W_{\text{bægerglas}} + W_{\text{s}}$		g	570.648
$W_{\text{bægerglas}}$		g	420.677
Tørstof	W_{s}	g	149.971
Vands densitet	$\rho_{\text{w}}^{\text{t}}$	g/ml	0.9975
Relativ densitet	$d_s = \frac{W_s \cdot \rho_w^t}{W_s + W_2 - W_1}$		**2.64**

Table A1.1: *Determination of specific gravity, d_s, for Frederikshavn Sand*

Specific gravity	d_s	**2.64**

Table A1.2: *Specific gravity of Frederikshavn Sand*

A1.2 Minimum and maximum void ratio for Frederikshavn Sand

The minimum and maximum void ratio is determined in by standardised laboratory tests. Hence natural depisots can have void ratios larger then the maximum void ratio and void ratios lower then the minimum void ratio. The tests are made according to ths standard precedure at Aalborg University. The results for the maximum void ratio is given in Table A1.3 and maximum void ratio, e_{max}, is calculated to 1.05.

Prøve	nr	1	2	3	4	5
A	cm^2	10	10	10	10	10
h	cm	7	7	7	7	7
V	cm^3	70	70	70	70	70
Cyl. + W_s	g	330.19	328.20	329.31	328.21	328.29
Cyl.	g	239.14	239.14	239.14	239.14	239.14
W_s	g	91.05	89.06	90.37	89.07	89.15
$e = \frac{d_s \cdot \rho_w \cdot V}{W_s} - 1$		1.02	1.07	1.04	1.07	1.07
						$e_{max} = 1.05$

Table A1.3: *Results for determination of the maximum void ratio.*

The minimum void ratio, e_{min}, is calculated in Table A1.4 to 0.64.

Prøve	nr	1	2	3
A	cm^2	10	10	10
h	cm	6.7	6.6	6.7
V	cm^3	67.00	66.00	67.00
Cyl. + W_s	g	346.90	346.70	345.95
Cyl.	g	239.14	239.14	239.14
W_s	g	107.76	107.56	106.81
$e = \frac{d_s \cdot \rho_w \cdot V}{W_s} - 1$		0.64	0.62	0.65
				$e_{min} = 0.64$

Table A1.4: *Results for determination of the minimum void ratio.*

Minimum void ratio	e_{min}	**0.64**
Maximum void ratio	e_{max}	**1.05**

Table A1.5: *Minimum and maximum void ratio for Frederikshavn Sand.*

A1.3 Bulk modulus of Frederikshavn Sand

Three oedometer tests were conducted in order to determine the bulk modulus, K, which is a measure of volumetric strain due to a change in mean stress. This was done for three relative densities namely, 60 %, 80 % and 100 %. The test were carried out by a standard method developed at Aalborg University. The load steps for the oedometer tests can be seen in Table A1.6.

Table A1.6: *Load steps applied during oedometer test.*

Load step	1	2	3	4	5	6	7	8	9
kg	7.5	15	30	60	30	10	30	60	120
Load step	10	11	12	13	14	15	16	17	18
kg	60	10	60	120	240	120	60	120	240

The consolidation modulus, M, is determined when conducting oedometer tests, see equation (A1.1). The consolidation modulus is related to the modulus of elasticity, E, through equation (A1.2), hereby E can be determined by estimating poissons ratio, ν. This makes it possible to determine the bulk modulus through the relation given in equation (A1.3).

$$M = \frac{\Delta\sigma_1'}{\Delta\varepsilon_1} \tag{A1.1}$$

$$M = \frac{1-\nu}{1+\nu}\cdot\frac{E}{1-2\nu} \quad \Leftrightarrow \quad E = \frac{M(1-\nu-2\nu^2)}{1-\nu} \tag{A1.2}$$

$$K = \frac{E}{3(1-2\nu)} \tag{A1.3}$$

The results from the consolidation tests are given in Figure A1.1. The effective stress levels which the triaxial tests are conducted at the size of 100 kPa, and therefore a consolidation modulus of 360 MPa is choosen for a relative density of 80 %. This value is an average of the 3 curves for the aforementioned stress levels and relative density. Poisson's ratio is estimated to be 0.21. This gives a Bulk modulus of 108 MPa. The results are summarized in Table A1.7.

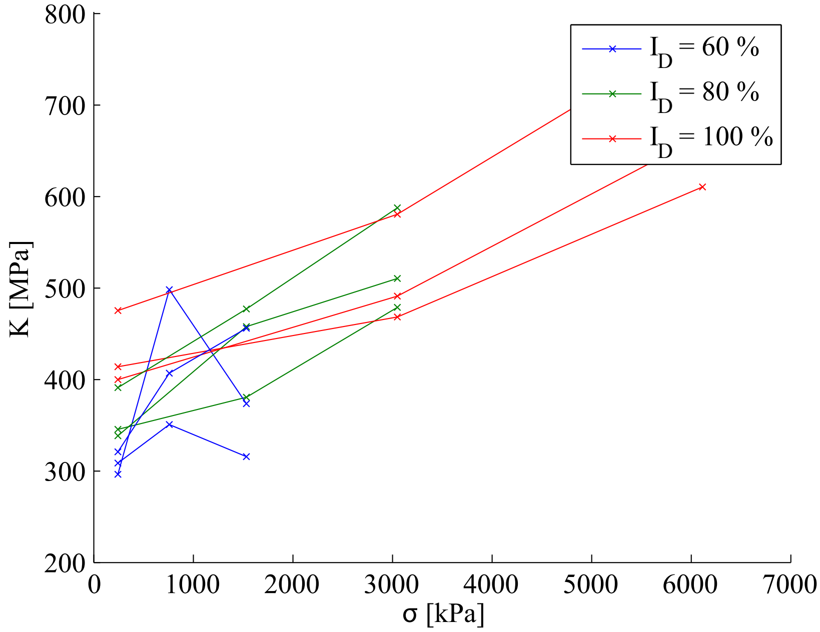

Figure A1.1: Results from oedometer test

Table A1.7: *Values used in order to calculate Bulk modulus, K.*

Poisson's ratio	ν	0.21 [-]
Consolidation Modulus	M	360 [MPa]
Modulus of elasticity	E	323 [MPa]
Bulk modulus	K	**108** [MPa]

A1.4 Friction angle of Frederikshavn Sand

Three drained monotonic isotropic consolidated triaxial tests were made prior to the cyclic triaxial tests in order to determine the friction angle, and thereby the anisotropic consolidation stress conditions.

Monotonic test program

Three monotonic tests were made with different effective isotropic consolidation stresses at 30, 60 and 120 kPa, respectively. The reason for different levels in effective consolidation stresses were in order to catch the curvature of the failure envelope. This is later captured by use of equation (A1.4).

Stress path

The triaxial apparatus applies a force to the sample by moving an hydraulic piston at constant confining pressure. This makes the p'/q ratio and thereby the effective stress path, which is equal to the total stress path, with an inclination of 1:3. An example is shown in Figure A1.2, where p'_0 is the initial effective mean stress in the specimen. This corresponds to the final effective stress during isotropic consolidation.

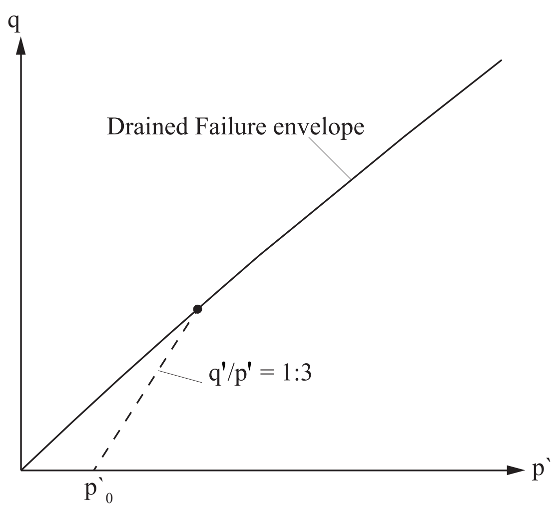

Figure A1.2: *Stress path used during monotonic CD triaxial tests.*

Monotonic test results

In Figure A1.3 the $q-\varepsilon_1$ diagrams from the three monotonic tests with $I_D = 80$ % are depicted. A peak in the deviatoric stress can be observed at approximately 9 % of axial strain. The corresponding value of q will be considered as the bearing capacity of the sample, i.e. the shear strength, τ_f, is $q/2$.

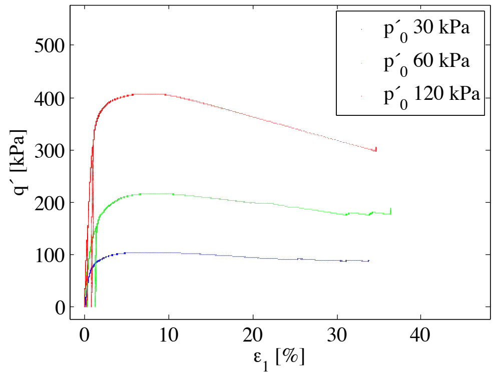

Figure A1.3: *q-ε_1 diagram for monotonic tests.*

From the results the triaxial friction angle is calculated as described in Manzari and Dafalias [1997b], and an the Mohrs circles is illustrated in Figure A1.4. The results is given in Table A1.8 and it is seen that the mean triaxial friction angle is 39.8°. From the table it is observed that the friction angle is decreasing when the initial effective stress, i.e initial cell pressure, increases.

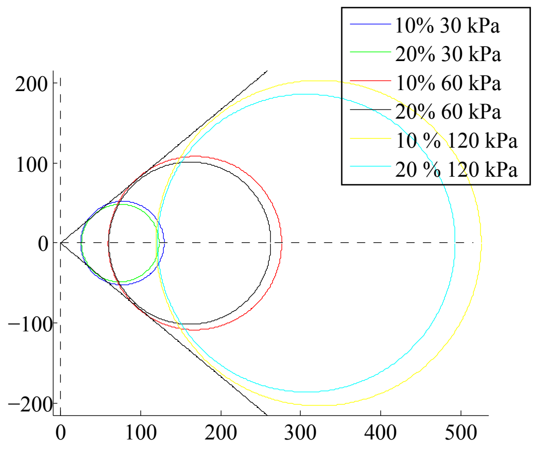

Figure A1.4: *Mohrs circles used to calculate φ.*

Futhermore the curvature of the failure envelope is captured, by introducing an expression for φ as a function of the effective confining pressure, σ'_3, and relative density, I_D. The used expression for the friction angle is given in (A1.4) and is calibrated to Frederikshavn Sand by Hansson et al. [2005] to

Table A1.8: Triaxial friction angle, φ_{tr}, calculated from monotonic tests with a relative density on 80 %.

$\sigma'_{3,i}$ 30 kPa	60 kPa	120 kPa	φ_{tr}
41.6°	39.6°	37.3°	**39.8°**

$$\varphi_{tr} = 0.146\, I_D + 41\, \sigma_3'^{-0.0714} - 1.78° \tag{A1.4}$$

where

I_D	Relative density	[%]
σ'_3	Effective confining pressure	[kPa]

From the unloading-reloading part of the $q-\varepsilon_1$-diagram, which is shown in Figure A1.5, the unloading-reloading Youngs Modulus, E_{ur}, can be calculated. The mean value of E_{ur} for all three tests is 880.6 kPa.

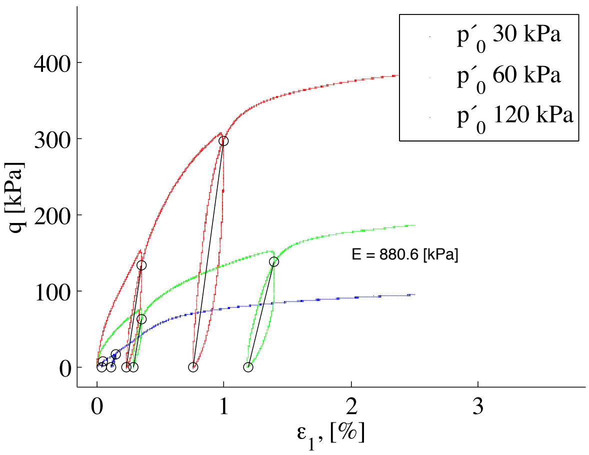

Figure A1.5: Zoom on the unloading-reloading part of the stress strain curve for a relative density I_D = 80 %.

A2 Results from Undrained Triaxial Tests

In the following results from the performed triaxial tests is shown. A complete list of the conducted tests is given in Table A2.1.

Table A2.1: *Average and cyclic shear stress used in the test programme. Test No. 1 is a monotonic test, and test No. 2-17 is cyclic triaxial tests. * was also made as a compression test, of which the results also is shown.*

Test No.	τ_a [kPa]	τ_{cy} [kPa]	u_0 [kPa]
1*	400.2	0.0	110.7
2	209.8	185.2	105.8
3	260.2	100.8	109.2
4	166.9	167.2	110.0
5	129.6	99.9	100.0
6	124.9	49.8	110.1
7	78.0	50.2	120.7
8	53.4	17.0	100.2
9	166.6	167.1	302.3
10	49.6	125.5	99.8
11	24.0	50.9	139.7
12	24.6	100.2	100.3
13	24.8	100.5	160.6
14	24.8	100.4	299.7
15	66.0	125.6	99.5
16	84.1	129.4	100.4
17	158.8	216.9	100.4

A2.1 Test No. 1: Monotonic triaxial test

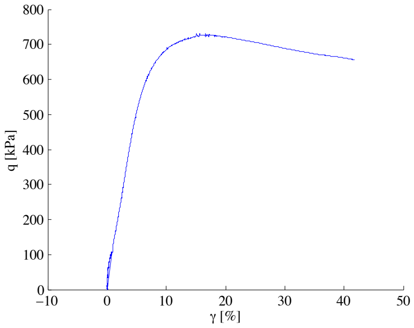

Figure A2.1: *$\gamma - q$ diagram for an undrained monotonic compression test.*

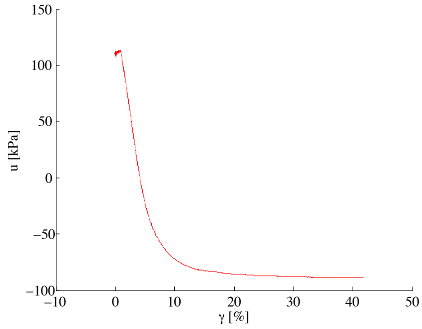

Figure A2.2: *$\gamma - u$ diagram for an undrained monotonic compression test.*

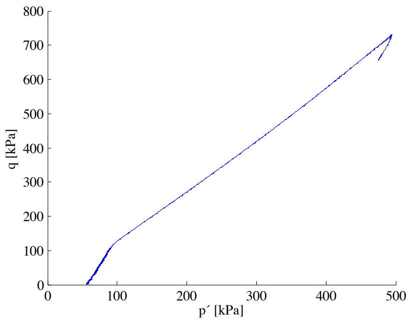

Figure A2.3: *$p' - q$ diagram for an undrained monotonic compression test.*

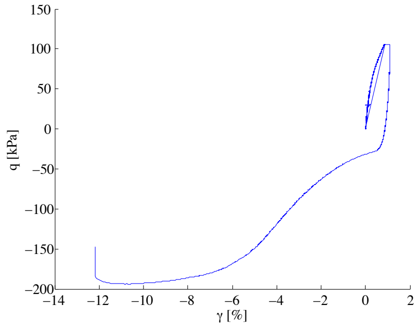

Figure A2.4: $\gamma - q$ *diagram for an undrained monotonic extension test.*

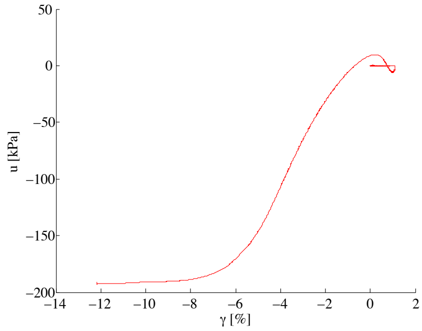

Figure A2.5: $\gamma - u$ *diagram for an undrained monotonic extension test.*

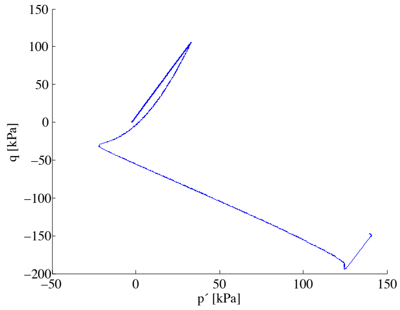

Figure A2.6: $p' - q$ *diagram for an undrained monotonic extension test.*

A2.2 Test No. 2: Cyclic triaxial test

This test was conducted with $\tau_p = 210$ kPa, $\tau_{cy} = 185$ kPa and $u = 106$ kPa.

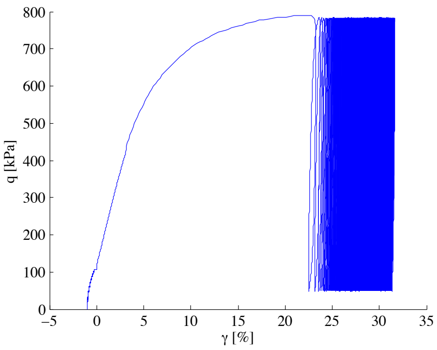

Figure A2.7: *$\gamma - q$ diagram for cyclic triaxial test.*

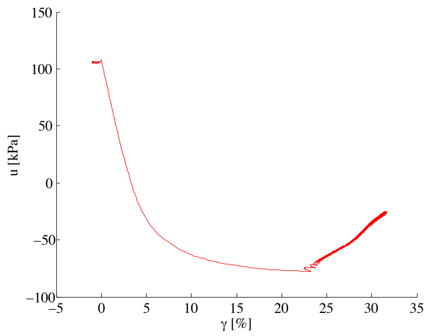

Figure A2.8: *$\gamma - u$ diagram for cyclic triaxial test.*

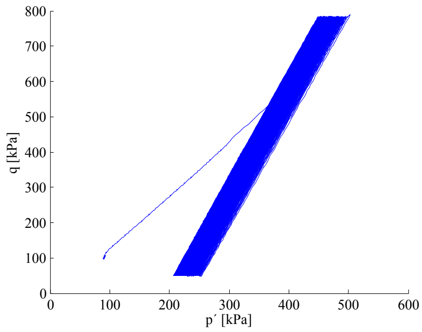

Figure A2.9: *$p' - q$ diagram for cyclic triaxial test.*

A2.3 Test No. 3: Cyclic triaxial test

This test was conducted with $\tau_p = 260$ kPa, $\tau_{cy} = 101$ kPa and $u = 109$ kPa.

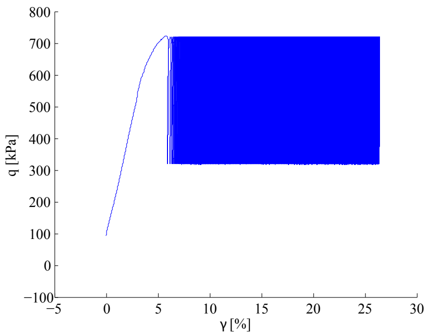

Figure A2.10: *$\gamma - q$ diagram for cyclic triaxial test.*

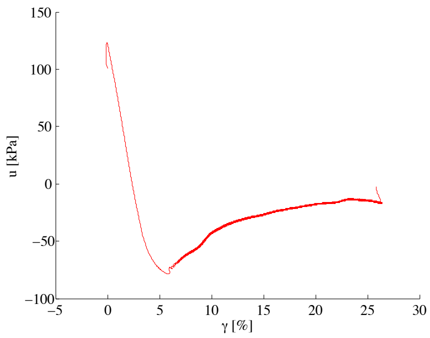

Figure A2.11: *$\gamma - u$ diagram for cyclic triaxial test.*

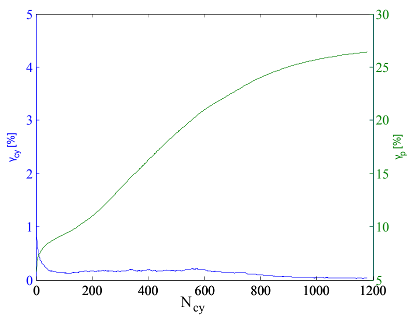

Figure A2.12: *$N - \gamma$ diagram for cyclic triaxial test.*

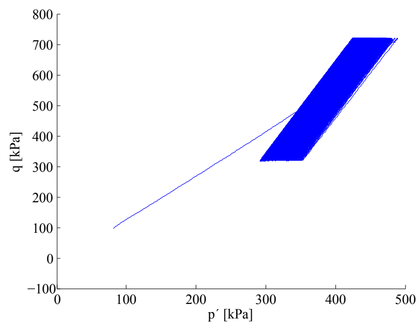

Figure A2.13: *$p' - q$ diagram for cyclic triaxial test.*

A2.4 Test No. 4: Cyclic triaxial test

This test was conducted with $\tau_p = 167$ kPa, $\tau_{cy} = 167$ kPa and $u = 110$ kPa.

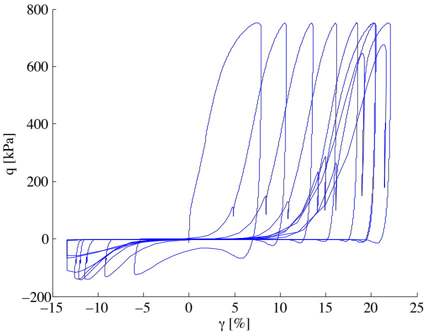

Figure A2.14: *$\gamma - q$ diagram for cyclic triaxial test.*

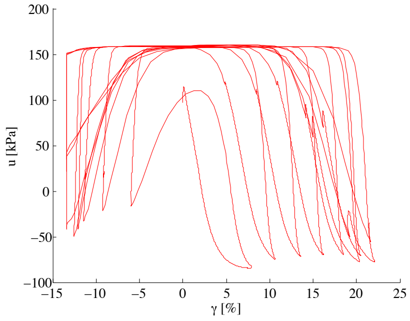

Figure A2.15: *$\gamma - u$ diagram for cyclic triaxial test.*

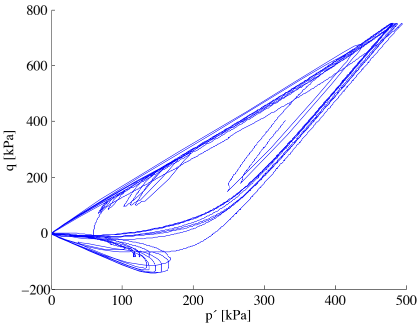

Figure A2.16: *$p' - q$ diagram for cyclic triaxial test.*

A2.5 Test No. 5: Cyclic triaxial test

This test was conducted with $\tau_p = 130$ kPa, $\tau_{cy} = 100$ kPa and $u = 100$ kPa.

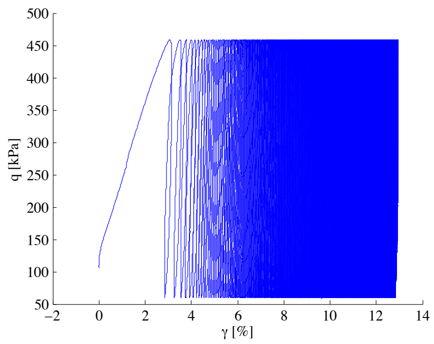

Figure A2.17: *$\gamma - q$ diagram for cyclic triaxial test.*

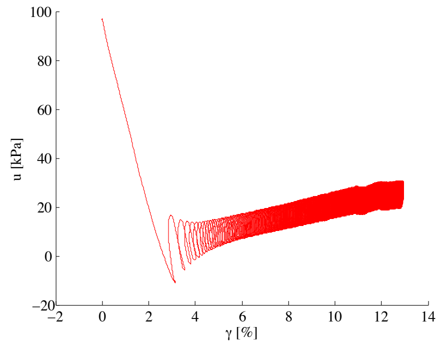

Figure A2.18: *$\gamma - u$ diagram for cyclic triaxial test.*

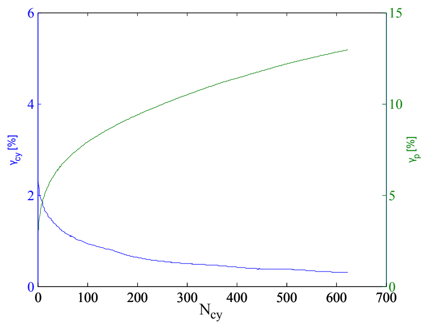

Figure A2.19: *$N - \gamma$ diagram for cyclic triaxial test.*

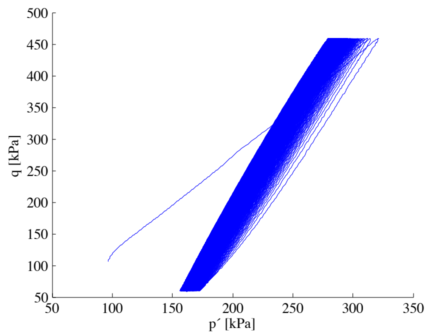

Figure A2.20: *$p' - q$ diagram for cyclic triaxial test.*

A2.6 Test No. 6: Cyclic triaxial test

This test was conducted with $\tau_p = 125$ kPa, $\tau_{cy} = 50$ kPa and $u = 110$ kPa.

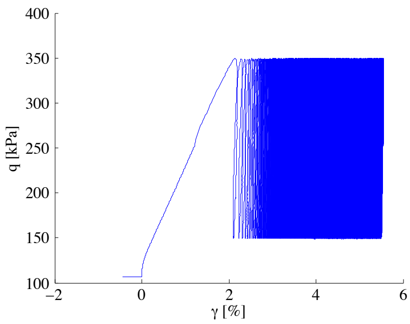

Figure A2.21: *$\gamma - q$ diagram for cyclic triaxial test.*

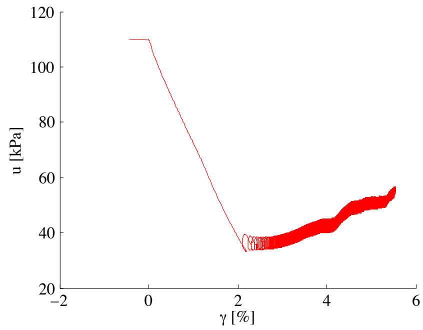

Figure A2.22: *$\gamma - u$ diagram for cyclic triaxial test.*

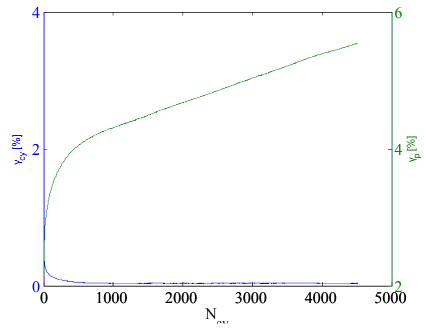

Figure A2.23: *$N - \gamma$ diagram for cyclic triaxial test.*

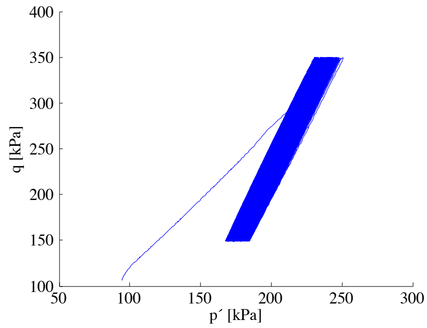

Figure A2.24: *$p' - q$ diagram for cyclic triaxial test.*

A2.7 Test No. 7: Cyclic triaxial test

This test was conducted with $\tau_p = 78$ kPa, $\tau_{cy} = 50$ kPa and $u = 121$ kPa.

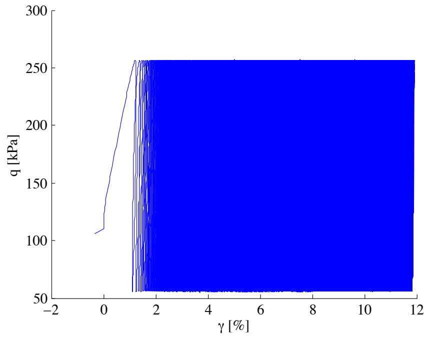

Figure A2.25: *$\gamma - q$ diagram for cyclic triaxial test.*

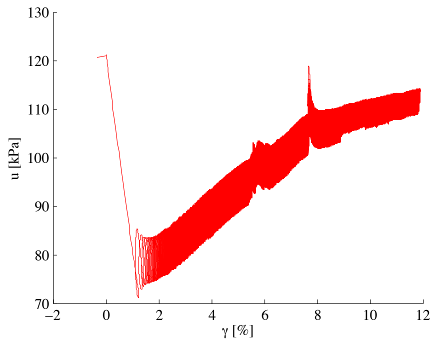

Figure A2.26: *$\gamma - u$ diagram for cyclic triaxial test.*

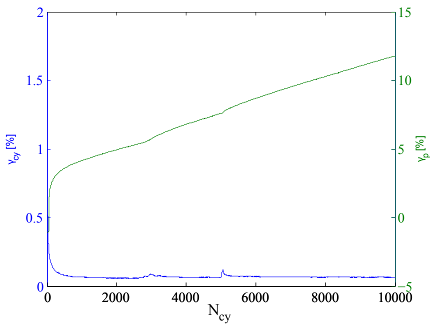

Figure A2.27: *$N - \gamma$ diagram for cyclic triaxial test.*

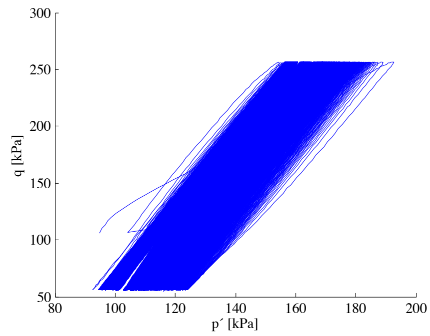

Figure A2.28: *$p' - q$ diagram for cyclic triaxial test.*

A2.8 Test No. 8: Cyclic triaxial test

This test was conducted with $\tau_p = 53$ kPa, $\tau_{cy} = 17$ kPa and $u = 100$ kPa.

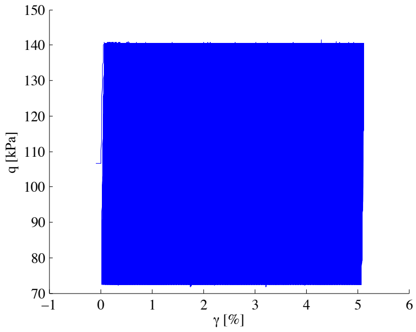

Figure A2.29: *$\gamma - q$ diagram for cyclic triaxial test.*

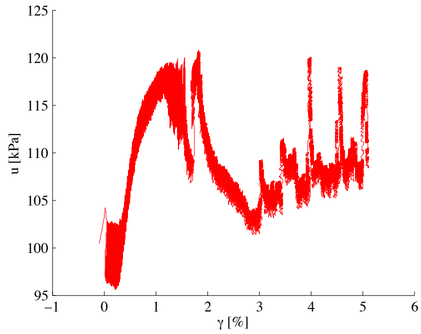

Figure A2.30: *$\gamma - u$ diagram for cyclic triaxial test.*

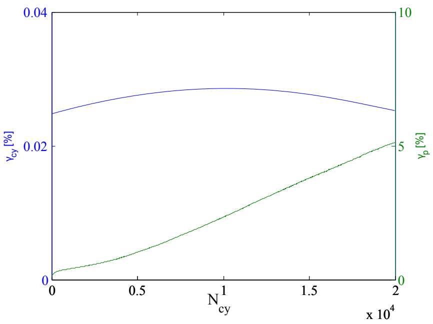

Figure A2.31: *$N - \gamma$ diagram for cyclic triaxial test.*

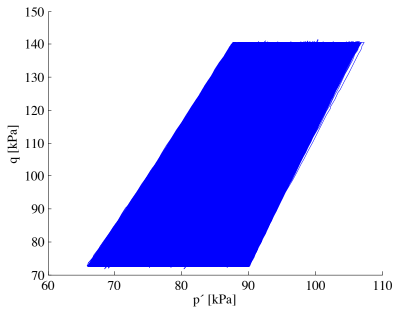

Figure A2.32: *$p' - q$ diagram for cyclic triaxial test.*

A2.9 Test No. 9: Cyclic triaxial test

This test was conducted with $\tau_p = 167$ kPa, $\tau_{cy} = 167$ kPa and $u = 302$ kPa.

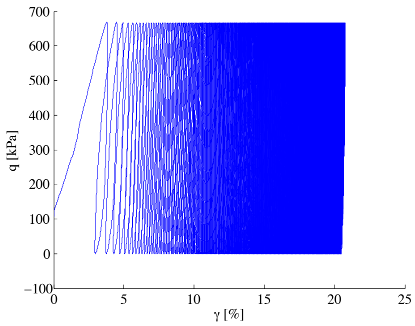

Figure A2.33: *$\gamma - q$ diagram for cyclic triaxial test.*

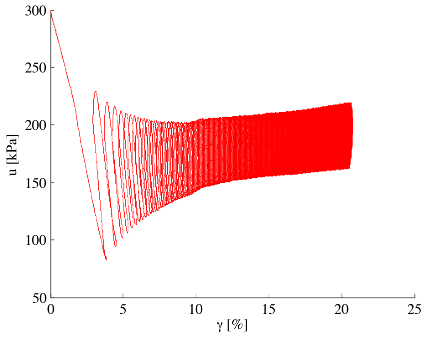

Figure A2.34: *$\gamma - u$ diagram for cyclic triaxial test.*

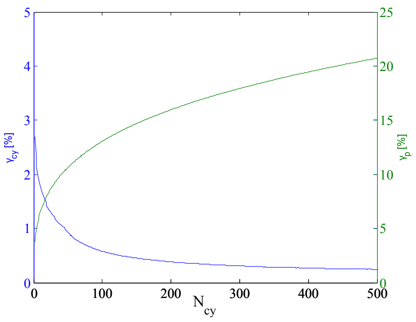

Figure A2.35: *$N - \gamma$ diagram for cyclic triaxial test.*

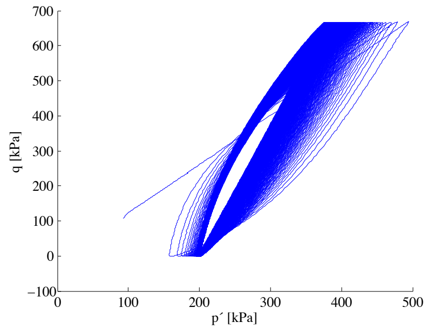

Figure A2.36: *$p' - q$ diagram for cyclic triaxial test.*

A2.10 Test No. 10: Cyclic triaxial test

This test was conducted with $\tau_p = 50$ kPa, $\tau_{cy} = 126$ kPa and $u = 100$ kPa.

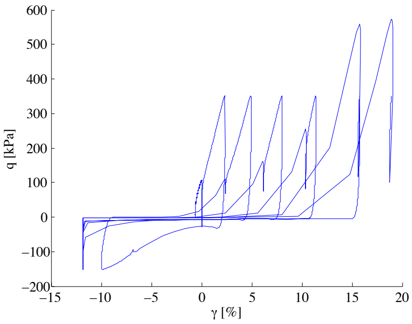

Figure A2.37: *$\gamma - q$ diagram for cyclic triaxial test.*

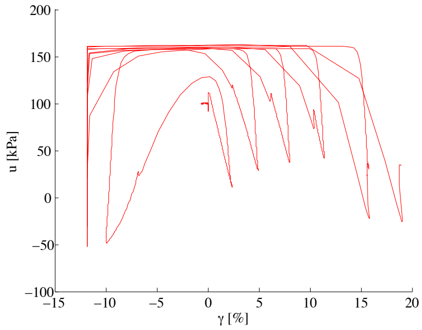

Figure A2.38: *$\gamma - u$ diagram for cyclic triaxial test.*

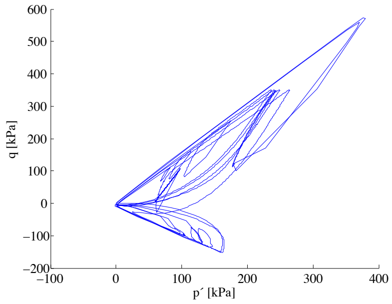

Figure A2.39: *$p' - q$ diagram for cyclic triaxial test.*

A2.11 Test No. 11: Cyclic triaxial test

This test was conducted with $\tau_p = 24$ kPa, $\tau_{cy} = 51$ kPa and $u = 140$ kPa.

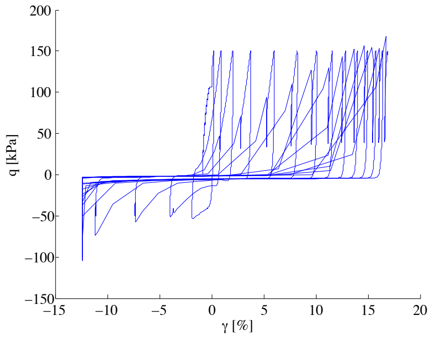

Figure A2.40: *$\gamma - q$ diagram for cyclic triaxial test.*

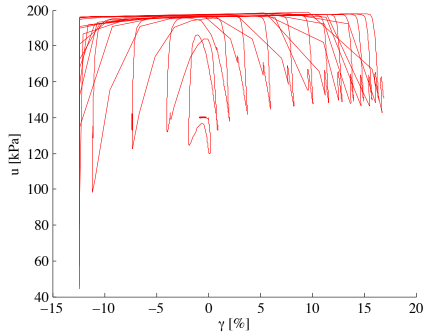

Figure A2.41: *$\gamma - u$ diagram for cyclic triaxial test.*

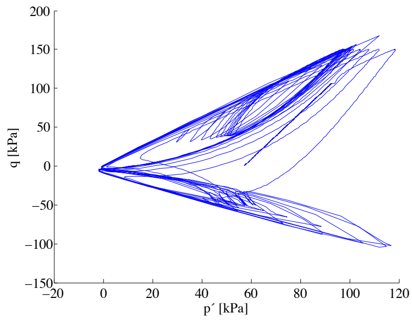

Figure A2.42: *$p' - q$ diagram for cyclic triaxial test.*

A2.12 Test No. 12: Cyclic triaxial test

This test was conducted with $\tau_p = 25$ kPa, $\tau_{cy} = 100$ kPa and $u = 100$ kPa.

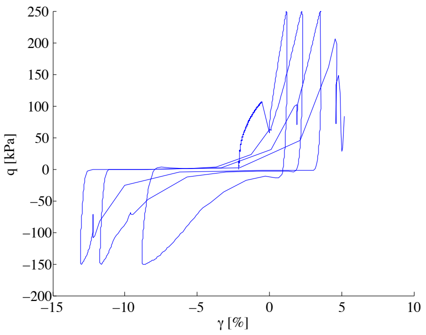

Figure A2.43: *$\gamma - q$ diagram for cyclic triaxial test.*

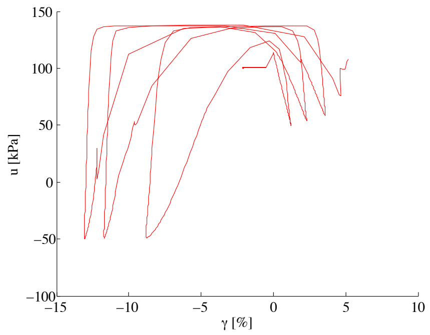

Figure A2.44: *$\gamma - u$ diagram for cyclic triaxial test.*

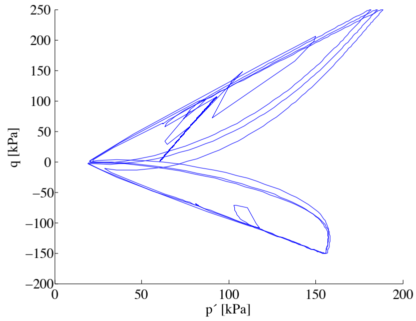

Figure A2.45: *$p' - q$ diagram for cyclic triaxial test.*

A2.13 Test No. 13: Cyclic triaxial test

This test was conducted with $\tau_p = 25$ kPa, $\tau_{cy} = 101$ kPa and $u = 161$ kPa.

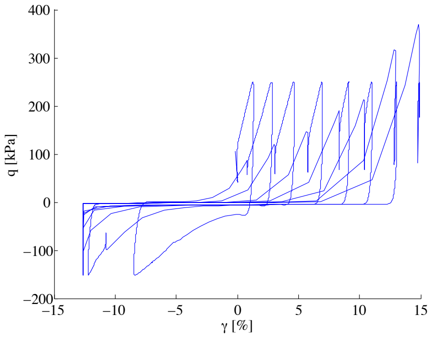

Figure A2.46: *$\gamma - q$ diagram for cyclic triaxial test.*

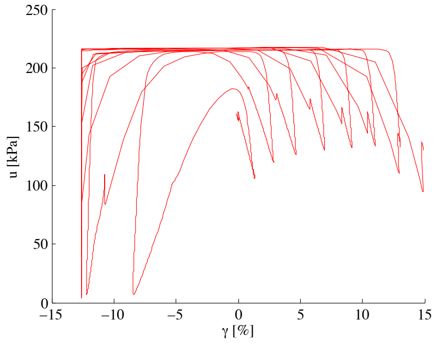

Figure A2.47: *$\gamma - u$ diagram for cyclic triaxial test.*

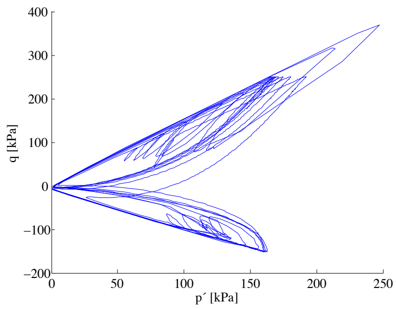

Figure A2.48: *$p' - q$ diagram for cyclic triaxial test.*

A2.14 Test No. 14: Cyclic triaxial test

This test was conducted with $\tau_p = 25$ kPa, $\tau_{cy} = 100$ kPa and $u = 300$ kPa.

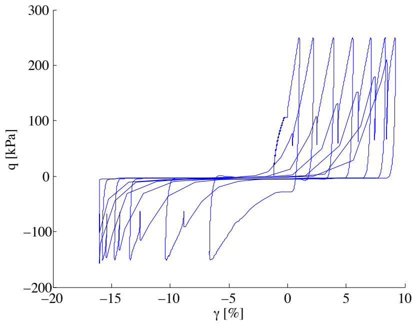

Figure A2.49: *$\gamma - q$ diagram for cyclic triaxial test.*

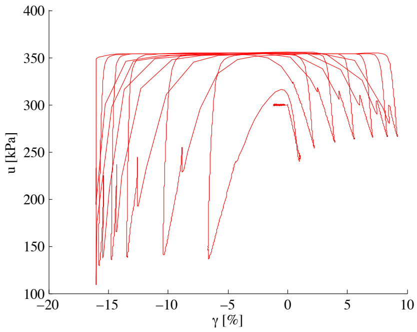

Figure A2.50: *$\gamma - u$ diagram for cyclic triaxial test.*

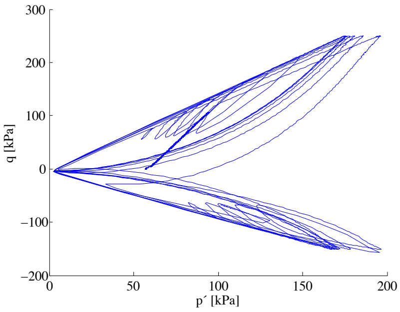

Figure A2.51: *$p' - q$ diagram for cyclic triaxial test.*

A2.15 Test No. 15: Cyclic triaxial test

This test was conducted with $\tau_p = 66$ kPa, $\tau_{cy} = 126$ kPa and $u = 100$ kPa.

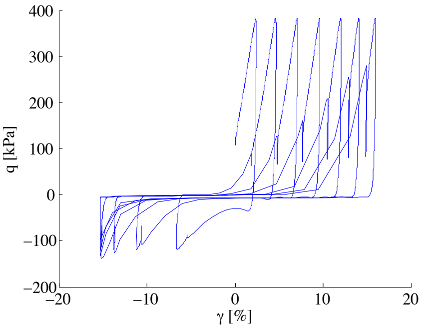

Figure A2.52: *$\gamma - q$ diagram for cyclic triaxial test.*

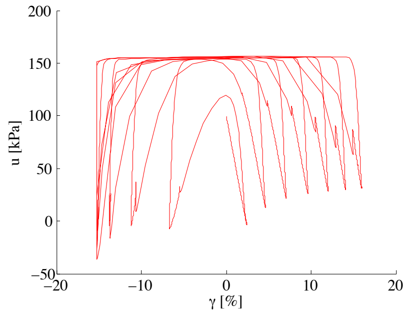

Figure A2.53: *$\gamma - u$ diagram for cyclic triaxial test.*

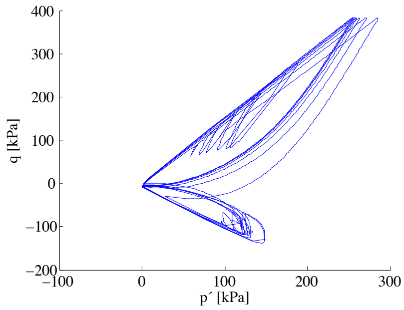

Figure A2.54: *$p' - q$ diagram for cyclic triaxial test.*

A2.16 Test No. 16: Cyclic triaxial test

This test was conducted with $\tau_p = 84$ kPa, $\tau_{cy} = 129$ kPa and $u = 100$ kPa.

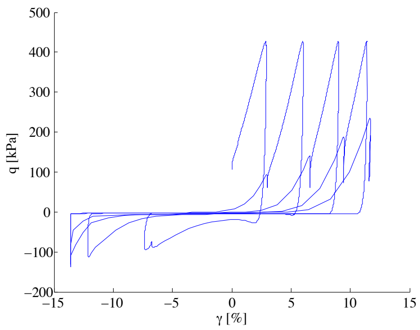

Figure A2.55: *$\gamma - q$ diagram for cyclic triaxial test.*

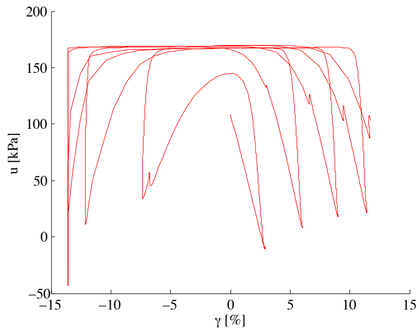

Figure A2.56: *$\gamma - u$ diagram for cyclic triaxial test.*

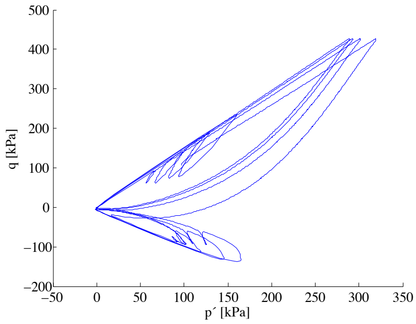

Figure A2.57: *$p' - q$ diagram for cyclic triaxial test.*

A2.17 Test No. 17: Cyclic triaxial test

This test was conducted with $\tau_p = 160$ kPa, $\tau_{cy} = 217$ kPa and $u = 100$ kPa.

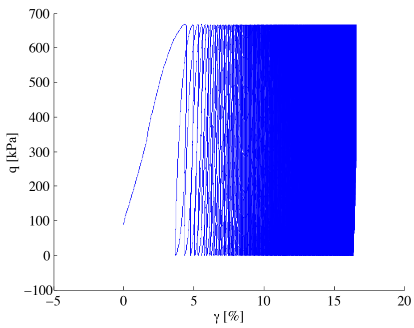

Figure A2.58: *$\gamma - q$ diagram for cyclic triaxial test.*

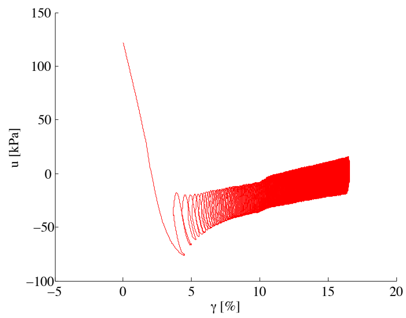

Figure A2.59: *$\gamma - u$ diagram for cyclic triaxial test.*

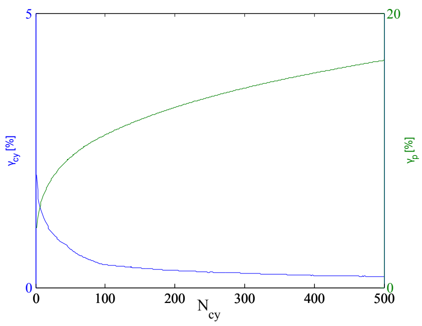

Figure A2.60: *$N - \gamma$ diagram for cyclic triaxial test.*

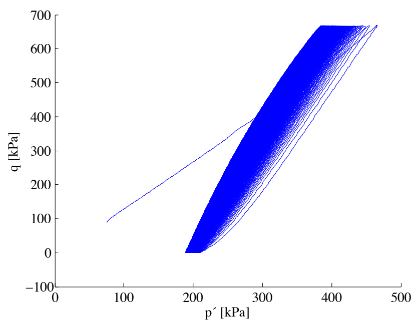

Figure A2.61: *$p' - q$ diagram for cyclic triaxial test.*

A3 Drucker-Prager Yield Criterion

The Drucker-Prager failure criterion is often applied for soils since it includes the dependency of the hydrostatic pressure. This is also the reason why the formulation does not have a constant distance to the hydrostatic axis in the meridian plan, this is also illustrated in Figure A3.1. This dependency is captured by including the first invariant of the stress tensor, I_1, in the formulation of the yield function . The deviatoric influence is accounted for by including the second invariant of the deviatoric stress tensor, J_2, in the yield function. The yield function for this criterion is given as

$$f(I_1, J_2) = \sqrt{3J_2} + \alpha I_1 - k \tag{A3.1}$$

where α is the hardening variable and k is a material parameter. When criteria are formulated without any hardening, i.e. perfect plasticity, the yield surface will be fixed and the stress state will remain on the yield surface during plasticity, either in one position or slide along the surface when stresses are redistributed.

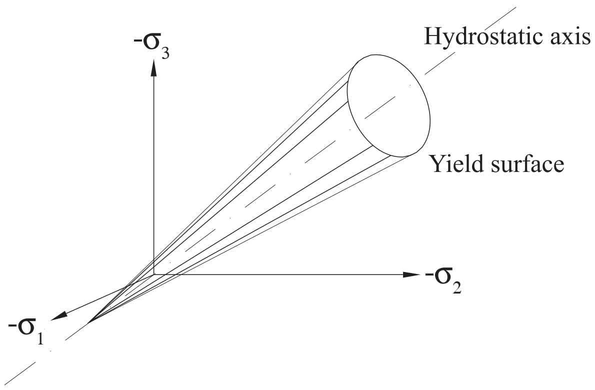

Figure A3.1: Drucker-Prager yield criterion in priciple stress space

The yield criterion was formulated linear elastic perfect plastic, for a cyclic load given as

$$\varepsilon_1(x) = 10\,x^{0.3\,sin(x)} \tag{A3.2}$$

The response is shown in Figure A3.2. From the figure it can be observed that every time the stress becomes plastic the stress path follows the yields surface. The criterion was also formulated with hardening e.g. elasto-plastic, but no illustration of the response was performed because of complexities.

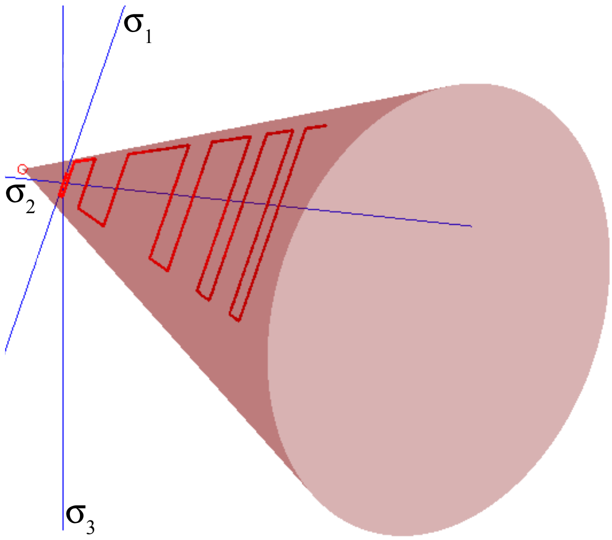

Figure A3.2: *Drucker Prager yield surface.*